VU VRIJE UNIVERSITEIT AMSTERDAM

VU Research Portal

High-harmonic spectroscopy and holographic imaging of semiconductors and correlated materials

Guery, Léo Claude Jacques

2026

DOI (link to publisher)
10.5463/thesis.1722

document version
Publisher's PDF, also known as Version of record

Link to publication in VU Research Portal

citation for published version (APA)
Guery, L. C. J. (2026). *High-harmonic spectroscopy and holographic imaging of semiconductors and correlated materials*. [PhD-Thesis - Research and graduation internal, Vrije Universiteit Amsterdam]. https://doi.org/10.5463/thesis.1722

General rights
Copyright and moral rights for the publications made accessible in the public portal are retained by the authors and/or other copyright owners and it is a condition of accessing publications that users recognise and abide by the legal requirements associated with these rights.

- Users may download and print one copy of any publication from the public portal for the purpose of private study or research.
- You may not further distribute the material or use it for any profit-making activity or commercial gain
- You may freely distribute the URL identifying the publication in the public portal

Take down policy
If you believe that this document breaches copyright please contact us providing details, and we will remove access to the work immediately and investigate your claim.

E-mail address:
vuresearchportal.ub@vu.nl

Download date: 14. Oct. 2026

HIGH-HARMONIC SPECTROSCOPY AND HOLOGRAPHIC IMAGING OF SEMICONDUCTORS AND CORRELATED MATERIALS

Léo Guery

VRIJE UNIVERSITEIT

High-Harmonic Spectroscopy and Holographic Imaging of Semiconductors and correlated materials

ACADEMISCH PROEFSCHRIFT

ter verkrijging van de graad Doctor
aan de Vrije Universiteit Amsterdam,
op gezag van de rector magnificus
prof.dr. J.J.G. Geurts,
volgens besluit van de decaan
van de Faculteit der Bètawetenschappen
in het openbaar te verdedigen
op woensdag 9 september 2026 om 11.45 uur
in de universiteit

door

Léo Claude Jacques Guery

geboren te Tournan-en-Brie, Frankrijk

promotor:	dr. P.M. Kraus
copromotoren:	prof.dr. S.M. Witte dr. L.V. Amitonova
promotiecommissie:	prof.dr. A.J. den Boef prof.dr. B.I. Avci dr. A. Mondal prof.dr. P.C.M. Planken prof.dr. H. Merdji

This dissertation was approved by

Promoter:	
dr. Peter M. Kraus	ARCNL, Vrije Universiteit Amsterdam Amsterdam, The Netherlands
Copromoters:	
prof.dr. Stefan Witte	TU Delft Delft, The Netherlands
dr. Lyuba Amitonova	ARCNL, Vrije Universiteit Amsterdam Amsterdam, The Netherlands

Dissertation Committee

Committee:	
prof.dr. Arie den Boef	ARCNL, ASML, Vrije Universiteit Amsterdam Amsterdam, The Netherlands
prof.dr. Imran Avci	Vrije Universiteit Amsterdam Amsterdam, The Netherlands
dr. Angana Mondal	ARCNL, Universiteit van Amsterdam, Amsterdam, The Netherlands
prof.dr. Paul C.M. Planken	ARCNL, Universiteit van Amsterdam, Amsterdam, The Netherlands
prof.dr. Hamed Merdji	CEA-Saclay, École Polytechnique, LOA Saclay, France

© 2026, Léo Guery
All rights reserved. No part of this publication may be reproduced, stored in a retrieval system or transmitted in any form or by any means electronic, mechanical, photocopying, recording or otherwise, without the prior written permission of the author.
DOI: https://doi.org/10.5463/thesis.1722

CONTENTS

1 Introduction **1**

2 Theoretical framework **5**
2.1 Scalar diffraction theory . . . 6
2.2 Holography . . . 8
2.2.1 Digital holographic microscopy . . . 8
2.2.2 Fourier transform holography . . . 11
2.3 High-harmonic generation in solids . . . 13
2.3.1 Introduction . . . 13
2.3.2 Semi-classical description . . . 14
2.3.3 Macroscopic properties . . . 18
2.3.4 Applications of Solid-HHG . . . 20
2.4 Correlated electron systems . . . 21

3 Methods **25**
3.1 Laser source . . . 26
3.2 Nanofabrication . . . 27
3.3 Numerical methods . . . 29
3.3.1 Computation of field distributions in nanostructures . . . 29
3.3.2 High dynamic range image stitching . . . 29
3.3.3 Fourier ring correlation . . . 30
3.3.4 Angular spectrum field propagation . . . 32

4 Non-Linear DHM for reconstruction of subwavelength structures **35**
4.1 Introduction . . . 36
4.2 Methods . . . 37
4.2.1 Analytical framework for transmission THG . . . 37
4.2.2 Experimental setup . . . 38
4.2.3 Sample design . . . 38
4.2.4 Hologram amplitude and phase reconstruction procedure . . . 38
4.3 Results and discussion . . . 41
4.4 Conclusion . . . 47

5 Non-linear Fourier transform holography **49**
5.1 Introduction . . . 50
5.2 Methods . . . 51
5.2.1 Reconstruction methodology . . . 51
5.2.2 Sample fabrication . . . 52
5.2.3 Experimental setup, data acquisition and analysis . . . 52

5.3 Results . . . 53
5.4 Conclusion . . . 58

6 Following the nonthermal phase transition in NbO_2 by harmonic spectro. 61
6.1 Introduction . . . 62
6.2 Results . . . 63
6.3 Conclusions. . . . 68

7 HHG field charact. using an interferometric non-linear conversion technique 81
7.1 Introduction . . . 82
7.2 Collinear harmonic generation auto-correlation . . . 83
7.2.1 Methods . . . 83
7.2.2 Results . . . 87
7.3 SCORPIO . . . 90
7.3.1 Methods . . . 90
7.3.2 Results . . . 94
7.4 Conclusion . . . 97

8 Non-linear pump-probe DHM for tracking the ultrafast phase transition in NbO_2 99
8.1 Introduction . . . 100
8.2 Methods . . . 100
8.3 Results . . . 104
8.4 Conclusion . . . 108

Bibliography 109

List of publications 123

Summary 125

1

INTRODUCTION

1

Efforts toward reaching a better understanding of interactions between light and matter have been a driving force for technological development since ancient times. Daily observable phenomena such as the formation of rainbows, reflection from mirrors, or simply the color of the sky took humanity centuries to understand. The benefits gained from seeking a refined comprehension of light–matter interactions are profound, and led to major technological breakthroughs. As striking evidence, one may mention the invention of the transistor in 1947 [1], which on its own has completely transformed modern society.

With the invention of the laser in 1960, a revolutionary tool became accessible to researchers for studying light–matter interactions [2]. By providing very intense coherent sources of light, these devices could be used to interrogate matter in completely new ways. In 1985, the first developments of chirped-pulse amplification (CPA) systems helped to further push our capacities to probe matter, both by allowing access to intensity regimes never reached before and by enabling ultrashort timescales in the femtosecond range [3].

The orbital period of an electron around its nucleus can be used to estimate the typical timescale of electronic motion. In the Bohr model, a rough estimate of this period for a hydrogen atom is given by [4]:

$$T = \frac{2\pi r}{v} \tag{1.1}$$

where $r \approx 0.5$Å is the orbital radius and $v \approx 2.2 \times 10^6$ m/s is the electron velocity, leading to a period of 1.5×10^{-16} s, or 0.15 fs. Therefore, reaching femtosecond resolution was a crucial step toward investigating how electrons behave in matter, giving rise to the field of femtochemistry.

A next step in the development of ultrafast optics was the discovery of high-harmonic generation (HHG): by focusing a very intense laser in a gas, liquid, or solid medium, highly nonlinear interactions lead to the generation of a discrete set of harmonics of the fundamental driving field, which can extend to the XUV/soft-X-ray range [5, 6].

HHG was first demonstrated in gases in the late 1980s, launching the field of attosecond science, and more recently in solids [7]. Since its discovery, solid HHG has proven to be an excellent tool for probing ultrafast changes in the electronic structure of solids [8]. Although its modeling can be challenging and still motivates significant efforts in terms of theoretical description and the development of advanced computational techniques [9–12], it has been used successfully to investigate electronic, structural, and topological dynamics in matter.

Solid HHG (SHHG), as a nonlinear technique, provides both advantages and challenges when employed as a probe of ultrafast electronic dynamics [13–15]. Due to the sub-cycle emission nature of HHG, harmonic spectroscopy can provide sub-femtosecond time resolution [16, 17]. HHG can offer microscopic spatial resolution and possibly super-resolution below the diffraction limit [18]. However, the interpretation of transient harmonic spectroscopy is challenging, as the highly nonlinear nature of the light–matter interaction in SHHG is related in a complex manner to the underlying electronic structure and dynamics. Therefore, experiments backed by theory are needed, and HHG must be characterized in as much detail as possible.

In order to fully characterize harmonic emission, both phase and amplitude need to be measured. Therefore, this thesis deploys solid HHG as a probe of ultrafast dynamics and combines it with holographic techniques, which are widely used to measure the spatial distribution of the phase of light in addition to its amplitude. Retrieving these two quantities is crucial in order to fully describe light–matter interactions and, as a result, extract more information from the harmonic generation process. Finally, this thesis also presents a first exploratory experiment that characterizes the harmonic emission itself on sub-cycle timescales. This step can dramatically increase the time resolution for experiments in which the dynamics of interest are initiated by the harmonic driving pulse itself, as opposed to typical dual-pulse pump–probe experiments where resolution is linked to the cross-correlation of the durations of both laser pulses.

OUTLINE

Two main topics are investigated using SHHG holography: the metrology of subwavelength structures etched in semiconductors, and the ultrafast dynamics of phase transitions in quantum materials.

After a general introduction in chapter 1, chapter 2 presents the theoretical background of high-harmonic generation, the holographic techniques used in the thesis, and a basic introduction to the physics of correlated materials. Chapter 3 details the experimental and numerical methods used throughout the thesis. Chapter 4 presents results concerning the reconstruction of subwavelength structures by combining digital holographic microscopy and SHHG. Chapter 5 introduces another holographic technique, Fourier-transform holography (FTH). In chapter 6, we investigate the ultrafast phase transition in NbO_2, a correlated electron system, through pump–probe harmonic generation. This investigation continues in chapter 7 with the introduction of a novel interferometric technique aimed at unveiling sub-cycle dynamics occurring in the material. In the final chapter 8, we combine the concepts introduced in chapters 4 and 6 to measure the transient third-harmonic field emitted from photoexcited NbO_2 samples.

2

THEORETICAL FRAMEWORK

2.1 SCALAR DIFFRACTION THEORY

Diffraction is most clearly observed when light is scattered from structures with features that are of the order of the wavelength. The Rayleigh-Sommerfeld formulation aims at computing the wavefront of the field at a distance from the scattering object. In this model, the vectorial nature of electromagnetic waves is ignored, polarization effects being considered negligible, and the field as treated as a scalar quantity. The first Born approximation, in which only single-scattering event per source term are considered, is also assumed. If we consider a monochromatic wave $E_0(x,y)$ of frequency ω, diffracted from a plane, under normal incidence, the field at a distance z along the propagation of the field is given by [19]:

$$E(x,y,z) = \frac{ik}{2\pi}\iint_{\Sigma_0} E_0(x_0,y_0,z=0)\frac{exp(ik\vec{r})}{|\vec{r}|}dx_0dy_0 \tag{2.1}$$

Where $E_0(x_0,y_0,z=0)$ and $E(x,y,z)$ respectively stand for the electric field in the scattering object plane Σ_0, and the plane Σ, where the field is calculated. $k=\frac{2\pi}{\lambda}$ is the wavenumber of the incoming field and $\vec{r}$ is a vector originating from plane Σ_0 and reaching plane Σ.

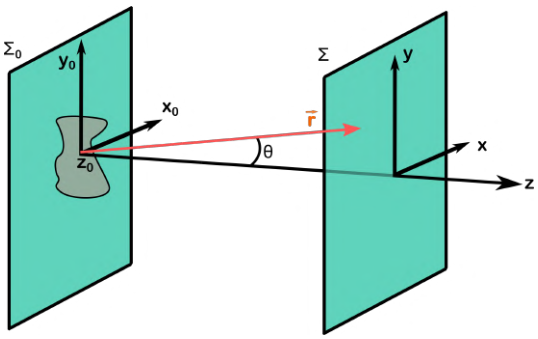


Figure 2.1: Diffraction geometry in the Rayleigh-Sommerfeld formulation of diffraction. A plane wave is transmitted the aperture in plane Σ_0, and propagates to the perpendicular plane Σ located at distance z.

This formula takes its roots in the Huygens-Fresnel depiction of the diffraction phenomena which states that the field emitted from an object can be expressed as the sum of spherical waves emitted by secondary sources. Adequate approximations can enable to obtain relatively simple mathematical formulations of the diffraction process for two distinct regimes: the Fresnel and Fraunhoffer diffraction integrals. The norm of vector $\vec{r}$ is given by:

$$|\vec{r}| = \sqrt{(x-x_0)^2+(y-y_0)^2+z^2} \tag{2.2}$$

If we call $\rho^2 = (x-x_0)^2+(y-y_0)^2$, we have:

$$|\vec{r}| = z\sqrt{1+\frac{\rho^2}{z^2}} \tag{2.3}$$

By applying a binomial expansion, we can write it as:

$$|\vec{r}| = z\left[1 + \frac{\rho^2}{2z^2} - \frac{1}{8}\left(\frac{\rho^2}{z^2}\right)^2 + ...\right] \tag{2.4}$$

Fresnel diffraction consists in applying a paraxial approximation to this last equation. Higher order terms of the binomial expansion can be considered negligible if the angles between $\vec{r}$ and the normal to the the two planes Σ and Σ_0 are small. Therefore we can write:

$$\begin{aligned} |\vec{r}| &\approx z\left[1 + \frac{\rho^2}{2z^2}\right] \\ &= z\left[1 + \frac{(x-x_0)^2}{2z^2} + \frac{(y-y_0)^2}{2z^2}\right] \end{aligned} \tag{2.5}$$

Injecting this term in equation 2.1, we have:

$$E(x,y,z) = \frac{e^{ikz}}{i\lambda z}\iint_{\Sigma_0} E_0(x_0,y_0,0)\, e^{\frac{ik}{2z}[(x-x_0)^2+(y-y_0)^2]}\, dx_0 dy_0 \tag{2.6}$$

By expanding the exponent, we get:

$$E(x,y,z) = \frac{e^{ikz}}{i\lambda z} e^{\frac{ik}{2z}(x^2+y^2)}\iint_{\Sigma_0} E_0(x_0,y_0,0)\, e^{\frac{ik}{2z}(x_0^2+y_0^2)}\, e^{-i\frac{2\pi}{\lambda z}(x_0 x + y_0 y)}\, dx_0 dy_0 \tag{2.7}$$

This expression, known as the Fresnel integral, gives the field distribution at any distance from the origin plane. It can be even more simplified if we consider a long-enough propagation distance z compared to the feature size of the scattering object:

$$z \gg \frac{k}{2}(x_0^2 + y_0^2) \tag{2.8}$$

If this condition is verified, quadratic terms in the exponent of equation 2.7 can be discarded so that:

$$E(x,y,z) \simeq \frac{e^{ikz}}{i\lambda z} e^{\frac{ik}{2z}(x^2+y^2)}\iint_{\Sigma_0} E_0(x_0,y_0,0)\, e^{-i\frac{2\pi}{\lambda z}(x_0 x + y_0 y)}\, dx_0 dy_0 \tag{2.9}$$

This expression, in which the 2D spatial Fourier transform of the field in plane Σ_0 can be identified, is known as the Fraunhofer diffraction equation. We can introduce the Fresnel number F, which is commonly used to quantify the validity of the Fraunhofer approximation. It takes the form:

$$F = \frac{a^2}{z\lambda} \tag{2.10}$$

Where a stands for the characteristic size of the scattering object. If F is close to zero, the fraunhofer approximation can be applied: we are in the far-field regime as opposed to the near-field regime, for which the Fresnel integral is needed.

2.2 HOLOGRAPHY

Since holography was invented by Denis Gabor in 1947 [20], it has established itself as a powerful and versatile technique to recover the phase and amplitude of the light. The basic principle still remains very similar to Gabor's Nobel-prize-winning experiment. The light wave scattered from an object is combined with a second "reference" wave on a detector where their interference pattern is recorded. In early experiments, holograms were recorded and stored on a photosensitive material, and "reading", was done by exposing the hologram with another light source. In digital holography, the hologram is recorded with a camera, and decoded using numerical methods. Two holographic techniques were used in this thesis: Fourier transform holography (FTH), and off-axis digital holographic microscopy (DHM).

2.2.1 DIGITAL HOLOGRAPHIC MICROSCOPY

DHM consists in recording a microscopic image of a sample and make it interfere with a plane wave reference on a camera. Generally, a monochromatic light source is split in two separate beam path: one is focused on the sample, and either the reflected or transmitted light is captured by a microscope system to produce an image on the photodector ; The other beam path is used to produce a plane wave reference which is recombined with the "sample" wave using a beamsplitter placed before detection. A schematic of a basic experimental setup is displayed in Fig.2.2a. Intensity of the electric field on the camera can be expressed as [19, 21]:

$$\begin{aligned} I(x,y) &= \left|P(x,y)+R(x,y)\right|^2 \\ &= (P(x,y)+R(x,y))(P^*(x,y)+R^*(x,y)) \\ &= P(x,y)P^*(x,y)+R(x,y)R^*(x,y)+P(x,y)R^*(x,y)+R(x,y)P^*(x,y) \end{aligned} \tag{2.11}$$

with $P(x,y)$ the image of the near-field wavefront emitted from the sample, and $R(x,y)$ the reference wave. If we take the Fourier transform of this expression, we get:

$$\begin{aligned} FT\left[I(x,y)\right] &= FT\left[P(x,y)P^*(x,y)\right]+FT\left[R(x,y)R^*(x,y)\right] \\ &\quad + FT\left[P(x,y)R^*(x,y)\right]+FT\left[R(x,y)P^*(x,y)\right] \\ &= \hat{P}(f_x,f_y)*\hat{P}^*(-f_x,-f_y)+\hat{R}(f_x,f_y)*\hat{R}^*(-f_x,-f_y) \\ &\quad + \hat{P}(f_x,f_y)*\hat{R}^*(-f_x,-f_y)+\hat{R}(f_x,f_y)*\hat{P}^*(-f_x,-f_y) \end{aligned} \tag{2.12}$$

Where the hat symbol denotes a spatial Fourier transform, the $*$ symbol stands for a convolution product, and f_x and f_y are the reciprocal space coordinates. The reference wave is typically a plane wave:

$$R(x,y) = |R|e^{i\vec{k}\vec{r}} \tag{2.13}$$

The plane wave vector can be expressed in the spherical base defined by the angle ϕ between $\vec{k}$ and the z-axis (normal to the detection plane), and angle θ made between the projection of $\vec{k}$ on the x-y plane with the x-axis (see Fig. 2.2b). The coordinates of $\vec{k}$ in the cartesian coordinate system are:

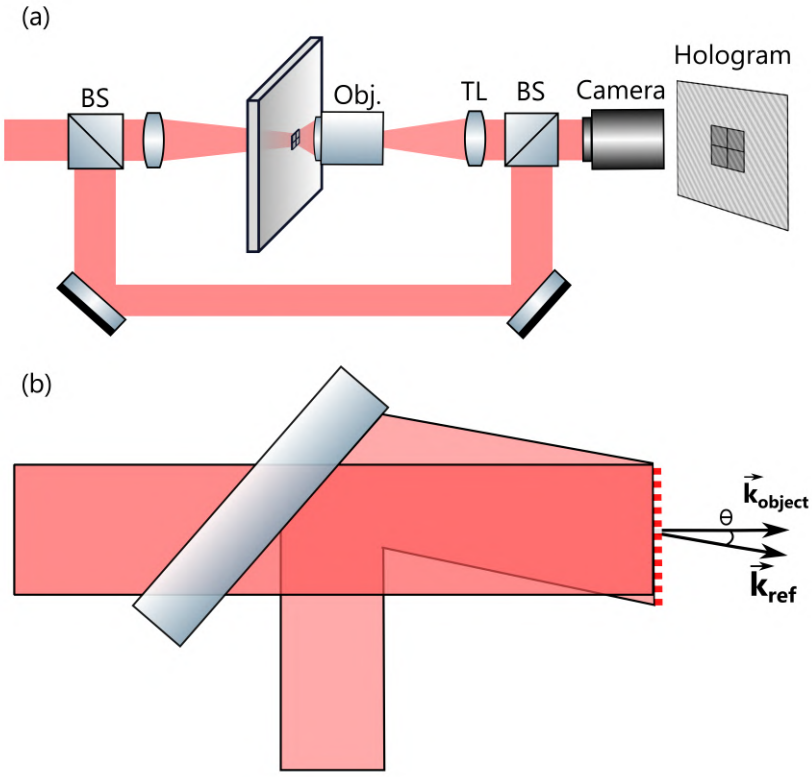


Figure 2.2: Schematic of a transmission DHM measurement. (a) A laser source is split in two beam paths: a first one is focused on the sample, and an image is produced by a microscope system composed of an objetive and a tube lens on a camera. (b) Close-up on the recombination beamsplitter. θ is the angle between wavevectors of both waves and conditions the fringes spacing recorded on the photodetector. BS: Beamsplitter ; Obj.: Objective lens ; TL: Tube lens.

$$\begin{aligned} k_x &= |\vec{k}|\sin(\phi)\cos(\theta) \\ k_y &= |\vec{k}|\sin(\phi)\sin(\theta) \\ k_z &= |\vec{k}|\cos(\phi) \end{aligned} \tag{2.14}$$

Since the measurement is made in the x-y plane, we have:

$$\begin{aligned} R(x,y) &= |R|\, e^{i(k_x x + k_y y)} \\ &= |R|\, e^{ik\sin(\phi)(\cos(\theta)x + \sin(\theta)y)} \end{aligned} \tag{2.15}$$

The spatial Fourier transform of a plane wave corresponds to a delta function in reciprocal space:

$$FT\left[R(x,y)\right] \propto \delta(f_x - \frac{k_x}{2\pi}, f_y - \frac{k_y}{2\pi}) \tag{2.16}$$

We can now inject this expression back in equation 2.12 to obtain:

$$\begin{aligned} FT\left[I(x,y)\right] = \hat{P}(f_x,f_y) * \hat{P}^*(-f_x,-f_y) + |R|^2\delta(f_x,f_y) \\ + |R|\hat{P}(f_x+k_x,f_y+k_y) + |R|\hat{P}^*(-f_x+k_x,-f_y+k_y)) \end{aligned} \tag{2.17}$$

The first term of this expression corresponds to the autocorrelation of the pattern distribution Fourier transform, centered on the spatial frequencies axis origin. The second term is an intense peak, also positioned at the origin. Finally, the last two terms can be identified as the Fourier transform of the pattern and its complex-conjugate, centro-symetrically flipped with respect to the origin. By cropping one of this two terms and performing an inverse Fourier transform, the spatial distribution of phase and amplitude emitted in the near-field of the pattern is obtained. Figure 2.3 illustrates how the different convolution terms are spread in Fourier space.

Special attention must be paid to angle θ between the wavevector of the pattern and reference wave: if it is too large, corresponding to a high-frequency fringes interference pattern in real-space, the pattern Fourier transform can be shifted out of accessible Fourier space window. If on the contrary the angle is too small, overlap with the DC terms at the origin can prevent from obtaining an accurate reconstruction.

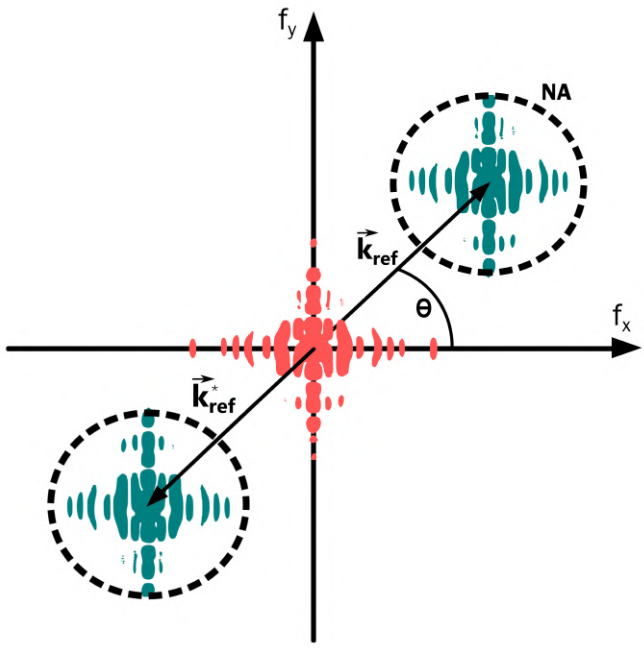


Figure 2.3: Illustration of the hologram Fourier transform. Convolution products $\hat{P}(fx+kx, fy+ky)$ and $\hat{P}(fx-kx, fy-ky)$ are centered on the frequency coordinates defined by the reference wavevector $\vec{k}_{ref}$. Extension of the diffraction patterns are limited by the NA of the optical system.

2.2.2 FOURIER TRANSFORM HOLOGRAPHY

FTH relies on the same core principle as DHM i.e. combining both an "object" and "reference" wave on a photodetector. However, in FTH, an image of the sample is not directly recorded, but its diffraction pattern is instead.

Equation 2.9 states that the far-field diffraction pattern is directly proportional to the Fourier transform of the field in sample plane.

$$E(x,y,z) \propto \iint_{\Sigma_0} E_0(x_0,y_0,0) e^{-i\frac{2\pi}{\lambda z}(x_0 x + y_0 y)} dx_0 dy_0 = FT\left[E_0(x_0,y_0,0)\right] \tag{2.18}$$

In FTH, the sample is prepared so that it is composed of two distinct elements. First is a 2D pattern of any kind which is the object we want to image in the experiment. It can be a fully or partially transmittive structure etched on a substrate for example. The second element is a reference feature, etched at some distance away from the pattern, which will scatter a wave with known characteristics (see Fig. 2.4a). We can express the wavefront in the sample plane by:

$$E(x_0,y_0,z=0) = P(x_0,y_0) + R(x_0,y_0) \tag{2.19}$$

Where $P(x_0,y_0)$ and $R(x_0,y_0)$ respectively stands for the pattern and reference 2D distributions of the field at $z=0$, which are directly linked to the complex-valued transitivity of the material:

$$P(x_0,y_0) \propto A(x_0,y_0) e^{i\phi(x_0,y_0)} \tag{2.20}$$

In which $A(x_0,y_0)$ is a metric of how much light was absorbed in the medium, and the exponential term describes its phase distribution. The intensity of the light is defined as the square absolute value of the electric field. Therefore, using equation 2.18 the intensity distribution in the far-field takes the form:

$$\begin{aligned} I(k_x,k_y) = |FT\left[P(x_0,y_0) + R(x_0,y_0)\right]|^2 &= |FT\left[P+R\right]|^2 \\ &= |\hat{P}+\hat{R}|^2 \\ &= \left(\hat{P}+\hat{R}\right)\left(\hat{P}+\hat{R}\right)^* \\ &= |\hat{P}|^2 + |\hat{R}|^2 + \hat{P}\hat{R}^* + \hat{P}^*\hat{R} \end{aligned} \tag{2.21}$$

where spatial dependencies were omitted for sake of conciseness, and where f_x and f_y stand for the reciprocal space coordinates. The Fourier transform of a multiplication being a convolution product, taking the inverse Fourier transform of equation 2.21 yields:

$$\begin{aligned} FT^{-1}\left[I(k_x,k_y)\right] = P * P^*(-x,-y) + R * R^*(-x,-y) \\ + P * R^*(-x,-y) + P^*(-x,-y) * R \end{aligned} \tag{2.22}$$

The most basic reference used for FTH is a hole, which scatters a spherical wave in the far-field (see Fig. 2.4b). If its diameter gets small with respect to the dimensions of the pattern to be imaged, we can approximate it by a Dirac δ function so that equation 2.22 becomes:

$$
\begin{aligned}
FT^{-1}\left[I(k_x,k_y)\right] &= P * P^*(-x,-y) + |R|^2\delta(x,y) \\
&+ P * |R|\delta(x+x_H, y+y_H) + P^*(-x,-y) * |R|\delta(x-x_H, y-y_H) \\
&= P * P^*(-x,-y) + |R|^2\delta(x,y) \\
&+ |R|P(x+x_H, y+y_H) + |R|P^*(-x+x_H, -y+y_H)
\end{aligned}
\tag{2.23}
$$

Where x_H and y_H stands for the coordinates of the reference hole. The first term of equation 2.23 is a delta function located at the centre. The second term describes an auto-correlation of the pattern distribution, also located in the centre. The third term and fourth terms describes the pattern distribution centred at the $(-x_H, -y_H)$ coordinates and its complex-conjugate, centro-symmetrically flipped, and centered at the (x_H, y_H) coordinates. Figure 2.4d) shows an example of an FTH reconstruction. As follows from equation 2.20, the transmittivity distribution is recovered by taking the absolute value of the reconstruction, and a phase reconstruction can be obtained by taking its complex angle.

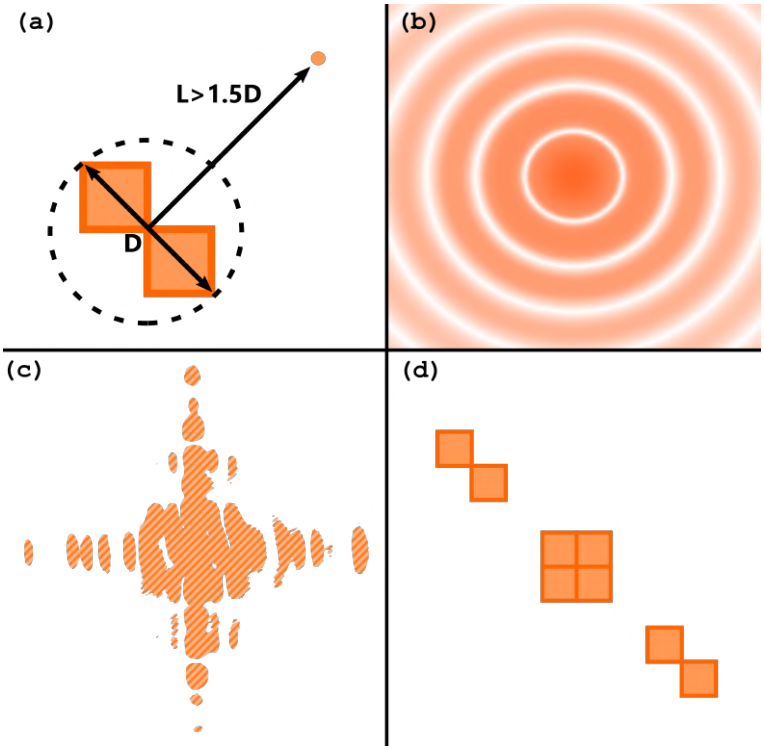


Figure 2.4: Illustration of the FTH reconstruction. a) A pattern and a reference hole are etched on the sample. The distance between the hole and the center of the pattern needs to be at least 1.5 time the diameter of the pattern's longest distance. b) Diffraction pattern emitted in the far-field by the reference hole. c) Hologram composed of the overlap of both the pattern and hole diffraction patterns, which gives rise to interference fringes. d) Inverse Fourier transform of the hologram.

Different kinds of reference have been tried over time. Multiple holes can for example be etched in such a manner that no overlap occurs in the final reconstruction. We can also cite the so-called Heraldo method which allows to to use more complex structures as references [22, 23].

In order to avoid any overlap of the different convolution terms in equation 2.23, it is necessary to impose a minimum distance between the reference hole and the pattern. The larger the pattern to be imaged, the more distant needs to be the reference hole from it. As a rule of thumb, it is generally preferable that the hole sits at a distance of at least 1.5 times the diameter (in the direction of the hole with respect to the origin) of the pattern to be imaged [24], as the dimension of the convolution product can be as big as two times the one of the object.

This rule comes with some issues. Because FTH is an interferometric technique, the intensity of the light scattered by the reference and the pattern needs to be of the same order. This means that the dimensions of the pattern cannot be so large compared to the hole. A solution is to make the hole larger in order to generate a more intense diffraction pattern in the far-field, but that comes with a loss in resolution as the reference hole deviates from a true delta function.

FTH is a technique of choice for performing imaging in the XUV/X-ray domain, where no optics are easily available for imaging [25–27] . Its use in the visible range has remained sparse, and limited to phase imaging of transparent micro-objects such as cells, as it do not display any significant advantage compared to standard digital holography except for an inherent accrued stability. Indeed, as both the reference and pattern diffraction patterns are generated from the same sample, the technique is far less sensitive to potential mechanical instabilities than standard holographic techniques which requires two beam to be recombined. Because our experiments are dealing with solid high harmonic generation which often suffers from low yield, stability was the key element which motivated us to investigate this particular technique.

2.3 HIGH-HARMONIC GENERATION IN SOLIDS

2.3.1 INTRODUCTION

Non-linear light matter-interactions were investigated since the early days of the laser invention. For instance, second-harmonic generation (SHG), which is the most straightforward manifestation of non-linear emission, was first demonstrated experimentally in 1961 by Franken et al [28]. The formalism developed to describe such processes is based on a perturbative approach. In the linear regime, the response of a medium to an external field $\tilde{E}(t)$ can be characterized by its polarization $\tilde{P}(t)$ [29]:

$$\tilde{P}(t) = \epsilon_0 \chi^{(1)} \tilde{E}(t) \tag{2.24}$$

where ϵ_0 is the free space permittivity and $\chi^{(1)}$ is the linear susceptibility second-rank tensor of the considered medium. In non-linear optics, this expression is developed into a power series of the applied electric field:

$$\tilde{P}(t) = \epsilon_0 \left[\chi^{(1)} \tilde{E}(t) + \chi^{(2)} \tilde{E}^2(t) + \chi^{(3)} \tilde{E}^3(t) + \ldots \right] \tag{2.25}$$

If we consider SHG, it can be understood as originating from the second order term of equation 2.25. Considering a monochromatic field $\tilde{E}(t)$ such that

$$\tilde{E}(t) = E_0 e^{-i\omega t} + \text{c.c.} \tag{2.26}$$

and inserting it in the second order term of 2.25, we have:

$$\begin{aligned} \tilde{P}^{(2)}(t) &= \epsilon_0 \chi^{(2)} (E_0 e^{-i\omega t} + \text{c.c.})^2 \\ &= 2\epsilon_0 \chi^{(2)} E_0^2 + (\epsilon_0 \chi^{(2)} E_0 e^{-i2\omega t} + \text{c.c.}) \end{aligned} \tag{2.27}$$

We obtain a polarization that oscillates at 2ω, producing light at the same frequency, therefore generating a second harmonic of the incoming field. In the quantum description of this process, second harmonic generation can also be understood as the annihilation of two photons with energy $\hbar\omega$ and the creation of one photon with energy $\hbar 2\omega$.

Major advances such as the invention of the Chirped-Pulse Amplification (CPA)[3] technique in the 1980's fueled the production of ever more intense pulses of light in the subsequent years, with durations down to the femtosecond time scale, enabling to explore new regimes of light-matter interaction, commonly denominated as strong-field regimes.

One of the most remarkable discoveries making use of these strong field interactions is high-harmonic generation, which was first demonstrated in 1987/1988 [5, 6]. By focusing an intense femtosecond infrared (IR) beam into a noble gas, a broadband spectrum composed of odd-harmonics of the fundamental driving field extending to the EUV could be observed, at much higher fluxes than anticipated from perturbative nonlinear optics. It was very soon understood that the generation of such large spectra emitted coherently could be used to form attosecond pulses. In 2001, the first experimental demonstration of attosecond pulse generation was published [30, 31]. This pioneering work initiated the development of attosecond science, which has allowed for some tremendous results since then [32]. These combined efforts were honored in 2023, when the Nobel prize was awarded to Anne L'Huillier, Pierre Agostini, and Ferenc Krausz.

In solids, the generation of harmonics beyond the perturbative regime was first demonstrated in 2011, with the work of Ghimire et al, who showed that high-harmonics up to the EUV range could be generated by focusing a NIR femtosecond laser on a ZnO sample. [7].

In the strong-field regime where both gas and solid HHG belong, the strength of the external field becomes comparable to the atomic or lattice potential experienced by electrons, and the perturbative approximation used in classical non-linear optics cannot be applied anymore [33]. Therefore, we will now present the semi-classical description that was developed to answer the need for a theory to support the experimental evidence of SHHG, partially adapted from the model describing gas-HHG.

2.3.2 SEMI-CLASSICAL DESCRIPTION

An established model for describing gas-HHG is known as the "three-step model" [34]. In this semi-classical description of the light-matter interactions, the atomic potential is strongly bent in one direction because of the intense electric field of the laser, which allows an electron from the outer shell of the atomic gas to tunnel out from the Coulomb potential. The electron is then accelerated, driven by the laser field, first moving away

from its origin and then accelerating back as the field changes sign. When the electron returns to its initial position, there is a probability that it is recaptured by its parent ion. When doing so, all the kinetic energy acquired through propagation in free space is converted into a high energy photon. The electron can take many different trajectories depending on the moment it was ionized with respect to the driving pulse. Therefore, photons emitted upon recombination can take a broad range of energy values.

The most significant approximation made in the three step model, which is not applicable to solids, is to consider the electron as a free particle whose trajectory in time and space is only affected by the electric field of the laser once it has tunneled through the potential of its parent ion. In order to describe HHG in solids, the periodic potential imposed by the crystal lattice has to be considered, which also makes the description of HHG in solids a lot more challenging than that for gasses.

Keeping the "three-step model" in mind, we start with the first tunnel ionization step. In solids, the allowed energies and momenta of electrons can be described by the electronic band structure theory, which results from the hybridization of atomic orbitals when packed together in a close arrangement. Thus, the electron can no longer be promoted to a free-space continuum of energy levels, as would be the case in gas. The electron gets excited from the energetically highest lying occupied band, called the valence band, to a more energetic band (conduction bands) above the Fermi level. For the sake of simplicity, we are now only going to consider promotion to the first conduction band.

Excitation from the valence to conduction band by absorption of a photon requires conservation of both energy and momentum. As a photon carries negligible momentum compared to an electron, a transition between two bands changes only its energy. This can be represented by a vertical arrow in the typical first Brillouin zone representation of the material band structure (see step one in figure 2.5).

In a similar manner to gas-HHG, the second step of this model consists in the electron being accelerated by the driving laser field. However, the influence of the lattice potential, which also affects the electron trajectory, results in new mechanisms at the origin of harmonic generation which have no equivalent in gasses. Therefore, because of the non-trivial nature of trajectories followed by electrons, a momentum-space representation is more intuitive when dealing with solids compared to gasses for which a real-space representation is preferred. However, it is worth mentioning that a real-space description can also be employed, via Wannier basis [35].

We will first consider the intraband HHG mechanism, which originates from the non-linear motion of electrons in conduction bands. If we consider an excitation by a linearly polarized field $\tilde{F}(t)$, and look at the electronic response along the same polarization, we can ignore the vectorial nature of the problem and consider 1D fields and polarizations. The electron motion in a band produces a time-dependent current density which can be expressed as [36]:

$$J(t) = \frac{-2e}{2\pi} \int_{BZ} v(k,t) g(k,t) dk \tag{2.28}$$

in which the electron current $j(t) = -eg(t)v(t)$, where e is the electron charge, $v_i(k,t)$ its velocity, and $g(t)$ the population of the conduction band, is integrated over the full

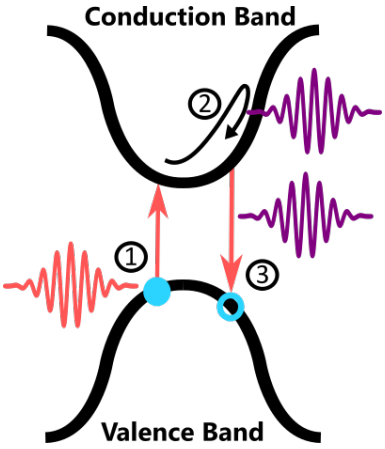


Figure 2.5: Illustration of the three-step semi-classical model for solid-HHG. (1) The electron is excited to the conduction band via tunnel ionization. (2) It is then accelerated in the conduction band by the NIR field. The non-linear motion of the electron gives rise to the generation of a broadband spectra (intraband generation). (3) The electron recombines with the hole left vacant in the valence band through emission of a photon (interband generation).

Brillouin zone. The electron velocity depends on the curvature of the band and can be written as follows:

$$v(k) = \frac{1}{\hbar}\frac{\partial E(k)}{\partial k} \tag{2.29}$$

In the tight-binding approximation, from which the band structure of most dielectrics can be derived, the dispersion of the band i.e the relationship between E and k can be expressed as a series of cosine functions:

$$E(k) = \sum_{n=0}^{n_{\max}} \epsilon_{\mathrm{n}} \cos(nka) \tag{2.30}$$

where $n_{\max}$ is the number of atoms in the solid along the considered crystal orientation, usually considered infinite, and a is the lattice constant. Replacing this expression in equation 2.29 yields:

$$v(k) = -\frac{a}{\hbar}\sum_{n=0}^{n_{\max}} n\epsilon_{\mathrm{n}} \sin(nka) \tag{2.31}$$

We consider interaction with a time-dependent electric field such that the electron crystal momentum can be written:

$$K(t) = k + \frac{e}{\hbar}A(t) \tag{2.32}$$

with $A(t)$ the vector potential of the field $F(t)$ and k the crystal momentum in the absence of external field. For a gaussian laser pulse of carrier frequency ω_0, we can write it as:

$$A(t) = -\frac{F_0}{\omega_0} P(t)\sin(\omega_0 t + \phi) \tag{2.33}$$

Where $P(t)$ is the envelope of the pulse. We have also implicitly assumed the dipole approximation to hold true ($F(x,t) \approx F(t)$). Inserting this new expression for momentum in equation 2.31 allows to rewrite the current density in equation 2.28 as:

$$J(t) = -\frac{ea}{\pi\hbar} \sum_{n=0}^{n_{\max}} n\epsilon_{\mathrm{n}} \int_{BZ} \sin(na(k + \frac{e}{\hbar}A(t)))g(k)dk \tag{2.34}$$

The spectral intensity of the field emitted by moving charges is proportional to the square modulus of the current density derivative with respect to time [36]:

$$I(\omega) \propto \left| \mathrm{FT}\left[\frac{\partial J(t)}{\partial t}\right]\right|^2 \propto \left| \mathrm{FT}\left[\sum_{n=0}^{n_{\max}} \int_{BZ} g(k,t)\frac{\partial v(k,t)}{\partial t}\right]\right|^2 \tag{2.35}$$

with FT standing for Fourier transforms. According to the expression of velocity we finally get:

$$I(\omega) \propto \left| \sum_{n=0}^{n_{\max}} C_{\mathrm{n}}(g(k,t))\delta(\omega - n\omega_0)\right|^2 \tag{2.36}$$

with delta functions rising from the Fourier transform applied to the sum of cosine functions composing velocity. We can stop at this equation to highlight how intraband generation has no equivalent in gas-HHG . If the electron is accelerated in free-space, the energy dispersion as function of k is a parabolic function. If we consider a conduction band with the same curvature, we can write the dispersion relation as:

$$E(k) = E_0 + \frac{\hbar^2 k^2}{2m} \tag{2.37}$$

with E_0 being the minimum energy of the band at $k = 0$. Thus, according to equation 2.29 the velocity becomes:

$$v(k) = \frac{\hbar k}{m} \tag{2.38}$$

if we consider interaction with the external field, we can replace k with $K(t)$ given in equation 2.32.

$$v(t) = \frac{\hbar}{m}(k + \frac{e}{h}A(t)) \tag{2.39}$$

The velocity is linear with the driving field and therefore only the fundamental frequency is non-zero in equation 2.36. The medium response to the external field is thus solely linear, resulting in light emission oscillating at the fundamental frequency ω_0. This demonstrates that acceleration in free space, which is a valid approximation for gas-HHG, does not produce harmonics, emphasizing the singular nature of intraband harmonic generation. It also shows that the curvature of the band, which determines the number

and intensity of higher order-terms in equation 2.34, is directly linked to the emission of light at a wavelength smaller than the fundamental.

After the electron spent some time in the conduction band, there is a probability that it recollides with the hole in the valence band through emission of a photon: this process is called interband generation. In contrast to gas-HHG, the photon energy is bound by the energy difference between conduction and valence band in the electric field. Therefore, harmonics produced through interband generation must have an energy larger than the direct bandgpap within this classical framework [11].

Although the relative efficiency between interband and intraband generation is variable depending on both the band structure, and the nature of the driving field, a general rule of thumb is that intraband generation predominates at lower harmonic orders, especially if the band gap requires many photons for tunnel-ionization, and that higher harmonic orders are mostly due to interband generation.

Both the interband and intraband processes are repeated in each cycle of the driving field, which results in a macroscopic emission composed of a set of discrete peaks, corresponding to odd-harmonics of the fundamental frequency (for an inversion symmetry medium).

2.3.3 MACROSCOPIC PROPERTIES

PHASE MATCHING

In order to accurately depict the macroscopic HHG emission from solids, the single atom picture is not enough. Emission from multiple atomic sites result in constructive or destructive interference, which can considerably affect the HHG signal emitted from the whole bulk. Therefore, to obtain the highest yield possible, atoms emitting harmonics along propagation of the driving field need to do so in phase. This condition can be achieved if the wavevector of the fundamental, k_{f}, and harmonic order q, k_{q}, satisfy:

$$\begin{aligned} \Delta k &= k_{\mathrm{q}} - q k_{\mathrm{f}} = 0 \\ &= n(q\omega_0)\frac{q\omega_0}{c} - q n(\omega_0)\frac{\omega_0}{c} = 0 \end{aligned} \tag{2.40}$$

Therefore, optimal phase matching requires $n(q\omega) = n(\omega)$. This condition is generally very hard to achieve in the UV, visible and NIR range because of the highly dispersive nature of most solids in these energy domains, but can be improved in the mid-IR, where the material response is less wavelength-dependent. Birefringent materials, which are characterized by an anisotropic refractive index which depends and the considered crystal axis, are commonly used to generate efficient SHG and THG light by allowing to tune the refractive index experienced by the different wavelengths. The most commonly used material for producing low-order harmonic in the visible and UV range is beta barium borate (BBO), which combines both a convenient birefringence and a high non-linear efficiency.

GOUY PHASE SHIFT

When a gaussian beam is focused, a π phase shift occurs after the beam waist [37]. This extra phase term, originating from the spatial confinement and deformation of the wavefront in focus, leads to some changes in the macroscopic HHG emission. Harmonic light

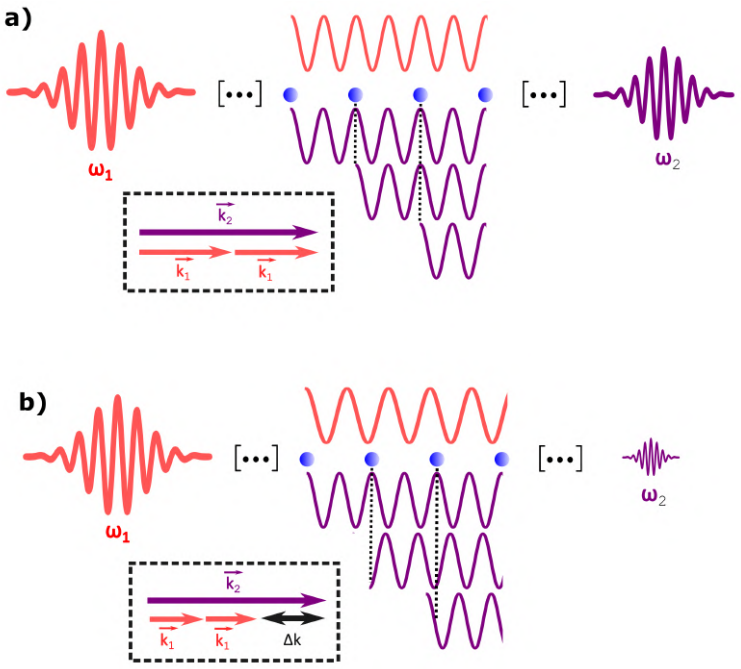


Figure 2.6: Illustration of the phase matching concept. In a), wave vectors of the fundamental and second harmonic satisfy $\Delta k = 0$. In real space, this corresponds to an in-phase SH emission from each atomic sites, which add up constructively and results in a strong macroscopic emission. In b), $\Delta k \neq 0$, and emission from atomic sites are not in phase. The macroscopic emission is therefore much weaker than in a).

emitted at position $-x$ with respect to the waist, interfers destructively with the light emitted at position $+x$, which is π phase-shifted. Therefore, if the beam used for driving HHG is focused at the plane standing at equal distance from the back and front surface of the medium, all contributions emitted before focus are cancelled by the ones emitted after focus, resulting in a null net yield. Careful attention must therefore be given to the focusing position with respect to the sample in order to obtain high HHG yields. Moreover, this π phase shift can also lead to misleading in interpretation of the measured HHG phase.

OPTICAL KERR EFFECTS

Focusing intense electric fields in solids can modify light propagation, and alter the subsequent harmonic generation. In intensity regimes suitable for HHG, the medium response to the electric field can induce changes to the refractive index on a subcycle time scale. The most basic manifestation of such phenomena can be attributed to $\chi^{(3)}$ non-linear processes, also known as Kerr optical effect. In this model, the refractive index is modified from its unperturbed state n_0 by the addition of a term which depends linearly on the intensity of the external field [38]:

$$n = n_0 + n_2 I \tag{2.41}$$

in which n_2 is the so-called Kerr non-linear coefficient and I is the intensity of the field. Spatially, this equation implies that different areas of the pulse experience a distinct refractive index, because of the inhomogeneous intensity distribution of the gaussian beam. This effect can result in self-focusing of the beam along its propagation axis, causing the so-called filamentation, which can induce some severe damage to the solid medium. Temporally, equation 2.42 implies that the latter part of the pulse, interacting at a given position in the sample, experiences a different refractive index than the early part of the pulse. This leads to a time dependent phase accumulation which can be expressed as:

$$\phi(t) = 2\pi\lambda n_2 I(t) L \tag{2.42}$$

This effect, called self-phase modulation, results in a spectral broadening of the fundamental field, and an increased chirp of the pulse, meaning wavelength are getting desynchronised, which leads to a longer time duration and a decrease in peak intensity. Therefore this affect harmonic generation in two ways: harmonics are spectrally broaden, but the overall yield is diminished. This phenomenon can be observed experimentally by measuring the HHG-yield in transmission from samples with different thicknesses, and needs to be accounted for if we are interested in comparing the relative phase between multiple harmonic orders.

2.3.4 APPLICATIONS OF SOLID-HHG

A wide number of applications were investigated to take advantage of the specific nature of SHHG. A first one, is the development of compact coherent EUV sources, with part of the research on SHHG being primarly focused on extending the energy cut-off, and increasing the yield, of harmonic emission. For instance we can report attempts made at combining multiple driving field in order to push conversion efficiency [39, 40].

The generation mechanisms behind SHHG make it an excellent probe of the band structure, as any slight electronic reorganization leads to variations in the harmonic emission [8, 41–43]. Therefore, pump-probe implementations, in which a first ultrashort pulse is focused in a material, and a second NIR beam is used to generate harmonics, are used to study the transient dynamics following pump excitation. A standard measurement consists in recording the spectra at different time delays between pump and probe, but alternative observables such as the spatially resolved emission, the polarization dependence [44, 45], or the harmonics phase content were also investigated [46, 47].

Measurements can be compared to ab-initio simulations in order to extract meaningful information on the physics taking place in materials. There are two main approaches to simulate SHHG. A reciprocal space approach, which typically combines solving Semiconductor Bloch Equations (SBEs) and applying Time-dependent Functional Theory (TDSE)[10], and a real-space one, through the mediation of the Wanier basis.

Investigation of quantum materials using SHHG has drawn a lot of attention recently. This category of materials encompasses all solids that show evidence of their quantum

nature, unexplainable by classical means, such as topological insulators [48], transition metal dichalcogenide monolayer materials (TMDCs) [49], and strongly correlated electron systems [13, 50]. That is precisely on this last kind that part of the research conducted in this thesis is going to be concerned with.

2.4 CORRELATED ELECTRON SYSTEMS

Band theory arose from the development of quantum mechanics in the the first half of the twentieth century and is still the most successful model for characterizing electrons in matter. When atoms are packed together in a solid, the discrete set of atomic energy levels are reshaped into continuous functions named bands. The metallic or insulator nature of solids can be determined by the electron population in the last occupied band: If the last occupied band is completely filled, electrons cannot move around freely when a force is acting upon them, therefore prohibiting current in the solid, which is not the case for a partially-filled band. The last occupied energy level at equilibrium defines the Fermi level, which lies in the last occupied band for metals, and in the band gap between the last occupied band (valence band) and the next more energetic band (conduction band) for dielectrics.

This theory could also provide an interpretation for the behavior of semiconductors: if the band gap between valence and conduction band is small enough, it was predicted that electrons could be excited from the first to the latter one, either thermally or optically, and that a transient conducting state could be created. This hypothesis lead to the invention of the transistor in 1948 [1].

Although this model was very successful at describing electronic properties of most solids, it failed to explain the behavior of some materials such as transition metal-oxides and perovskite oxides with a partially-filled d or f band: some of these solids would exhibit a very poor conductivity, inconsistent with the band theory, which would predict them as metals [51]. This flow originates from an approximation in the band theory: electron-electron interactions are neglected, which is, in most cases, a valid approximation. However, when they are so strong it prevents free electron mobility in the solid, some theoretic metals behaves like insulators. Materials of this kind are known as strongly correlated electron systems.

Mott and Peierls were the first to predict that if enough energy would be injected into such materials, an insulator-to-metal transition (IMT) could be observed [52, 53]. This observation lead to over sixty years of both experimental and theoretical efforts in order to understand and control these transitions, which are of particular interest for their potential applications as next generation memristors devices, i.e., materials with a tunable resistivity, sensitive to a small external perturbation [54, 55].

We are going to focus on the specific case of d-electron metal-oxides. In these systems, metal atoms form strong covalent bonds with oxygens atoms and most of the optical, electric, and magnetic properties of the material are governed by the d-electrons, not involved in those bonds. The 5 atomic orbitals of the d-band are split in two energy levels: The lower energy t_{2g} band, composed of orbitals, d_{xy}, d_{xz} and d_{yz}, and the e_g band, composed of orbitals $d_{x^2-y^2}$ and d_{z^2} pointing directly towards ligands, therefore higher in energy. Among d-electron metal oxides which can undergo an IMT, VO_2 is probably the most well-known [56]. It displays a low-temperature monoclinic structure (M1) and a

high-temperature rutile structure (R) with a critical temperature of around 340 Kelvin. In both phases, VO_2 is slightly distorted from a perfect octahedron structure, which results in a splitting of the t_{2g} band between a $d_{||}$ orbital, pointing along the V-V chain, and two π^* orbitals, which are higher in energy.

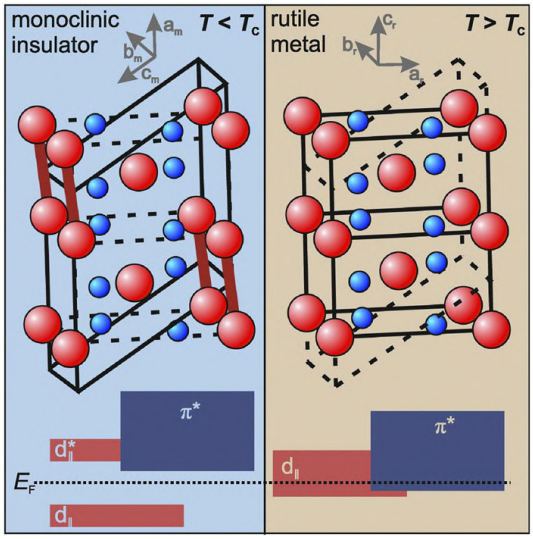


Figure 2.7: VO_2 crystal structure for the (left side) low-temperature monoclinic insulator phase and the (right side) high-temperature rutile metal phase and corresponding band structure near the Fermi level. Diamerization of the V-V chain is highlighted by red connections between atoms. Figure from [57].

The low-temperature phase is characterized by dimerization between vanadium atoms along the c-axis which induces another degeneracy lift with a splitting of $d_{||}$ orbitals between a bonding and anti-bonding state. Because vanadium has a single d^1 electron, the bonding state is completely filled and the Fermi level lies in the bandgap between the bonding $d_{||}$ and π^* bands. In the high-temperature phase, the dimerization vanished, which reestablishes the symmetry of $d_{||}$ orbitals, therefore closing the bandgap: VO_2 becomes metallic.

The exact mechanism driving the IMT in VO_2 has been debated for long, and mainly two models have been considered: the Peierls transition, in which the IMT is primarily dictated by the dimerization process, or the Mott transition, triggered by electronic correlations, which implies an ultrafast metallic phase preexists in the material before reorganization of ion sites [58]. Because the timescale of ion motion is orders of magnitude slower than electrons, a way to discriminate the two models is to track band structure modifications as function of time. Because heating is not an instantaneous process, measuring an observable while increasing or decreasing the temperature, allows to characterize the individual insulating and metallic phases, but prohibits from investigating the exact mechanism triggering IMTs. However, thermal heating is not the only way to trigger an IMT. A phase transition can also be photo-induced by a sufficiently intense laser beam through excitation of carriers. Owing to the ultrafast nature light-matter interactions, investigation of the exact mechanisms responsible for IMTs are therefore in reach. Pump-

probe experiments in which a first pulse is used to excite the material, and a second one is used to probe the subsequent electron dynamics, are widely reported in the literature. We can mention techniques such as linear reflection/transmission spectroscopy [59–61], photoelectron spectroscopy, Raman spectroscopy[62], X-ray lensless imaging[63, 64], or non-linear microscopy [65] as a few examples.

The correlated material studied in this thesis is niobium dioxide (NbO_2). Niobium is positioned just beneath vanadium in the periodic element chart, therefore sharing a similar electronic structure, with a single d-electron. Similarly to VO_2, NbO_2 present an IMT, but at a higher temperature of around 1080 K, and almost the same crystalline reorganization, with a low-temperature monoclinic phase, and a high-temperature rutile phase. The same dimerization mechanism is also present, and the debate regarding the exact nature of the IMT is essentially the same as in VO_2, therefore motivating experiments carried on NbO_2 in this thesis.

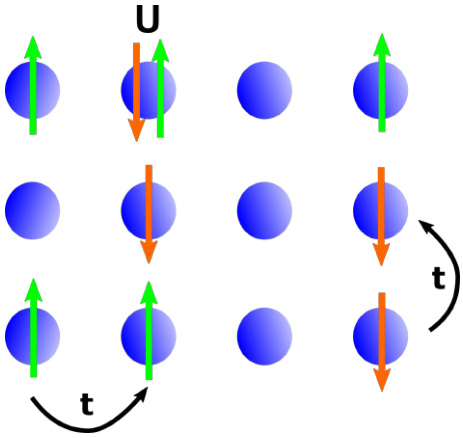


Figure 2.8: Illustration of the 2D Hubbard model. Atomic sites, symbolized by an blue sphere, have a default electron occupancy of one. If an electron overcomes the on-site repulsion energy U, it can share a site with another electron of opposite spin. The probability of double occupancy is dependent on the protected space between amplitude and t.

HHG in Mott insulators The Hubbard model can help us to understand how the case of correlated materials differs from traditional semiconductors regarding harmonic generation [66]. In this simplified picture, where we consider one kind of equivalent and equidistant orbitals located on each atomic site, the hamiltonian is written as:

$$H = -\sum_{<i,j>,\sigma} v_{ij} c^{\dagger}_{i,\sigma} c_{j,\sigma} + U \sum_{i} n_{i\uparrow} n_{i\downarrow} \tag{2.43}$$

where v_{ij} is the hopping amplitude between neighboring sites i and j, U is the on-site Coulomb repulsion between two electrons, $c^{\dagger}_{i,\sigma}$ and $c_{j,\sigma}$ are respectively the creation and annihilation operator at site i, for a spin σ, and n_i is the number operator, also equal to $c^{\dagger}_{i,\sigma} c_{j,\sigma}$. We can see from this equation that the on-site interaction U needs to be overcome to allow for hoping between atomic sites. Quasi-particles formed by

two-electrons sharing the same site are named doublons, whereas sites left with a vacancy are called holons. In the specific case of VO_2 and NbO_2, this corresponds to the excitation of electrons from the bonding $d_{||}$ band, with only one electron-per-site states, to the two-electron-per-site states antibonding $d_{||}$ band. Once a doublon is created, it can be accelerated in the band, and recombined to the ground states in a similar manner to an electron in semiconductors, therefore generating harmonics.

As discussed in the previous chapter, SHHG is particularly sensitive to the band structure, and therefore can be used as a tool to get more insights on the ultrafast dynamics taking place during IMTs. Measurements of HHG spectra were reported in multiple Mott insulators [66], including transient pump-probe experiments where a pump excites the material, and a second beam generates harmonics [67–69].

3

METHODS

3.1 LASER SOURCE

All experiments reported in this thesis were done with a Ti:saphire laser (*Astrella* system manufactured by *Coherent*).

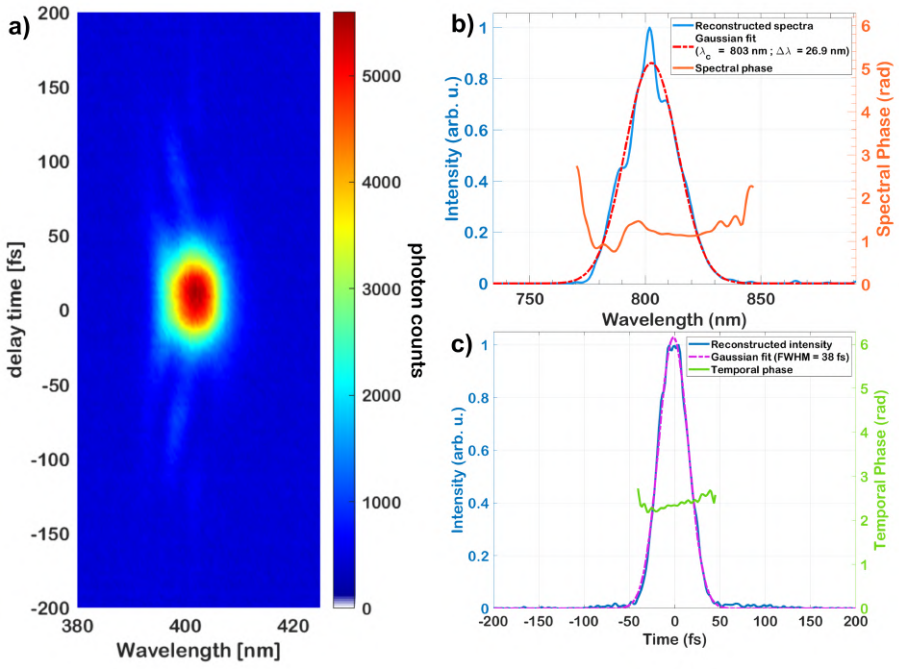


Figure 3.1: FROG measurement of the Astrella output used for the OPA. a) 2D FROG trace of the Astrella output. b) Reconstructed spectra, characterized by a central wavelength of 803 nm and a FWHM bandwidth of 26.9 nm. c) Reconstructed field intensity displaying a FWHM duration of 38 fs.

The system is composed of four main stages: an oscillator, a stretcher, a regenerative amplifier, and a compressor. The oscillator, labeled *Vitara*, provides femtosecond pulses with a central wavelength of 815 nm, a bandwidth of 60 nm, at a repetition rate of 80 MHz and an average power of 600 mW. This ouput is stretched in time using a grating stretcher in order to reduce its peak intensity and avoid damage to the second Ti:sapphire crystal used in the amplification process. The amplification cavity is gated by two Pockels cells: one of the stretched pulse is picked up, goes 13 roundtrip in the cavity of the regenerative amplifier, and is rejected out from the cavity. At every roundtrip, the pulse is focused inside the Ti:sapphire crystal along side a pump beam with a central wavelength of 532 nm, used to create the population inversion. Finally, the beam goes into the grating compressor to resynchronize the broadband spectra, allowing to reach the highest possible intensity. The final pulses are characterized by a central wavelength of 803 nm with a repetition rate of 1 kHz, an energy per pulse of around 8 mJ, and a FWHM duration of 35 fs, as presented in the FROG measurement in Fig. 3.1 [70].

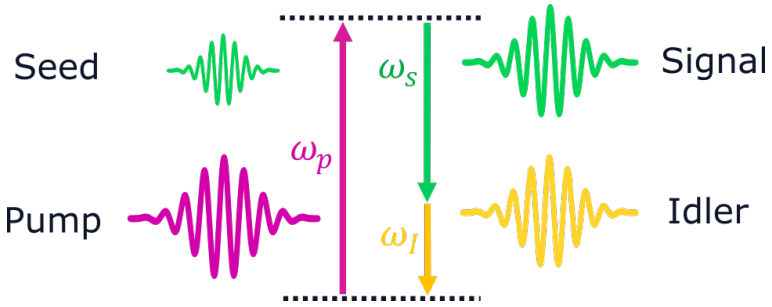


Figure 3.2: Energy diagram of the parametric down conversion process used in the OPA. A pump photon ω_p is converted to two lower energy photons ω_s and ω_I, the signal and idler photons. A seed pulse corresponding to the signal wavelength is combined with the pump to favor emission at this specific wavelength.

5 W of the *Astrella* is used to pump an optical parametric amplifier (OPA) (HE-TOPAS manufactured by *Light Conversion*), in order to generate light in the NIR. The beam is first divided into two: most of the energy is used as a pump for the final amplification, and the remaining energy is used to produce the seeding signal and idler. This second beam path is first focused in a crystal to produce a white light continuum via the optical Kerr effect process as explained in chapter 1. The beam is then focused in a non-linear crystal together with an auxiliary 800 nm beam to induce parametric down conversion, therefore producing both idler and signal photons, as illustrated in Fig. 3.2. The white-light continuum being strongly chirped, tuning the relative time delay between the 800 nm and NIR beam allows to choose which wavelength to select as a seed for the parametric down conversion, the much shorter 800 nm pulses acting as a gate. The signal and idler beam undergo a first pre-amplification using the same parametric down conversion process, and a last amplification is finally done by combining the beam with the high energy pump which was isolated after the OPA entrance. The system can deliver pulses ranging from 1150 to 2400 nm with variable efficiency. Maximum conversion efficiency is achieved for a idler wavelength of 1.8 μm, with an output power of around 1.0 W for the signal, and 0.5 W for the 1.45 µm idler.

3.2 NANOFABRICATION

Deposition of metallic thin films was done using sputter coating (LEICA ACE600 sputter coater visible in Fig. 3.3a), which consists in ejecting atoms from a solid target to deposit them on a substrate. Both target and substrate are placed together in a vacuum chamber where an inert gas, typically Argon, is injected, and a high voltage is applied to ionize the gas and form a plasma. The positively charged ions are accelerated towards the target, set to a negative potential. The impact knocks off atoms, which are deposited on the substrate.

For dielectric thin film deposition, another technique called plasma enhanced chemical vapor deposition was used (Oxford PlasmaPro100 ICPECVD, visible in Fig. 3.3b). A gas, containing the element of interest, is injected in a low-pressure chamber. A high-frequency electric field is applied to ionize the gas, creating a plasma composed of elec-

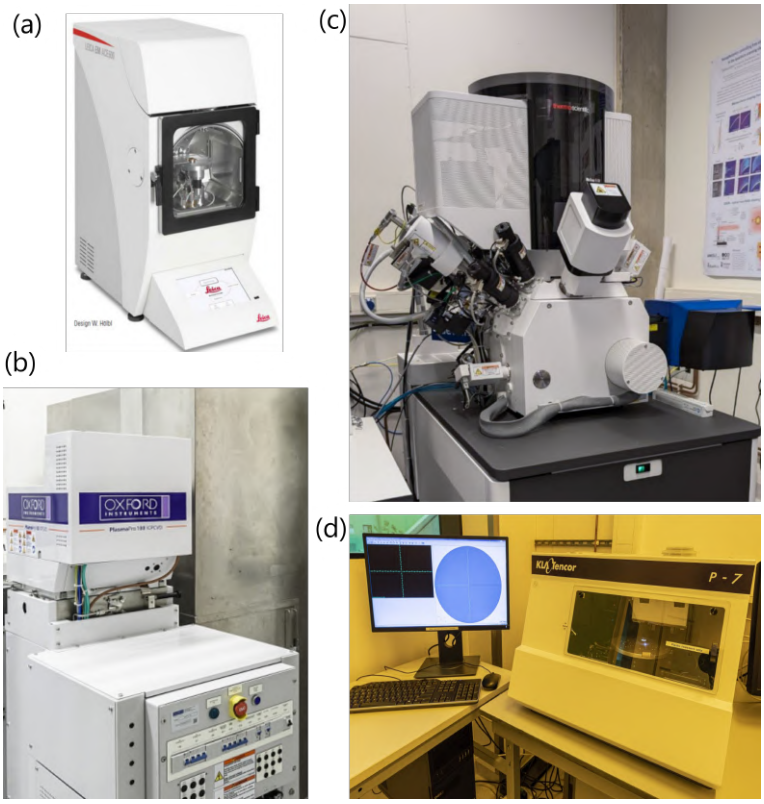


Figure 3.3: (a) LEICA ACE600 sputter coater ; (b) Oxford PlasmaPro100 ICPECVD ; (c) HELIOS dual-columm SEM and FIB ; (d) KLA Tencor Stylus Profiler P7.

trons, ions and excited molecules. Volatile molecules are pumped away, while species of interest react with the substrate to form a thin film. This technique was used to coat silicon, using the dissociation of a gas made of SiH_4 molecules.

Etching and characterization of nanostructures was done using a dual-column scanning electron microscope (SEM) coupled with a focused-ion beam (*HELIOS* manufactured by *Thermo Fisher Scientific* visible in Fig. 3.3c). SEM imaging is performed by focusing an electron gun to the sample using electromagnetic lenses. Secondary electrons emitted from the surface are collected and sent to detectors using magnetic fields. Therefore, by scanning the beam across the surface of the sample, an image is obtained. For etching, an ion source is focused on the sample in a similar way to the electron beam, and hit the surface of the sample with enough energy to eject atoms.

Height characterization was done using a profilometer (KLA Tencor Stylus Profiler P7, visible in Fig. 3.3d). A diamond-tip stylus is scanned across the peaks and valleys of the surface, moving up and down accordingly. These vertical movements are detected by a high-precision sensor and converted into a height profile.

Training on the multiple tools used for nanofabrication was done under the supervi-

sion of the Nanolab team of the AMOLF institute in Amsterdam. For more information on these different techniques, we can forward the reader to the complete review on nanofabrication done by Stepanova [71].

3.3 NUMERICAL METHODS

3.3.1 COMPUTATION OF FIELD DISTRIBUTIONS IN NANOSTRUCTURES

COMSOL multiphysics is a physic simulation software relying on finite element analysis. It was used to compute the fundamental field distribution in grating nanostructures in order to extrapolate the harmonic far-field amplitude and phase distributions.

Figure 3.4a shows how a grating unit cell is constructed in COMSOL. Periodic boundary conditions are set between the two lateral limits of the cell, and *perfectly matched layer*, corresponding to artificial absorbing region with no reflection, are set at the bottom and top extremities of the cell. The fundamental field is inputted via a *port* at either the top or bottom of the cell. The field distribution for a 2 µm plane wave input polarized orthogonally to the plane of the 2D unit cell is plotted in Fig.3.4b.

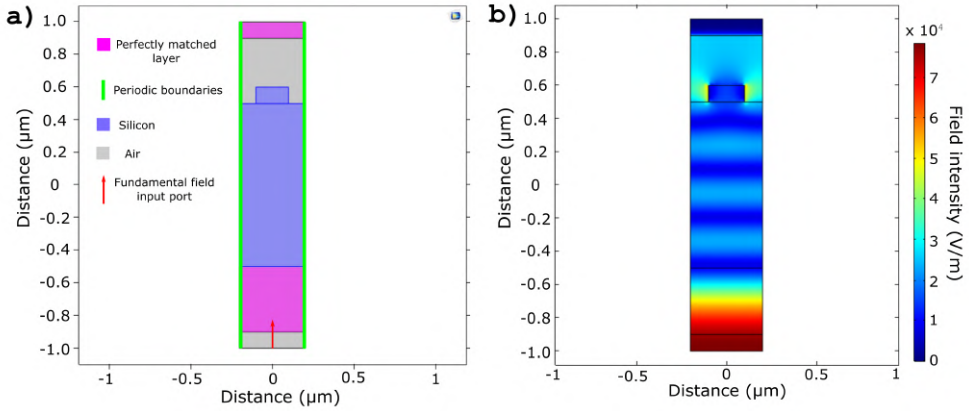


Figure 3.4: a) Plot of the grating unit cell constructed in COMSOL. b) Field distribution for an plane wave input with a central wavelength of 2 µm, polarized orthogonally to the plane of the 2D unit cell.

3.3.2 HIGH DYNAMIC RANGE IMAGE STITCHING

Diffraction pattern measurements often suffer from the limited dynamical range of cameras. The central zeroth order is typically orders of magnitude more intense than higher frequency terms, which makes acquisition of the whole diffraction pattern in a single measurement hard to achieve. A solution to this problem is to stitch together multiple images acquired at different integration time. We used the built-in Matlab function *makehdr* which implements the Debevec stitching procedure [72]. It consists in recovering the response curve of the camera, who is expected to be non-linear, by comparing the value at each pixels for different exposure time, and solve the associated system of equations. Using this curve, a stitched image is produced, replacing overexposed pixels in one image

with valid data from a darker exposure, and filling underexposed pixels in one image using brighter exposures. An example of HDR stitching is provided in Fig. 3.5.

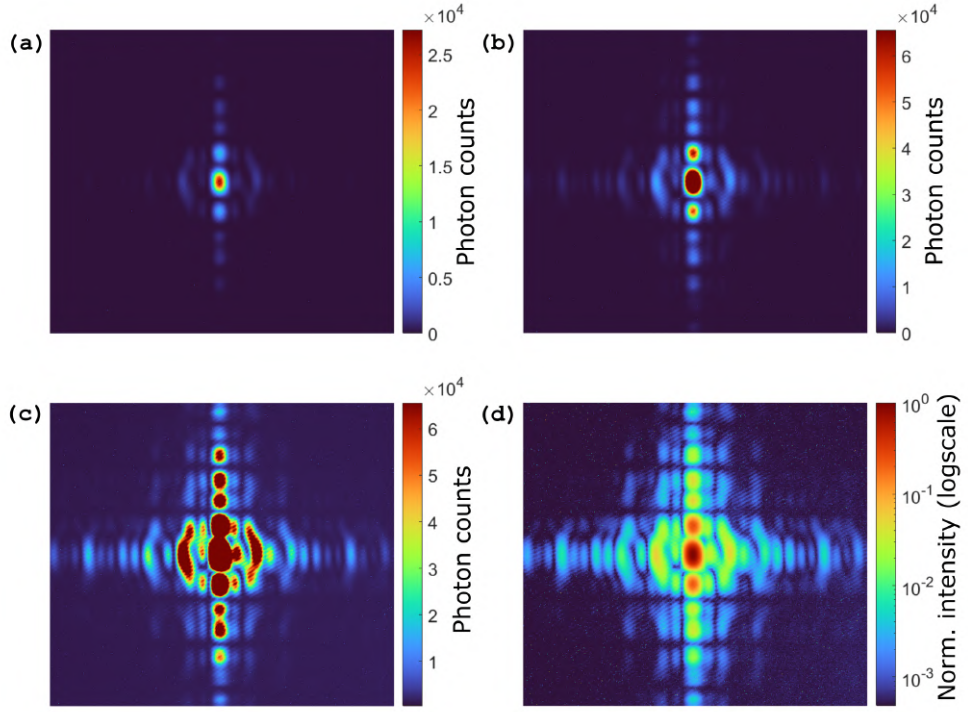


Figure 3.5: Illustration of HDR stitching using three images acquired with different integration times: (a) = 10 ms ; (b) = 100 ms ; (c) = 1000 ms. The stitched image using Debevec algorithm is presented in (d).

3.3.3 FOURIER RING CORRELATION

Optical systems cannot capture the most fine spatial features of an object, and always act as a Fourier-space shortpass filter. Fourier ring correlation is a method used to estimate spatial resolution by determining the cut-off frequency above which no information is carried.

A Fourier transform is applied to an image, and frequency components with the same absolute value, forming a ring around the origin, are binned together. The same steps are applied to a second image of the same object of interest, with independent noise realization, and the degree of correlation between the frequency bins of each image is calculated using [73**?**]:

$$FRC(r_i) = \frac{\sum_{r \in r_i} F_1(r) F_2^*(r)}{\sqrt{\sum_{r \in r_i} F_1^2(r) \sum_{r \in r_i} F_2^2(r)}} \tag{3.1}$$

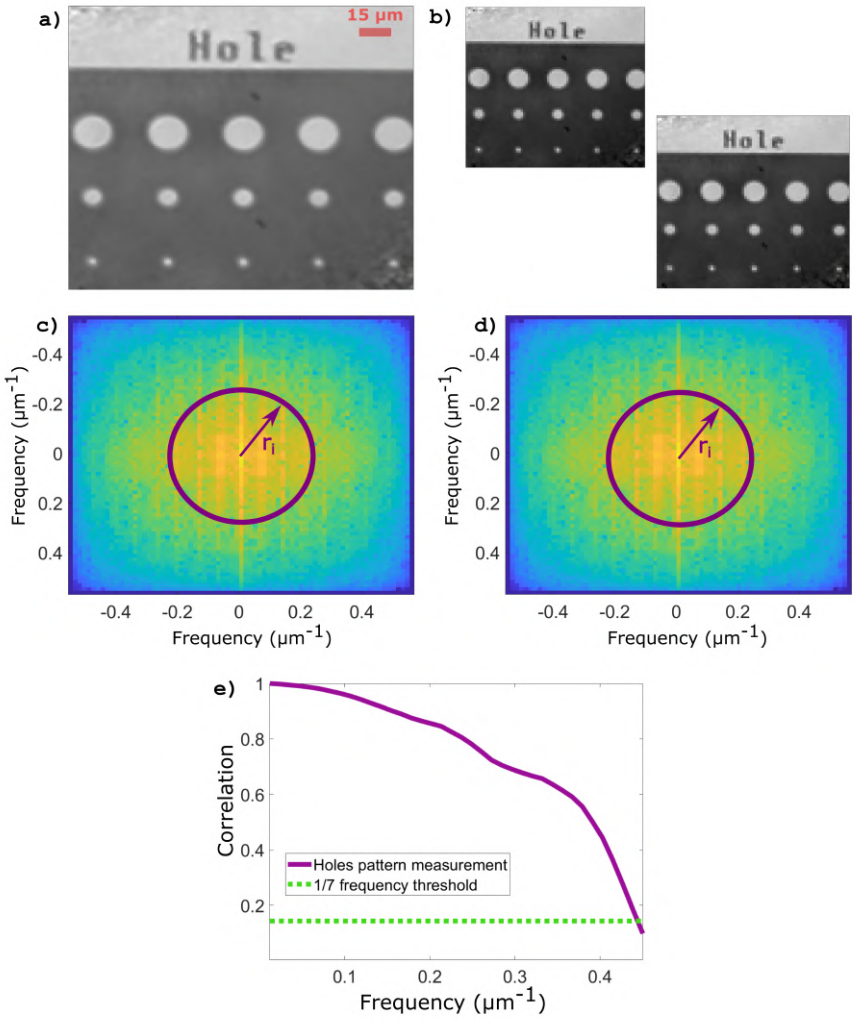


Figure 3.6: Illustration of the Fourier ring correlation method. a) Microscope image of a micron-scale array of holes. b) Image a) is split in two sub-images: one is composed of odd pixels along x-axis and even pixels along y-axis of a), and the other way around for the second sub-image. c) and d) are the Fourier transforms of the two sub-images. For a given purple circle of radius r_i, correlation between c) and d) are calculated using formula 3.1. e) Correlation as function of spatial frequency. Crossing with the 1/7 threshold line indicate the resolution of the image a), here equal to 1/0.438 = 2.28 µm.

where $F_1(r)$ and $F_2^*(r)$ are the Fourier transforms of image 1 and 2, and r_i is the frequency bin number i. This method can also be applied to single images: the measurement is split in two sub-images following the procedure described in Fig. 3.6, and the same correlation calculation is used. In general, the degree of correlation is expected to be close to one at lower frequencies, and to diminish as the frequency becomes larger. A

common standard is to define the frequency crossing down a correlation level of 1/7, as the cut-off corresponding to the inverse of the image resolution [74].

3.3.4 ANGULAR SPECTRUM FIELD PROPAGATION

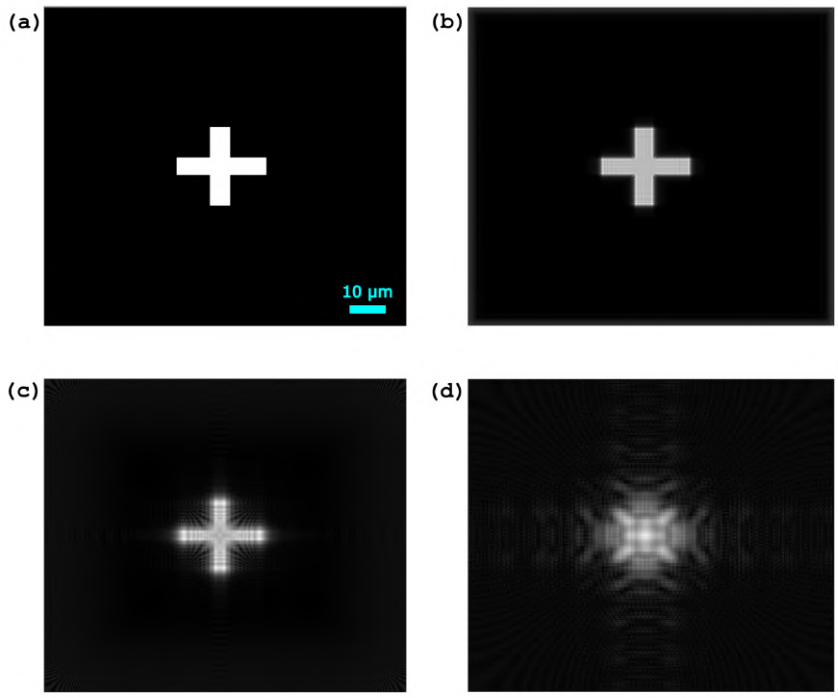


Figure 3.7: Plane wave of wavelength 800 nm is propagated from a cross pattern using the angular spectrum method for different distances z: (a) pattern ; (b) $z = 1$ µm ; (c) $z = 10$ µm ; (d) $z = 100$ µm.

The angular spectrum method was used to propagate fields in order to simulate measurements (FTH and DHM) and to correct for offsets in focusing of the imaging system in DHM measurements. Whereas both Fresnel and Fraunhoffer formulas can be used to propagate fields in, respectively, the near-field and far-field regimes, the angular spectrum method, can be used regardless of the distance from the sample, although it can sometime produce numerical errors. It consists in propagating each Fourier component of the field (its angular spectrum) separately, summing all contributions, and taking the inverse Fourier transform. The initial field can be expressed as an inverse Fourier transform of a function $\hat{E}(f_x, f_y, z)$ [75]:

$$E(x, y, z) = \iint_{-\infty}^{+\infty} \hat{E}(f_x, f_y, z) e^{i2\pi(f_x x + f_y y)} dxdy \tag{3.2}$$

The field needs to satisfy Helmholtz wave equation such that:

$$(\nabla^2 + k^2)E(x,y,z) = 0 \tag{3.3}$$

By replacing E(x,y,z) by its expression in equation 3.2, changing order between integration and differentiation, and using the fact that if the integrand is zero, the integral is also zero, we can write:

$$\nabla^2 \left[\hat{E}(f_x, f_y, z) e^{i2\pi(f_x x + f_y y)} \right] + k^2 \hat{E}(f_x, f_y, z) e^{i2\pi(f_x x + f_y y)} = 0 \tag{3.4}$$

Since the angular spectrum $\hat{E}(f_x, f_y, z)$ is composed of a sum of plane waves propagating along the z direction with no dependence on x or y, we can isolate the second-order derivative of the angular spectrum with respect to z:

$$\frac{\partial^2}{\partial z^2} \left[\hat{E}(f_x, f_y, z) \right] + (2\pi)^2 \left(\frac{1}{\lambda^2} - f_x^2 - f_y^2 \right) \hat{E}(f_x, f_y, z) = 0 \tag{3.5}$$

where we used $k = \frac{2\pi}{\lambda}$. A general solution to this differential equation can be written as:

$$\hat{E}(f_x, f_y, z) = \hat{E}(f_x, f_y, 0) e^{i2\pi z \sqrt{\frac{1}{\lambda^2} - f_x^2 - f_y^2}} \tag{3.6}$$

from which we can define the angular transfer function

$$H(f_x, f_y) = e^{i2\pi z \sqrt{\frac{1}{\lambda^2} - f_x^2 - f_y^2}} \tag{3.7}$$

Therefore, in order to obtain the field at any distance z, we need to numerically compute the Fourier transform of the field at the origin, propagate it using the transfer function $H(f_x, f_y)$ to obtain the angular spectrum at distance z, and finally do an inverse FFT to get the real-space field distribution. An example of field propagation is provided in Fig. 3.7.

4

NON-LINEAR DIGITAL HOLOGRAPHIC MICROSCOPY FOR RECONSTRUCTION OF SUBWAVELENGTH STRUCTURES

Digital holographic microscopy (DHM) is a successful technique frequently used to assess the phase in imaging experiments. Combining DHM with nonlinear generation opens the possibility of measuring phases in nonlinear processes such as high-harmonic generation and characterize nanostructures with an increased sensitivity.

In this paper, we demonstrate that the combination of DHM and harmonic generation from solids can be used to reliably perform 3D reconstructions of samples, but also investigate structural parameters of sub-wavelength periodic structures with improved accuracy. We were able to discriminate gratings etched in silicon, with only a few tens of nanometers change in critical dimension, down to a pitch of 400 nanometers, which is well below the wavelength of the near infrared (NIR) probing laser source.

This technique can in principle be used with all high-harmonic emitting materials, and is expected to reach even larger gains in resolution by probing higher order harmonics. These results pave the way for sensing of sub-wavelength structures via nonlinear light generation, for instance, in the semiconductor industry.

This chapter is based on: L. Guery et al.(2026), Digital Holography Using Harmonic Generation from Solids for Reconstruction of Subwavelength Nanostructures. *ACS Photonics* 13(4), 1055-1064.

4.1 INTRODUCTION

While conventional microscopy only measures intensity patterns, the phase is crucial to conduct an accurate 3D reconstruction. Measuring both amplitude and phase enables reconstruction of both real and imaginary parts of the refractive index, thus enhancing contrast between different materials compared to images obtained by only considering amplitude. More generally, measuring phase is a necessity in order to obtain a complete picture of light-matter interactions in a sample.

A number of well established techniques allow for phase sensitive imaging, for instance holography, in all its variants (including DHM) [20, 24, 76], ptychography [77], and coherent-diffraction imaging [78]. The latter two are usually recorded in Fourier space and thus generally preferred when performing measurements where no optics for re-imaging are available i.e. for wavelength shorter than the ultraviolet range. For longer wavelengths, real-space digital holography is both a fast and reliable way to recover phase as it does not rely on phase retrieval algorithms, which can sometimes lead to errors in the reconstruction, and involve an extended computation time.

A conventional DHM measurement relies on combining the image of a sample obtained using a microscope with a reference wave at the same wavelength so that both interfere in the plane of a detector. These interferences encode both the amplitude and phase of the electrical field at the sample plane position, which can be recovered by applying straightforward numerical operations [79]. The measurement scheme we present in this paper relies on the same core principle. The main difference lies in the nature of the light emitted by the sample which is at a harmonic order of the fundamental light illuminating the sample.

Using non-linear light-matter interactions for developing new imaging techniques has received a lot of attention as the availability of suitable ultrafast laser sources has grown. Both second and third harmonic generation (SHG and THG) microscopy have found applications in a large variety of research fields such as biological imaging [80, 81], 2D surface inspection [82] and have been further developed to enable super-resolution microscopy below the diffraction limit [83]. A central advantage of non-linear microscopy resides in the possibility to generate light in localized areas of interest in a sample thus enhancing the contrast of an image and reducing the necessity to use chemical labels.

Non-linear holography is starting to draw some attention as well. Early work by Ye Pu and Hsieh C. in 2008 describes an experiment in which SHG emitted by a collection of nanoscatterers is used to form an hologram, allowing to trace back the 3D positions of the particles [84, 85]. Similar results were achieved by Schaffer et al. which also focused on the measurements of biological samples. More recent work by Farah et al. [86] focused on synthetic spatial aperture THG hologram reconstructions, emphasizing aberration removal using algorithms. Higher-order harmonics were also investigated to perform coherent-diffraction imaging [87, 88].

The principle of holography can also be applied to shape the light wavefront in a desired way by making a light source interact with a well-defined nanostructure. Patterned samples used for that purpose are often referred to as metasurfaces and have a wide variety of applications [89]. Significant efforts have recently been put in designing resonant metasurfaces allowing to control high-harmonic generation (HHG) emission, wherever it is to increase conversion efficiency [82], shape the emitted wavefront [90], or control

polarization of the harmonic light [91].

With this paper, we pioneer nonlinear DHM on solid nanostructures and demonstrate two applications: firstly, we show how holograms can be measured through transmission of thick and opaque materials with an enhanced resolution; Secondly, we show how nonlinear DHM can be used to characterize periodic subwavelength structures.

4.2 METHODS

4.2.1 ANALYTICAL FRAMEWORK FOR TRANSMISSION THG

In perturbative non-linear optics, the polarization at the third harmonic frequency 3ω induced by an external field oscillating at ω is given by [29]:

$$\tilde{P}_{3\omega}(z,t) = \epsilon_0 \chi^{(3)} \tilde{E}^3_\omega(z,t) \tag{4.1}$$

where ϵ_0 is the free space permittivity and $\chi^{(3)}$ is the third-order non-linear susceptibility of the material. For the excitation field, we consider a plane wave propagating along the z axis. Leaving the temporal dependence aside, we can write:

$$E_\omega(z) = E_0(z) e^{i(k_\omega z + \phi_\omega))} \tag{4.2}$$

with E_0 the absolute value of the field, and k_ω its wave vector. Substituting this expression in equation 4.1, we get:

$$P_{3\omega}(z) = \epsilon_0 \chi^{(3)} E_0 e^{i(3k_\omega z + 3\phi_\omega)} \tag{4.3}$$

We are interested in the third harmonic emitted through transmission of a silicon sample of width L. At the backside exit of the material, it can be expressed as the sum of contributions emitted from each slab along z:

$$E_{3\omega}(z) \propto \int_0^L P_{3\omega}(z) e^{i k_{3\omega}(L-z)} e^{-\alpha(L-z)} dz \tag{4.4}$$

where the first exponential term accounts for propagation of the third harmonic after generation, and the second one for losses in the material, with α being the absorption coefficient for the third harmonic. Substituting $P_{3\omega}(z)$ by its expression in equation 4.3, we get:

$$\begin{aligned} E_{3\omega}(z=L) &= \int_0^L \epsilon_0 \chi^{(3)} E_0^3 e^{i3(k_\omega z + \phi_\omega)} e^{i k_{3\omega}(L-z)} e^{-\alpha(L-z)} dz \\ &= \epsilon_0 \chi^{(3)} E_0^3 e^{i(k_{3\omega} L + 3\phi_\omega)} \int_0^L e^{i\Delta k z} e^{-\alpha(L-z)} dz \end{aligned} \tag{4.5}$$

where we recognize the phase matching term Δk:

$$\Delta k = 3k_\omega - k_{3\omega} \tag{4.6}$$

Solving the integral, we obtain:

$$E_{3\omega}(z=L) = \epsilon_0 \chi^{(3)} E_0^3 e^{i(k_{3\omega} L + 3\phi_\omega)} \frac{1 - e^{-(\alpha - i\Delta k)L}}{\alpha + i\Delta k} \tag{4.7}$$

This is the general expression for THG emitted in transmission of a material through excitation by a plane wave that will be used to evaluate experimental results.

4.2.2 EXPERIMENTAL SETUP

The light source we use to generate harmonics is a Ti:sapphire laser (up to 7 mJ, 35 fs, 1 kHz) pumping an optical parametric amplifier (OPA) with 5 mJ of its total output (*TOPAS* from *Light Conversion*) allowing us to tune the central wavelength of the beam in the near-infra-red (NIR). All measurements presented in this paper were performed using a fundamental wavelength of 2090 nm with 80 fs pulse duration, and the third harmonic order, centered at 694 nm, was recorded.

The OPA output is split into two arms: one is used to generate and image harmonic light emitted in transmission from a patterned silicon sample, while the other one is used to produce a reference plane-wave from a BBO crystal. Both arms are recombined on a CMOS detector using a 50/50 fused silica beam splitter. Figure 4.1 provides a schematic of the complete experimental setup.

The laser is focused onto the sample to a spot size of around 200 µm using a 20 cm focal length CaF_2 lens. This corresponds to a fluence on the order of 20 mJ/cm^2 and a peak intensity of 3.5×10^{11}W/cm^2. This value was chosen in order to maximize third harmonic emission while staying well below the damage threshold of the material, which we estimated to be close to 100 mJ/cm^2 or 1.3×10^{12}W/cm^2 for the given experimental parameters, where damage here refers to any measurable change in the optical signals after an extended period of exposure. No active stabilization system was needed as the interferometer displayed a sufficient fringe stability for the time of an hologram recording. Collection of the light was done using a Nikon plan fluorite objective with 0.5 NA, 20X magnification. Fundamental light was removed by inserting an interferometric band-pass filter upon recombination of the two arms.

4.2.3 SAMPLE DESIGN

The sample we used is a crystalline silicon resolution test target provided by ASML. Etching was performed with ebeam lithography, and all patterns were etched at the same depth of 75 nm (see profilometer measurement presented in Fig. 4.2). The total thickness of the sample is 700 µm, making it almost completely transparent to the 2090 nm fundamental, and partially transparent to the third harmonic, centered at a wavelength of 694 nm. As detailed in the papers from Yamada et al. [92] and Journigan et al. [93] , harmonic generation over such a long propagation distance inside silicon is not optimal for conversion efficiency, with effects of non-linear propagation of the fundamental decreasing the coherent emission of harmonics. Nevertheless, we could obtain high enough yields to allow for hologram recording in relatively short acquisition times (typically one second).

4.2.4 HOLOGRAM AMPLITUDE AND PHASE RECONSTRUCTION PROCEDURE

The numerical procedure used to extract phase and amplitude for harmonic DHM reconstructions from the hologram is essentially the same as for linear DHM (see Fig. 4.3). The complex-valued electric field in the plane of the detector can be expressed as follows:

$$E(x,y) = P(x,y) + R(x,y) \tag{4.8}$$

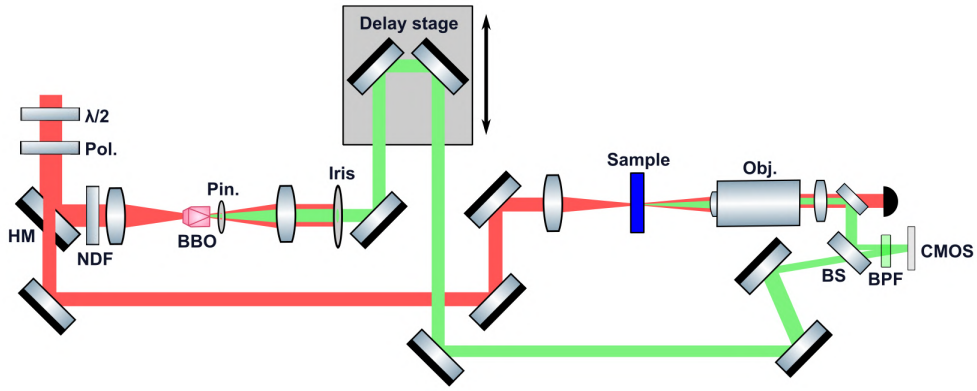


Figure 4.1: The OPA output goes through both a half-waveplate ($\lambda/2$) and a thin film polarizer (Pol.) in order to adjust power and polarization. A holey mirror (HM) is used to split the beam in two. The reflected beam, shaped as a donut in the far field, passes through an neutral density filter (NDF) in order to tune its relative intensity with respect to the other arm. It is focused in a BBO where harmonic generation takes place. A 200 µm diameter pinhole (Pin.) is placed just after the BBO in order to clean up the beam profile in the far-field. The donut-shaped NIR fundamental is filtered out using a partially closed iris while letting the third harmonic pass. The beam passes through a delay stage to adjust the time overlap of the two arms. Finally, the beam is sent to the detector by being transmitted through a beamsplitter (BS). The second beam path transmitted from the holey mirror is focused on the sample, and the scattered light is collected by an objective coupled to a tube lens. It is finally reflected from the beamsplitter and reaches the CMOS detector. A bandpass filter (BPF) is placed in-between the beamsplitter and the detector in order to filter out the fundamental.

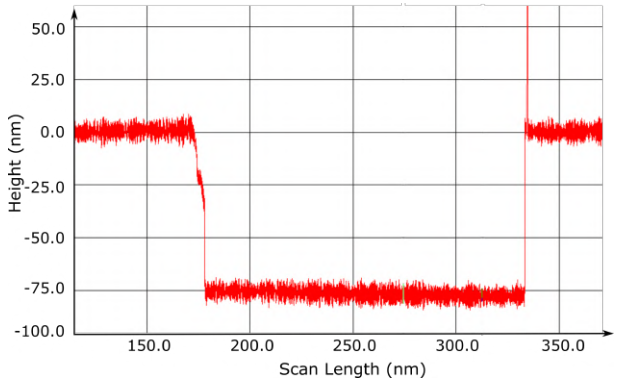


Figure 4.2: Profilometer measurement of a feature etched in the silicon sample from which the 75 nm height was extracted.

with $P(x,y)$ being the THG field emitted from the sample and $R(x,y)$ the reference plane wave emitted from the BBO, which can be expressed as $R(x,y) = |R|\, e^{i(k_x x + k_y y)}$. The hologram recorded by the CMOS detector (see Fig. 4.3a) is proportional to the intensity of this field:

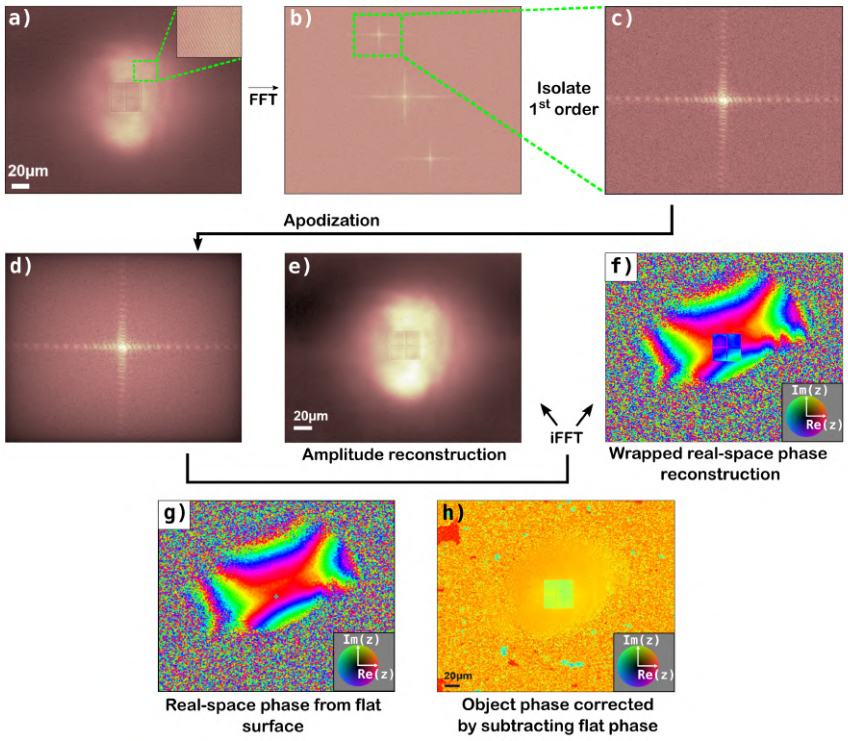


Figure 4.3: (a) Hologram displaying interference fringes between sample and reference wave as shown in the inset. (b) Fourier transform of (a) displaying characteristic DHM convolution terms marked by the green box. (c) Cropped DHM convolution term, highlighted from (b). (d) Blackman window apodization of (c). (e) Absolute value of the inverse Fourier transform of (d). (f) Complex phase of the inverse Fourier transform of (d). (g) Phase reconstruction of a flat area on the sample. (h) Subtraction of (g) from (f).

$$\begin{aligned} |E(x,y)|^2 &= |P(x,y)+R(x,y)|^2 \\ &= |P(x,y)|^2 + |R(x,y)|^2 + P^*(x,y)R(x,y) + P(x,y)R^*(x,y) \end{aligned} \tag{4.9}$$

Taking the Fourier transform of this expression yields (Fig. 4.3b)[79, 94]:

$$\begin{aligned} F^{-1}[|E(x,y)|^2] = \hat{P}(f_x,f_y) * \hat{P}^*(-f_x,-f_y) + |R|^2\delta(f_x,f_y) \\ + |R|\hat{P}(f_x+k_x,f_y+k_y) + |R|\hat{P}^*(-f_x+k_x,-f_y+k_y)) \end{aligned} \tag{4.10}$$

Where hats denote a Fourier transform, and f_x and f_y are the frequency space coordinates. The first two terms of this expression correspond to the autocorrelation of both the reference and sample waves Fourier transforms, centered on the origin of the frequency axis. The third term is the Fourier transform of the sample wave convolved by the Fourier transform of the plane wave reference (which translates to a delta function in frequency space). This convolution allows to shift the diffraction pattern from the origin

and to isolate it from the other terms. The fourth term is the complex-conjugate of the third term, centro-symmetrically inverted with respect to the origin.

The distance of these last two terms from the k-space origin depends on the hologram fringes spatial frequency, thus on both the wavelength as well as the relative incidence angle between sample and reference waves on the camera. If this frequency is too high the convolution is shifted out of the limits of the accessible frequency window. If the fringes frequency is too low, there is a risk the pattern overlaps with the terms sitting close to the origin, thus preventing an accurate reconstruction.

By isolating one of these twin patterns (Fig. 4.3c) and taking its inverse Fourier transform, both the amplitude and phase of the THG field can be obtained:

$$F^{-1}[|R|\hat{P}(f_x, f_y)] = |R||P(x, y)|e^{i\phi(x,y)} \tag{4.11}$$

A Blackman apodization filter on top of the isolated pattern in order to remove artifacts arising from cropping abruptly in Fourier space (Fig. 4.3d)[95, 96], after which the inverse Fourier transform in Eq. 4.11 is applied to reconstruct amplitude (Fig. 4.3e) and phase (Fig. 4.3f) of the object. As clearly visible in the wrapped phase reconstruction in Fig. 4.3f, the wavefront of the beam illuminating the sample is not flat and gets in the way of obtaining an accurate phase profile. Generally speaking, any deviation from the ideal case of using perfect plane waves for both the sample and reference waves alters the content of the phase and amplitude recovered in equation 4.11. Such aberrations can be corrected for by measuring an hologram on a flat part of the sample near the pattern of interest (Fig. 4.3g), and use its phase and amplitude reconstructions as references. Finally, a 2D unwrapping algorithm [97] is used to obtain a continuous phase profile (Fig. 4.3h).

4.3 RESULTS AND DISCUSSION

The spatial resolution of the phase reconstructions was determined using the one-image Fourier ring correlation (FRC) method [98]. Figure 4.4a-d shows phase reconstruction of multiple patterns etched on the silicon sample, and Fig. 4.4e, their corresponding FRC calculation. The patterns are an array of holes (Fig. 4.4a), a random distribution of particles (Fig. 4.4b), and a resolution target (Fig. 4.4c). According to the 1/7 cut-off frequency criteria [73], a resolution of 1.92 µm was extracted (Fig. 4.4d), which is less resolution than what should be achievable at an emission wavelength of 694 nm with a NA of 0.5. We attribute this result to cropping of the convolution term in Fourier space, which limits the achievable resolution in the final reconstruction.

We now delve deeper into analyzing the reconstructed phases. Figure 4.5 displays the results obtained in the measurement of a pattern composed of multiple holes (Fig. 4.5a). A phase reconstruction (Fig. 4.5b) is obtained from the hologram, the flat phase profile is subtracted from it, and the unwrapping algorithm is applied (Fig. 4.5c). The goal of this measurement is to verify how the phase difference obtained from the hologram relates to the height difference of 75 nm, and how it might differ from a linear DHM measurement. The phase line profile in Fig. 4.5d shows that the value is almost constant for both tops and bottoms of the holes. The average phase difference between the etched and pristine parts is 1.82 radians.

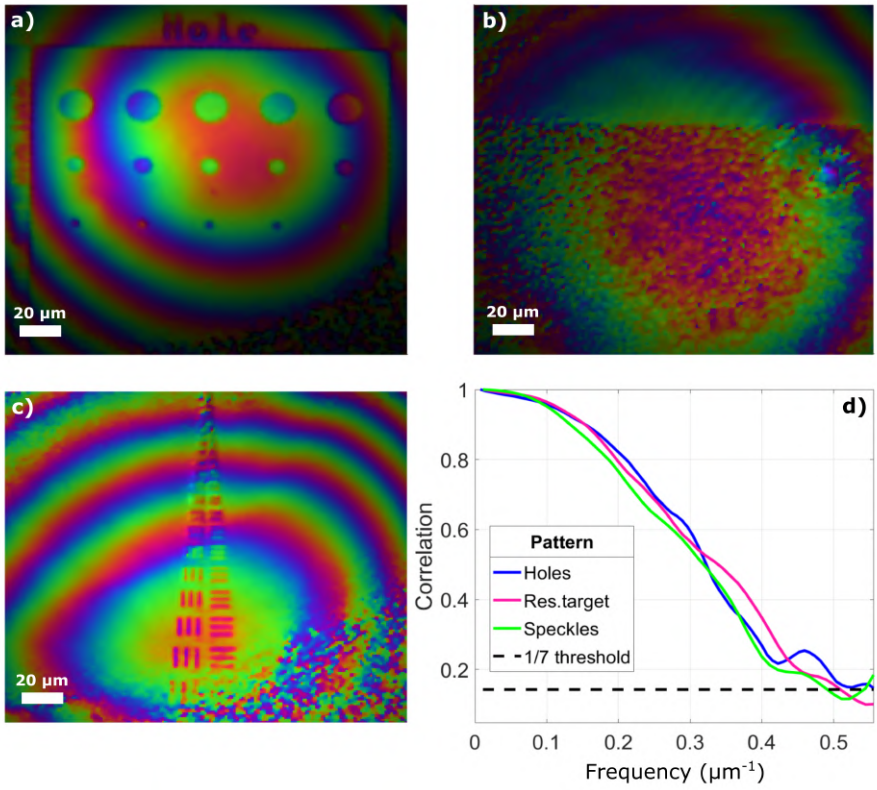


Figure 4.4: (a) Phase reconstruction of pattern made of holes. (b) Phase reconstruction of a random particle distribution. (c) Phase reconstruction of a resolution target. (d) FRC calculations using phase reconstructions a,b, and c.

To easily understand this result, we can separate the THG field in two contributions: a *bulk* part, which is common to both etched and unetched areas of the sample, and a *extra* contribution due to the additional layer of the unetched areas:

$$E_{3\omega}^{tot} = E_{3\omega}^{bulk} + E_{3\omega}^{extra} \tag{4.12}$$

although these fields can be derived exactly using equation 4.5, the absorption length of silicon at 690 nm is around 4.25 µm, which means the bulk contribution is much larger than the TH contribution from the extra layer of 75 nm. If we assume the phase and amplitude profile of THG is the same for etched and unetched areas at the interface with the nanostructure, we can therefore simplify the problem to the case of a plane wave propagating in two different media. In other words, the pattern essentially acts as a phase plate, altering propagation of the third harmonic already generated in the bulk. The formula for determining the phase offset between two waves propagating in different media is given by [87, 99]:

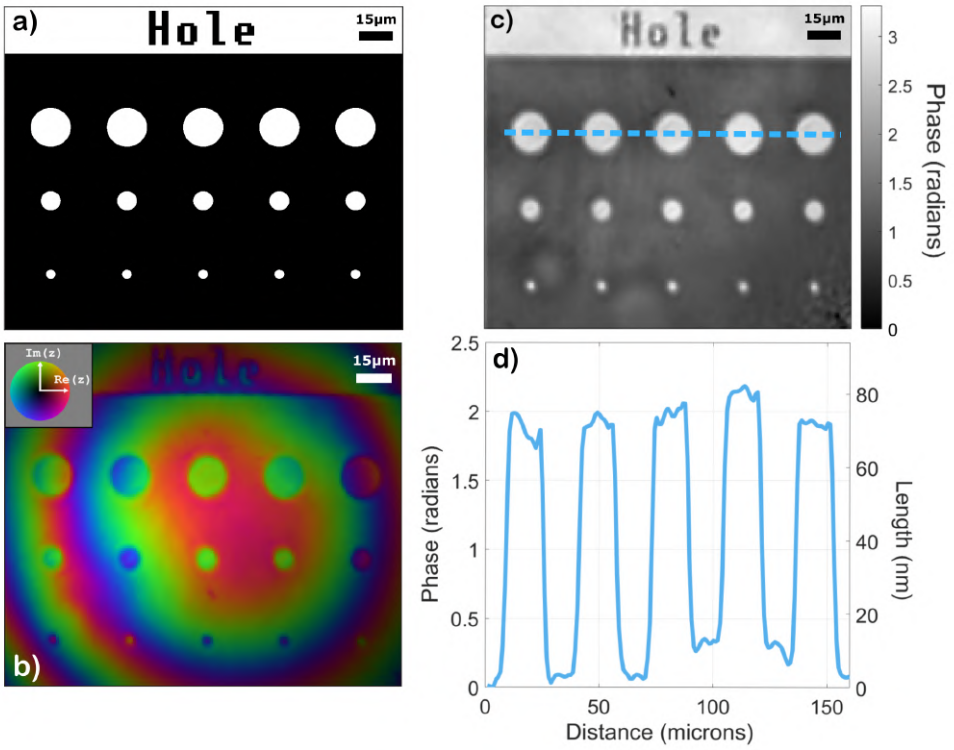


Figure 4.5: (a) Printing pattern for an array of 75 nm deep holes. The first line holes have a diameter of 16 µm, the second a diameter of 8 µm, and the third a diameter of 4 µm. (b) Reconstruction before subtraction of the reference flat phase. Color encodes phase and brightness encodes intensity. (c) Unwrapped phase reconstruction with subtraction of the flat phase. (d) Phase profile of the dotted blue line in figure (c).

$$\Delta\phi = \frac{2\pi}{\lambda}\Delta n(\lambda)L \tag{4.13}$$

where λ is the wavelength of the third harmonic, $\Delta n(\lambda)$ is the difference in refractive index between air and silicon, and L is the depth of the holes.

By averaging the phase difference obtained from multiple holograms, a depth L of 71.9 nm is extracted using equation 4.13, and 71.5 nm using the general formula given in equation 5.1 which is in very good agreement with the profilometer measurement. This result confirms that Eq. 4.13 holds for harmonic emission from diffracting structures, under the condition that the emission is governed by contribution from the bulk, and not from the nanostructures themselves.

We now turn to the cases where the simple expression used above does not work anymore, and focus on sub-wavelength features. The first set of sub-wavelength patterns we measured is composed of multiple gratings all having an equal pitch of 600 nm (Fig. 4.6a), with a fill factor (defined as the width of the lines over the periodic length of the grating) ranging from 50 to 90%. The reason we chose a slightly sub-wavelength pitch

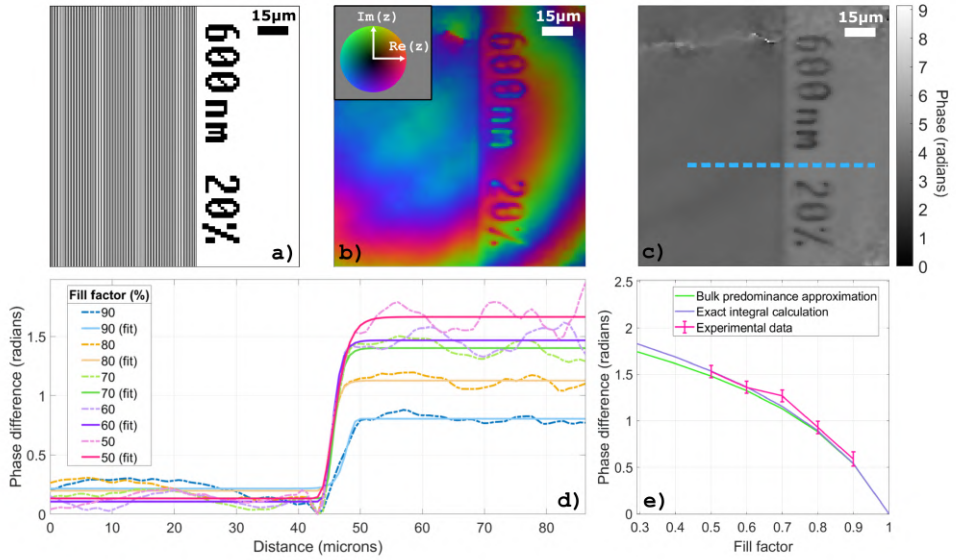


Figure 4.6: (a) Printing pattern for a sub-wavelength grating of 600 nm. (b) Reconstruction before subtraction of the reference flat phase. Color encodes phase and brightness encodes intensity. (c) Unwrapped phase reconstruction with subtraction of the flat phase. (d) Phase profile of the dotted blue line in figure (c) for different fill ratios. Curves are fitted to a sigmoid function to extract a phase difference between flat and sub-wavelength areas. (e) Phase differences as function of fill factor.

compared to our emission wavelength (694 nm) was to test approaches such as the effective medium theory, which usually work well for deep sub-wavelength features and have been successfully applied to e.g. describing deep sub-wavelength metasurfaces [100]. As can be seen in Fig. 4.6b, the lines of the sub-wavelength gratings are not resolvable in the reconstruction and an homogeneous phase distribution is measured over the entire extent of the nanostructure after flat phase subtraction (Fig. 4.6c), but a clear edge from the grating is visible. The phase between flat and nanostructured parts of the sample are fitted to a sigmoid function (Fig. 4.6d) so that a phase difference can be extracted for all fill factors (Fig. 4.6e). We can observe that the phase difference seems to scale exponentially with the inverse of the fill factor. We find that this result can still be explained (even though the features are relatively close-in-size to the wavelength) using an effective medium approach: by attributing a fill factor-dependent effective refractive index to the nanostructure, we can model how the recovered phase behaves. If light is polarized perpendicularly to the grating lines, effective medium theory gives an approximate expression for the complex-valued refractive index [100]:

$$n_{eff}^{TM} = \epsilon_a \left[\frac{\epsilon_a + \frac{1+2FF}{3}(\epsilon_b - \epsilon_a)}{\epsilon_a + \frac{1-FF}{3}(\epsilon_b - \epsilon_a)} \right]^{1/2} \tag{4.14}$$

with ϵ_a and ϵ_b being the refractive indices of both air and silicon at the third harmonic wavelength (1 for air and 3.80 for silicon), and FF being the fill factor. The effective

refractive index is included in both the general formula for transmission THG (equation 5.1), and the bulk predominance approximation (equation 4.13), in order to calculate the expected phase difference as function of the fill ratio. Fig. 4.6e shows that both models are in a very good agreement with the experimental data, confirming that an effective medium approach can be used to extract information on the critical dimension of subwavelength gratings using harmonic holography.

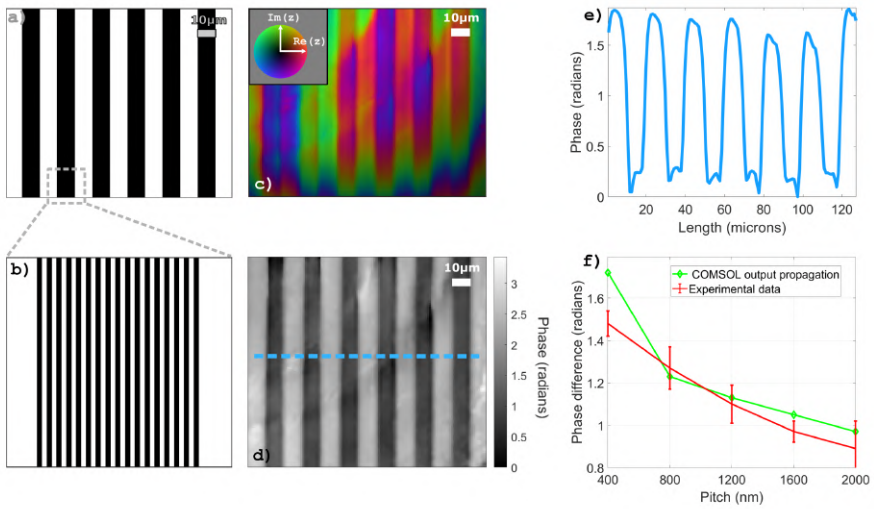


Figure 4.7: a) Printing pattern of a sub-segmented large pitch grating of 10 µm. b) Close-up on the sub-wavelength inner lines, here for a pitch of 600 nm. c) Reconstruction before subtraction of the reference flat phase. Color encodes phase and brightness encodes intensity. d) Unwrapped phase reconstruction with subtraction of the flat phase. e) Phase profile of the dotted blue line in figure d). f) Average phase difference between sub-wavelength gratings and flat areas for different pitch values.

The second set of nanostructures we focused on is a group of large pitch gratings (20 µm) (Fig. 4.7a) sub-segmented into smaller pitch lines (Fig. 4.7b). This design makes it easy to compare the phase from flat parts with the one of sub-wavelength gratings on a large area of the sample. Inner lines have a constant fill factor of 50% for all gratings of the set, and pitches ranging from 400 to 2000 nm. The depth of the etched lines is once again 75 nm. As can be seen in the wrapped (Fig. 4.7c) and unwrapped (Fig. 4.7d) phase reconstructions, the 10 µm pitch lines are easily distinguishable, whereas the inner lines are not. This is the case for all pitches of the set, which makes all of them "sub-wavelength" in the sense of being out of reach of the resolution imposed by our diffraction-limited optical system. Phase profiles are extracted, and the average phase difference is calculated. The plot in Fig. 4.7f shows an apparent inversely proportional relationship between the pitch and the phase difference measured between the structured and flat areas. The effective medium approach cannot account for such results, as only the fill factor should matter, i.e. the effective medium theory would not predict a change in phase as function of pitch for a constant fill factor.

In order to understand this result, calculations were performed using the electro-

magnetic waves package of the COMSOL software, which relies on the finite-difference method to solve Maxwell equations [101]. Our goal was to obtain the third harmonic wavefront emitted from the sample from the fundamental field distribution, propagate it to the far-field, and numerically simulate the measurement in order to compare it with our experimental results, following the approaches in [87, 102] where the same framework was applied to describe harmonic generation from solids.

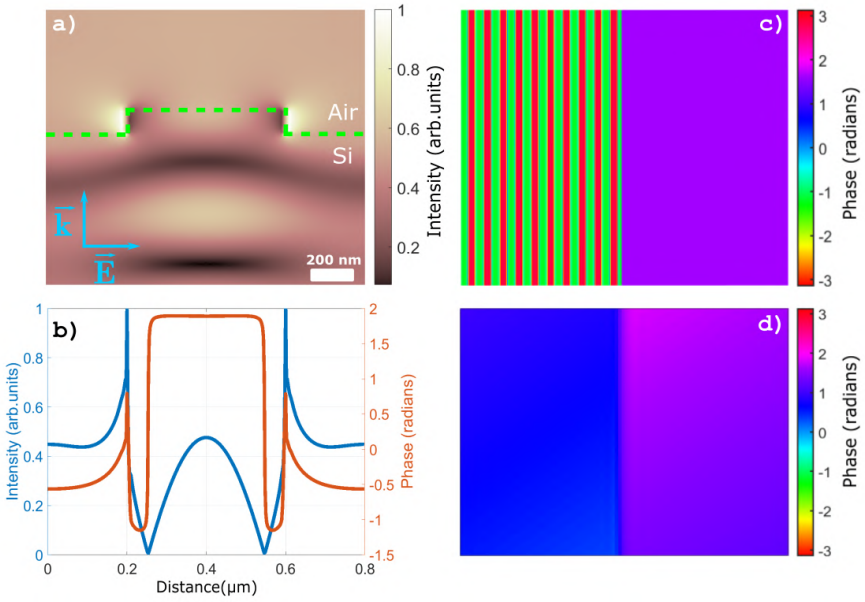


Figure 4.8: (a) Near-field intensity distribution in a single-line unit-cell of 800 μm pitch, obtained using the COMSOL software. The input field is a plane wave at the fundamental frequency propagating from the bottom to the top of the plot. (b) Near-field third harmonic phase and amplitude profile calculated by applying Eq. 4.15 to the field distribution in (a). (c) Simulated 2D phase distribution of the grating using the unit-cell calculations, juxtaposed to a flat area with no structures. (d) DHM phase reconstruction of (c). Details described in text.

Due to the symmetry invariance of the problem, the near-field distribution of a single unit cell, consisting of a 2D cross section in the plane orthogonal to the lines, is enough to establish the distribution of the field in the whole grating (Fig. 4.8a). The input field was simplified to a plane wave at the NIR pulse central wavelength, propagating from the bottom to the top of the unit cell. To obtain the emitted third harmonic, we use the following equation, which accounts for the inhomogeneous distribution of the fundamental:

$$E_{3\omega}(x, z = L) \propto \int_0^L |E_0(x, z)|^3 e^{ik_{3\omega}(L-z)} e^{-\alpha(L-z)} dz \tag{4.15}$$

where L is the coordinate of the silicon-air interface along the wave propagation axis, and 0 is the coordinate from which the THG contribution is summed-up in the silicon bulk. As can be seen in Fig. 4.8b, both phase and amplitude profiles of the third

harmonic wavefront are strongly distorted by the inhomogeneous distribution of the fundamental field. This approach can seem in contradiction the approximation made earlier in which the TH field generated in the nanostructure was neglected. However, near-field computations confirmed that coupling of the ω field to the subwavelength structures creates some significant change to the intensity distribution on a scale much larger than the etching height (see Fig.4.8a.), therefore explaining why this approximation no longer holds true.

To simulate the DHM measurement, several of these 1D phase and amplitude profile are merged to create a grating, and then extended in 2D (Fig. 4.8c). A frequency cut-off, corresponding to the NA of the imaging system which was used in the experiment, is applied in Fourier space to replicate the image recorded by the camera, thus making the lines invisible. A plane wave is overlapped on top to form an hologram, and the procedure presented earlier for phase and amplitude reconstruction is applied (Fig. 4.8d). Finally, the phase difference between the flat and nanostructured areas of the sample is computed and compared to the values obtained experimentally, as can be seen on Fig. 4.7f, directly next to the experimental results. The two plots shows an excellent agreement, with a slight offset for the smaller pitch of 400 nm, which we assign to a lower SNR for this particular pitch measurement. This results confirms the validity of our approach at modeling the non-linear scattering from nanostructures and how it reflects in the DHM phase measurement. A practical application of this reconstruction method would be to perform such calculations for multiple values of a periodic structure characteristic features to create a library that would be fitted to the measured data. The recovered phase depends on both pitch, CD and etching depth of the lines. Thus, using this technique to measure these three parameters at once could lead into potential errors. Disentangling each contribution could be achieved by making measurements at different polarization, since the local-field enhancement of the fundamental shows very different behavior when polarized perpendicular or parallel to the lines.

From the power law dependence in equation 4.15, we can expect that higher harmonic orders should allow for a large improvement in sensitivity: any slight change to the fundamental distribution inside the material should translate to larger observable phase shifts, making this technique extremely promising, without being necessarily required to use smaller wavelengths, but instead high nonlinearities. These expectations can be mitigated by the fact that higher-order harmonics generated in the non-perturbative domain are expected to deviate from this power law scaling, but we can nevertheless assume some significant resolution enhancement can be achieved.

4.4 CONCLUSION

Our results show that harmonic DHM allows to recover phase information in a reliable manner, and accurate height profiles with a very sharp contrast could be extracted from all measurements. The most notable aspect of this technique concerns the reconstruction of periodic subwavelength structures. We could show that measuring phase instead of amplitude allows for precise recovery of depth, but other key morphological parameters as well. Moreover, the technique makes use of the harmonic generation power scaling as a tool for improving sensitivity. These results thus provide a promising route and motivation towards applications in the measurement of metrology markers used in the

semiconductor industry.

Another important aspect of this chapter is that all the results were obtained by measuring through transmission of a 700 µm thick silicon sample. Thus, harmonic holography could be used for inspection of etched patterns on the back-side of opaque samples, which could not be possible otherwise. The reconstructions we obtained do not seem to be altered by propagation of the fundamental through the sample, such as self-focusing, which could be expected when dealing with such high intensities. Measurements in a reflection geometry can also be envisioned and are under consideration for upcoming experiments.

Further work will address reconstructions at higher harmonic orders, measuring smaller-sized patterns, as well as investigating other morphological parameters of gratings such as side-wall angle or surface roughness.

Moreover, we see a particular advantage of our nonlinear imaging approach for studying the emission phase of solid HHG following photoexcitation when used in a photoexcitation-pump / nonlinear-DHM-probe geometry, as our nonlinear DHM measurements provide a self-referenced measurement against the ground-state emission. Recent studies have indicated strong amplitude changes of solid HHG due to photoinduced insulator-to-metal phase transitions [13, 103], modification to the dielectric function [102, 104], and photocarrier-induced electron-hole dephasing [15, 68, 105, 106], but accompanying phase changes remain largely elusive. At the same time changes of energy levels by photocarrier excitation [106, 107] and driving-intensity controlled dipole phase contributions [47] have been shown to shift the phase of solid HHG. Understanding amplitude and phase changes following photoexcitation is relevant for unraveling fundamental ultrafast dynamics in solid materials, just like phase sensitive HHG spectroscopy advanced molecular dynamics [50]. Moreover, measuring phases of HHG from excited materials can help further improving super-resolution harmonic deactivation microscopy (HADES) [83, 105] and solid-state HHG source design [39].

5

NON-LINEAR FOURIER TRANSFORM HOLOGRAPHY

Holographic techniques applied to harmonics generated in solids have recently received a lot of interest. The additional information provided by probing the phase of harmonics can be used to enhance contrast in imaging, investigate ultrafast electron dynamics in new ways, but also to learn more about the fundamental properties of harmonic generation itself.

At higher harmonic orders belonging to the extreme ultraviolet, alternative methods are needed to circumvent the lack of adapted optics for imaging. In this paper, we are proposing to combine harmonic generation with Fourier holography which adopts a lensless approach, in order to solve this issue.

As a first proof of principle, we demonstrate that measurements of the far-field third harmonic emission from Fourier holography-like targets etched in silicon allow to recover both phase and amplitude of the harmonic field. Aberration-free imaging was achieved, with a lateral resolution of 1.5-2 µm, and height characterization of grooves etched by a few hundred nanometers could be extracted from phase reconstructions with an accuracy in the order of tens on nm. Results could also show evidence of laser-induced oxidation of the silicon, detectable from the phase distribution of the reconstructed holograms.

We anticipate our results to pave the way towards applications at higher harmonics orders, providing a new tool for harmonic wavefront characterization at shorter wavelength, which would be relevant for both semiconductor nanofabrication metrology, and solid high harmonic spectroscopy of transient dynamics in solids.

This chapter is based on: L. Guery et al.(2026), Phase imaging of nanostructures using third harmonic Fourier-transform holography. In preparation for submission.

5.1 INTRODUCTION

High harmonic generation (HHG) is an extreme non-linear interaction between a laser field and a solid, gas, or liquid medium, resulting in the emission of high order harmonic of the fundamental driving field due to the laser-induced sub-cycle electron dynamics taking place in the attosecond time scale [108]. In high-harmonic generation from solids (SHHG) can be mainly described by two distinct mechanisms: the non-linear motion of electrons inside the crystal due to interaction with the driving field (intraband contribution) and the recombination to its ground state (interband contribution)[7, 10, 11, 109, 110]. The intrinsic nature of this process makes SHHG spectroscopy a very effective probe of the material electronic structure, as the phase and intensity of emitted harmonics encode the electron motion though k-space, allowing to map out energy bands[8, 36]. Just like gas-phase HHG has been extensively used to study molecular processes and photochemistry [50, 111, 112], SHHG has been used very successfully as an ultrafast probe of transient photo-induced condensed-matter dynamics [13, 15, 103, 107].

Combining SHHG with holographic techniques enables to spatially resolve both the amplitude and phase of emitted harmonics, allowing to probe both the real and imaginary part of the refractive index, and in general, to obtain a more complete picture of nonlinear light-matter interactions in a material, bringing additional insight on ultrafast electron dynamics taking place in a material and on the harmonic generation process itself. Phase imaging is also a very valuable tool for enhancing contrast between materials, especially in an otherwise transparent medium.

First demonstrations of holography in the perturbative regime were performed using traditional in-line or off-axis holography [84–86, 113, 114] to track the 3D positions of nanoparticles. For higher harmonic orders in the extreme ultraviolet (XUV), a lensless approach needs to be considered because of the high absorbing nature of light in this energy domain, which precludes the use of optical elements such as lenses and objectives. Following the pioneering work by Sivis et al. that showed structured harmonic emission and imaging in the visible spectral range [115], the first work in structured XUV harmonic emission and imaging was demonstrated by Roscam Abbing et al.[87] in which far-field harmonic emission from a nanostructured silica sample could be measured and compared to theory. The following work by Korobenko et al. has shown that coherent diffractive imaging (CDI) could also be applied to SHHG [88] to spatially resolve the phase of XUV harmonics. In this paper, we are investigating another lensless imaging technique called Fourier-transform holography (FTH) which is typically used at XUV/X-rays wavelengths obtained from synchrotrons, free electron laser facilities and gas-HHG setups [25, 27, 116–119]. It has proven to be a very effective tool for imaging ultrafast magnetization dynamics [26, 120, 121] with unprecedented time and spatial resolution.

An alternative approach to FTH we propose in this work, is to directly generate harmonics from the sample using a near-infrared laser, and to map-out the phase and amplitude distribution of harmonics by measuring their far-field diffraction pattern. We demonstrate that by applying this principle to third harmonic generated from silicon structures, a phase-based reconstruction of heights can be achieved with an accuracy down to the tens of nanometer scale.

5.2 METHODS

5.2.1 RECONSTRUCTION METHODOLOGY

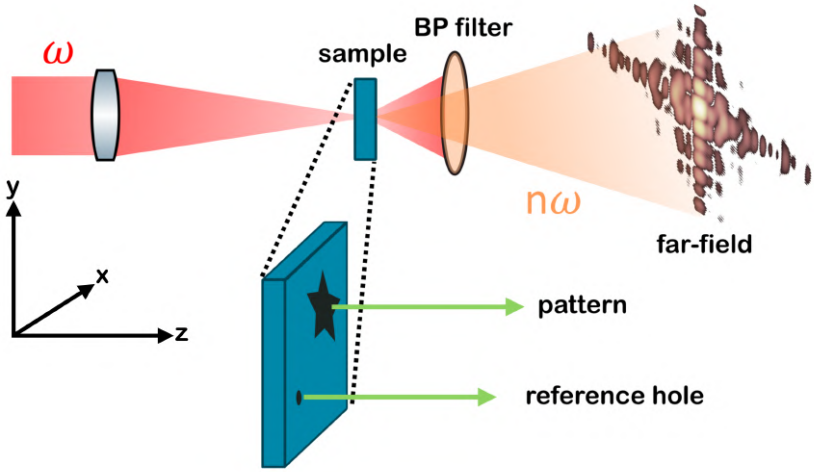


Figure 5.1: Principle of non-linear FTH. A light pulse at frequency ω propagating along the z-axis is focused orthogonally to the backside of the sample. On the frontside, which is composed of the pattern of interest, and a reference aperture etched some distance away, the sample emits harmonics of the fundamental driving field. A bandpass filter is used to measure the interference pattern of a single harmonic on the detector. The diffraction pattern is proportional to the Fourier transform of the near-field harmonic emission in the x-y plane, integrated over the width of the sample (z-axis).

The main difference between standard FTH relying on linear diffraction and the technique we are presenting in this chapter is that light emitted in the far-field is directly generated from the sample, and not simply transmitted (see Fig. 5.1). The third harmonic field can be computed by integrating harmonic emission over the width of the sample, using equation 4.5 introduced in the previous chapter:

$$\begin{aligned} E_{3\omega}(z=L) &= \int_0^L \epsilon_0 \chi^{(3)} E_0^3 e^{i3(k_\omega z+\phi_\omega)} e^{ik_{3\omega}(L-z)} e^{-\alpha(L-z)} dz \\ &= \epsilon_0 \chi^{(3)} E_0^3 e^{i(k_{3\omega}L+3\phi_\omega)} \int_0^L e^{i\Delta k z} e^{-\alpha(L-z)} dz \end{aligned} \tag{5.1}$$

where ϵ_0 is the free space permittivity, $|E_0|$ is the amplitude of the fundamental field, L is the position of the silicon-air interface along the wave propagation axis, χ^3 is the third-order non-linear susceptibility tensor, α is the absorption coefficient at the harmonic wavelength and $k_\omega / k_{3\omega}$ are respectively the wavevector of the fundamental and third harmonic inside silicon.

This equation is based on the assumption that we are still operating in the perturbative regime, with harmonic generation following the standard power law scaling of non-linear optics [29]. In order to extend this technique to higher harmonic orders, at intensity regimes beyond the perturbative regime, this equation would need to be adjusted to

account for the different power scaling of higher order harmonics as well as for their more complex dipole phase content.

5.2.2 SAMPLE FABRICATION

In this experiment, two samples are used, both composed of a 1 µm thick silicon nitride membrane sputter coated with a 200 nm gold layer on the backside and a 500 nm silicon layer on the front side, using plasma enhanced chemical vapor deposition. Patterns are etched in silicon via focused-ion beam lithography using a dual-column scanning electron microscope / focused-ion beam system. An aperture is etched in the backside covered with gold so that only a small area of interest in silicon gets to transmit the laser field. A reference hole of 2 micron diameter is etched in silicon at a distance slightly longer than two times the length of the pattern. This constraint on the position of the hole is necessary in order to avoid any overlaps between convolution terms, as mentioned in the theoretical framework of FTH. Finally, sample characterization was done by using SEM images acquired after patterning, and profilometer measurements for recovering a precise height profile.

5

5.2.3 EXPERIMENTAL SETUP, DATA ACQUISITION AND ANALYSIS

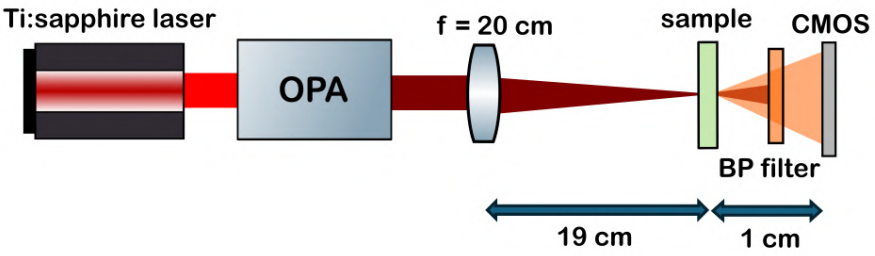


Figure 5.2: Experimental setup for the third harmonic FTH. The output of the Ti:sapphire laser is converted to NIR wavelength by the OPA. The idler is focused on the sample 1 cm before the focus position of a f = +20 cm lens. The fundamental is blocked using a bandpass filter, letting the third harmonic diffraction pattern to be recorded by a CMOS detector.

The light source is a Ti:sapphire laser (up to 7 mJ, 35 fs, 1 kHz) pumping an optical parametric amplifier (OPA) (TOPAS, Light Conversion) in order to generate wavelength in the near-infrared (NIR). The OPA output is focused on the sample to a spot size of around 400 µm, with an energy per pulse of a few µJ. This corresponds to a fluence of the order of tens of mJ/cm^2, and a peak intensity of the order of 10^{11}W/cm^2. This value was chosen to maximize third-harmonic emission while staying below the material damage threshold, but also to allow for illumination of both the sample and the reference hole. Focusing was made before the sample with a relatively long focal length lens of 20 cm to avoid intensity-dependent phase contributions such as dipole phase [46, 47] and Kerr effect non-linearities. When generating harmonics inside a solid sample, the total yield emitted in the far-field can be strongly influenced by the focusing position relative to the sample. Light emitted after focus is π phase-shifted compared to light emitted before focus. This

effect, called the Gouy phase shift [37], can strongly influence the total yield emitted in the far-field as both contributions can interfere destructively with each other, but also affect the phase reconstructions. With choosing to focus the beam before the sample, we avoid such issues.

The Fresnel number is a standard criteria to indicate if the far-field diffraction regime is achieved [19]:

$$F = \frac{a^2}{L\lambda} \tag{5.2}$$

Where a is the characteristic feature size of the pattern (around 1 µm), L is the distance from the sample to the detector and F the Fresnel number which needs to satisfy $F << 1$ in order to satisfy the far-field regime. Considering the sample dimensions, this criteria could be fulfilled by putting the CMOS detector at a distance close to 1 cm after the sample, which corresponds to a NA (numerical aperture) of around 0.5. A bandpass filter centered on the third harmonic wavelength was also positioned between the camera and the sample.

Because of the limited dynamic range of the camera, it is not possible to simultaneously record the very intense central part of the diffraction pattern, or order zero, and higher frequency terms, in a single image. In order to record the full pattern at once, multiple diffraction patterns are measured at the same position with different integration time, and stitched together using the Debevec algorithm [72] to produce a high dynamic range image. Aberration correction is performed by applying a Blackman apodization filter to the stitched diffraction pattern to remove artifacts arising from cropping abruptly in Fourier space [96]. Finally, an inverse Fourier transform is applied, allowing to extract both a phase and amplitude reconstruction.

5.3 RESULTS

A first test structure, shown schematically in Fig. 5.3, consists of three square recesses etched into the 500 nm-thick silicon layer, each with a different etch depth. This sample is designed to evaluate the sensitivity of third-harmonic Fourier transform holography (FTH) to nanoscale height variations in a realistic silicon platform and to test whether the reconstructed phase can be used for quantitative height metrology.

Figure 5.4 presents the FTH reconstruction of the third-harmonic field generated using a fundamental wavelength of 1.98 µm. In Fig.5.4a, the diffraction pattern obtained from HDR stitching of three measurements performed with integration times of 10, 100, and 1000 ms is shown. In Fig.5.4b, a blackman window is applied to the diffraction pattern for apodization, and zero-padding is performed, resulting in an image four times larger in both dimensions. The amplitude and phase reconstructions resulting from the inverse Fourier-transform are respectively displayed in Fig.5.4c and Fig.5.4d. The x–y axes correspond to spatial coordinates in the sample plane, while the color scale encodes the phase of the complex field. The three etched regions are clearly resolved, with distinct phase levels corresponding to different depths. The phase distribution outside the reconstructed structure displays a random phase value, which is expected since it corresponds to areas not illuminated by the laser, and thus lacking relevant intensity and phase content. A phase line profile extracted along the dashed line in Fig.

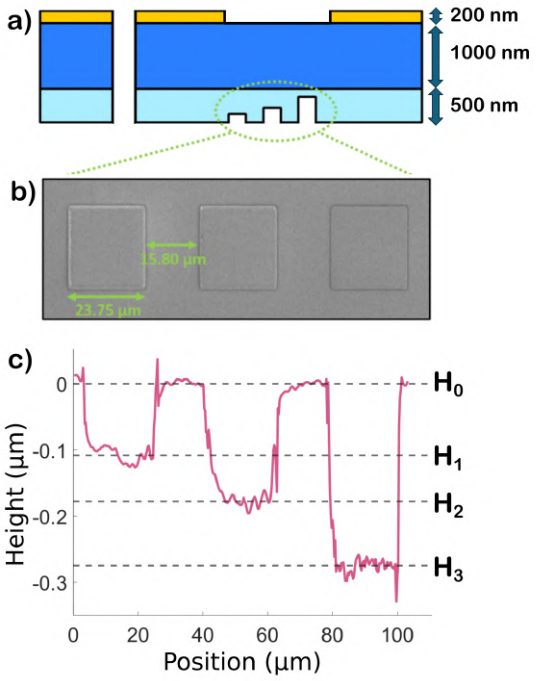


Figure 5.3: a) Schematic of the sample from a side-view, composed of three layers: a first opaque gold layer of 200 nm, a supporting SiN layer of 1 µm, and a 500 nm silicon layer in which the pattern and the reference hole are etched. An aperture is also etched in gold so that only the pattern gets illuminated. b) SEM image of the three square structures. c) Profilometer measurement going over the pattern. The mean depth values for each of the square patterns are H1 = 108 nm, H2 = 177 nm, and H3 = 276 nm.

5.4(e) is shown in Fig. 5.4(d), revealing discrete phase steps. Equivalent measurements performed with a 1.71 µm driving wavelength, generating a third harmonic at 570 nm, are displayed in Fig.5.5, where the pattern can again be resolved in both the amplitude and phase reconstruction.

According to equation 4.5, the third harmonic phase difference between the surface and a groove of height ΔL is:

$$\begin{aligned}\Delta\phi &= \phi_{\text{top}} - \phi_{\text{bot}} \\ &= arg\left(E_0^3 e^{i(k_{3\omega}L+3\phi_\omega)} \int_0^L e^{i\Delta kz} e^{-\alpha(L-z)} dz\right) \\ &- arg\left(E_0^3 e^{i(k_{3\omega}L+3\phi_\omega)} \int_0^{L-\Delta L} e^{i\Delta kz} e^{-\alpha(L-\Delta L-z)} dz\right) - arg\left(e^{ik_{3\omega}^{air}\Delta L}\right)\end{aligned} \tag{5.3}$$

In which the term $e^{ik_{3\omega}^{air}\Delta L}$ accounts for the propagation in air of the light emitted from the bottom of the groove, and where $k_{3\omega}^{air}$ is the third-harmonic wave vector in air. In our measurement, the third harmonic has a very long propagation distance compared

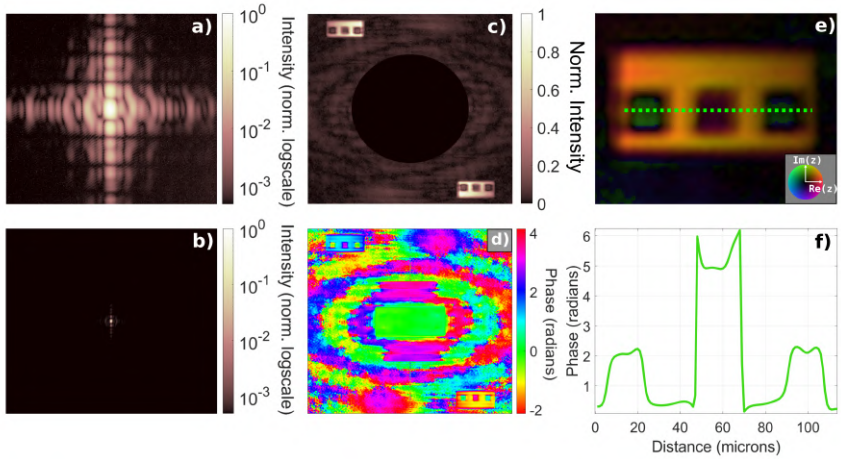


Figure 5.4: FTH reconstruction of the THG hologram for a fundamental wavelength of 1980 nm. a) Diffraction pattern formed by stitching three measurements made with an exposure time of 10, 100, and 1000 ms. b) A Blackman apodization window is applied to the diffraction pattern, which is then zero-padded so that the number of pixels along both axis becomes 4 times bigger. c) Amplitude reconstruction of the hologram. d) Phase reconstruction of the hologram. e) Close-up on the pattern reconstruction with colors representing the phase, and brightness representing intensity. f) Phase profile of the green dotted line plotted in e).

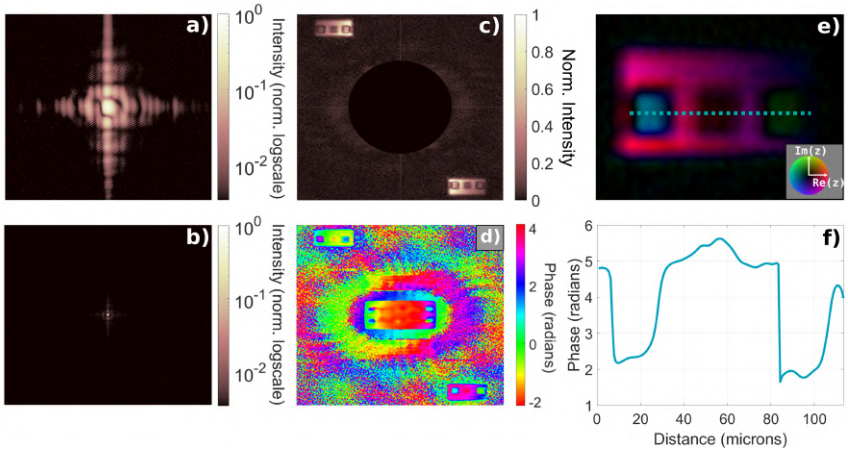


Figure 5.5: FTH reconstruction of the THG hologram for a fundamental wavelength of 1710 nm. a) Diffraction pattern formed by stitching three measurements made with an exposure time of 10, 100, and 1000 ms. b) A Blackman apodization window is applied to the diffraction pattern, which is then zero-padded so that the number of pixels along both axis becomes 4 times bigger. c) Amplitude reconstruction of the hologram. d) Phase reconstruction of the hologram. e) Close-up on the pattern reconstruction with colors representing the phase, and brightness representing intensity. f) Phase profile of the blue dotted line plotted in e).

to the height of the pattern etched on the surface (attenuation length of 1.44 µm at the third harmonic wavelength of 570 nm and 3.41 µm at 660 nm, compared to groove heights

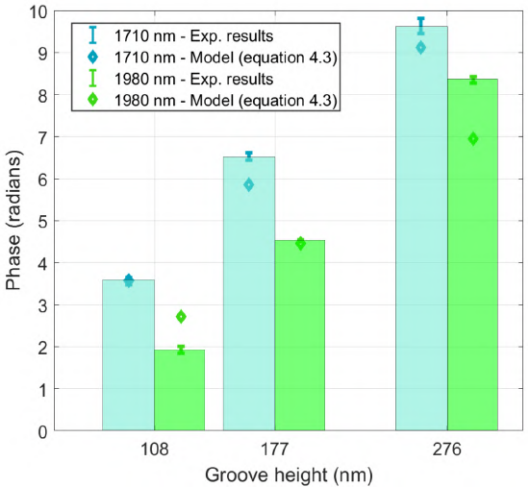


Figure 5.6: Phase difference between the etched and non etched part of the sample as a function of the groove height of the holes for both experimental results and calculations following equation 5.3.

between 108 and 276 nm). Figure 5.6 displays the phase difference recovered for the three groove heights compared to theory. The three data points suggest a linear relationship between phase and groove height, which is expected from the equation 5.3 in the limit of small groove heights with respect to the total length over which the third harmonic is generated. Small differences in the slope can be noticed compared to the calculations, in particular for the 1980 nm measurement, and are due to the uncertainty of the exact value of the refractive index, which imposes the coefficient of these slopes. These results confirm the validity of equation 5.3 in the interpretation of the phase recovered from third harmonic Fourier holograms.

We next quantify the spatial resolution of the phase reconstructions using the one-image Fourier ring correlation (FRC) method. The reconstructed phase image is divided into statistically independent subsets according to the procedure in ref. [98], and the FRC is computed as a function of spatial frequency. The intersection with the 1/7 threshold [73] yields resolutions of 2.02 µm and 1.63 µm for the third-harmonic wavelengths of 660 nm and 570 nm, respectively (Fig. 5.7). Considering the imaging system NA of ~ 0.5, the Abbe diffraction-limit relation would predict resolutions of around 0.57 µm and 0.66 µm, which is roughly 2.5 ~ 3 times smaller than the values extracted from the FRC calculations. These offsets could be explained by a variety of reasons, among which is the fact that the reference hole is not a true delta function, therefore reducing the achievable resolution. Processing of the raw data before reconstruction, such as the stitching of the multiple diffraction patterns or the application of an apodization filter in Fourier space, could also play a role in decreasing the resolution. We can, however, notice the resolution improvement at 570 nm compared to 660 nm, consistent with the expected wavelength scaling.

Beyond height metrology, we further investigate whether the reconstructed phase is

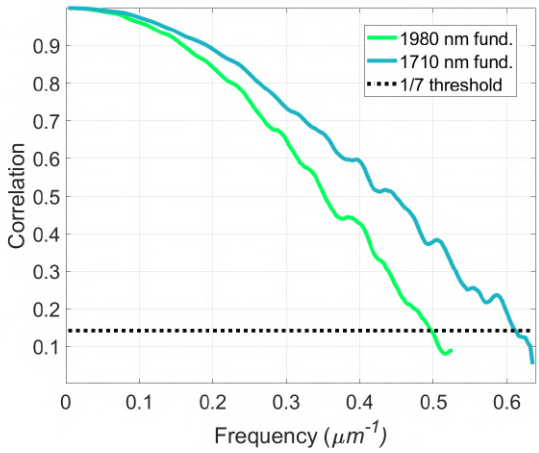


Figure 5.7: Fourier ring correlation of the phase reconstructions from the second sample. Crossover with the 1/7 threshold indicates a resolution of 1.63 μm for the third harmonic wavelength of 570 nm, and 2.02 μm for the one at 660 nm.

also sensitive to refractive-index variations at the sample surface due to varying chemical composition, using a second test structure. The spatially resolved hologram of the test structure interfering with a reference plane wave from an adjacent reference scatterer is shown in Fig. 5.8a. A SEM image of the test structure itself is shown in Fig. 5.8b. The structure is composed of 100 nm-deep lines etched into the silicon layer and a circular aperture is etched on the front-side gold layer of the sample. Figures 5.8(c–d) display the spatially resolved third-harmonic amplitude and phase reconstructions obtained using fundamental wavelengths of 1.71 µm and 1.98 µm. The lines can be resolved for both wavelengths. Some parts are not visible because the aperture etched in the gold layer is not exactly lined up with the pattern on the other side. The etched regions exhibit a uniform phase offset, as expected for constant etch depth. In contrast, the unetched silicon surface shows significant spatial phase variation. Applying equation 5.3, we can identify that areas in red in Fig. 5.8c and in yellow/orange in Fig. 5.8d display the expected phase difference ($\simeq \pi$) with respect to the grooves of 100 nm (see Fig. 5.6). We are making the hypothesis that areas with a different phase are affected by the formation of a passive oxidation layer on top of the silicon surface. Indeed, in ambient air, at room temperature, a thin oxidation layer of 1-2 nm forms on silicon within a few minutes. This layer then acts as a passive barrier which prevents further oxidation of the silicon underneath. However, considering the refractive index of both silicon (3.84 at 660 nm and 4.02 at 570 nm) and silicon dioxide (1.46 for both wavelengths) at the third harmonic wavelength, such a thin layer cannot explain the large phase difference of around π observable on unetched areas, which according to equation 5.3, should correspond to an oxide layer of around 270 nm. To understand the formation of such a large oxide layer, the laser-induced local heating of the sample needs to be accounted for, as temperature increase drastically enhances silicon dioxide formation. This effect is well documented in the literature [122]

and confirms the possible validity of our hypothesis. This demonstrates that non-linear holographic phase reconstructions are not only sensitive to geometric height but also to nanoscale refractive index variations.

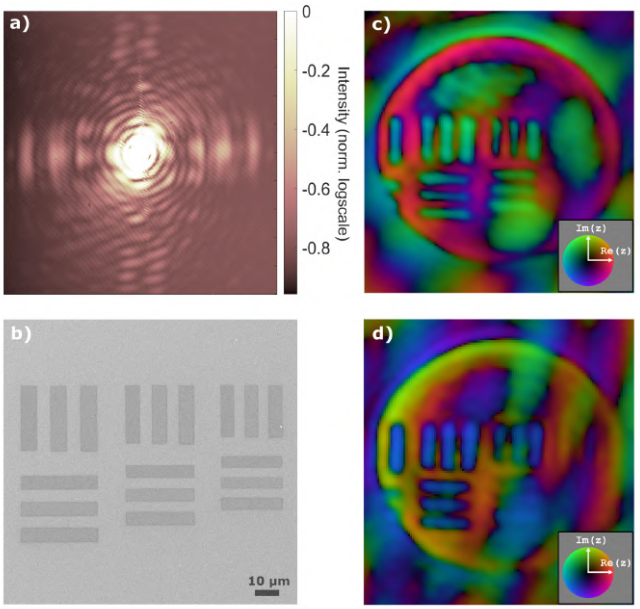


Figure 5.8: a) Diffraction pattern of third harmonic at a wavelength of 570 nm. b) SEM image of a pattern etched in silicon. c) Hologram reconstruction with a third harmonic of 570 nm. Colors correspond to the phase and brightness to the intensity. d) Hologram reconstruction with a third harmonic of 660 nm.

5.4 CONCLUSION

The results presented here demonstrate that Fourier transform holography using third-harmonic generation from silicon nanostructures enables quantitative, lensless phase imaging with nanometer-scale height sensitivity. By fabricating test structures with well-defined etch depths, we showed that the reconstructed phase increases linearly with feature height and agrees with a simple propagation model under clearly defined approximations. This confirms that third-harmonic emission from solids can be used as a reliable metrological signal without being obscured by nonlinear dipole-phase effects, provided that a loose focusing geometry is used. The spatial resolution, quantitatively assessed using Fourier ring correlation, is determined by the harmonic wavelength and detector numerical aperture, reaching the micrometer scale in our configuration. In addition, surface-sensitive phase variations observed on unetched regions demonstrate sensitivity to nanoscale refractive index changes, enabling differentiation between silicon and native oxide layers.

While the current implementation is limited by the third-harmonic wavelength, detector dynamic range, and the use of static samples, these constraints do not reflect fundamental limitations of the method but rather the experimental configuration. Improvements in detector geometry and extension to higher-order harmonics are expected to yield sub-wavelength spatial resolution. Additionally, the field of view is at present restricted by the size of the etched aperture and reference-hole separation, which can be optimized to access larger areas or denser photonic structures.

Taken together, these results establish third-harmonic Fourier holography as a viable table-top approach for quantitative metrology in silicon-based platforms, capable of retrieving both structural and material information without imaging optics. The demonstrated robustness against nonlinear phase distortions and the agreement with a simple propagation model lay a foundation for extending this technique to higher harmonic orders, shorter wavelengths, and time-resolved pump–probe measurements. These developments will enable all-optical, lensless phase imaging of ultrafast electronic and structural dynamics in solids, and provide a compact and scalable metrology tool for semiconductor nanofabrication and materials science.

6

FOLLOWING THE NONTHERMAL PHASE TRANSITION IN NIOBIUM DIOXIDE BY TIME-RESOLVED HARMONIC SPECTROSCOPY

Photo-induced phase transitions in correlated materials promise diverse applications from ultrafast switches to optoelectronics. Time-resolved metrology of those transitions and possible metastable phases are key enablers for these applications, but challenge existing experimental approaches. Extreme nonlinear optics can help probe phase changes, as higher-order nonlinearities have higher sensitivity and temporal resolution to band structure and lattice deformations. Here the ultrafast transition from the semiconducting to the metallic phases in polycrystalline thin-film NbO2 is investigated by time-resolved harmonic spectroscopy. The emission strength of all harmonic orders shows a steplike suppression when the excitation fluence exceeds a threshold (~11-12 mJ/cm^2), below the fluence required for the thermal transition - a signature of the non-thermal emergence of a metallic phase within 100±20 fs. This observation is backed by full ab-initio simulations as well as a 1D chain model of high-harmonic generation from both phases. Our results demonstrate femtosecond harmonic probing of phase transitions and non-thermal dynamics in solids.

This chapter is based on: Z. Nie and L. Guery et al.(2026), Following the nonthermal phase transition in niobium dioxide by time-resolved harmonic spectroscopy. *Physical review letters*, 131(24), 243201.

6.1 INTRODUCTION

Optical control of exotic or hidden phases in strongly correlated systems has emerged as one of the core topics in condensed matter physics [123, 124]. Besides a fundamental interest in disentangling competing electron-electron and electron-lattice interactions, there is an equally attractive technological relevance for the realization of Mott memristors [125–127]. Particularly, photo-induced insulator-to-metal transition (IMT) in strongly correlated materials has been studied widely for decades [56, 61, 125, 126, 128, 129]. Various ultrafast spectroscopy tools such as linear reflection/absorption [61], photoelectron emission [128], and X-ray or electron diffraction[129] were applied to reveal lattice distortions and bandstructure transformations, and even indications for metastable or hidden states were discovered in photo-induced IMT [128, 129]. The substantial achievements made in this area are mostly based on linear or low-order nonlinear spectroscopy, which probes a perturbative response of the bound electronic states.

High harmonic generation (HHG) is an extreme nonlinear optical effect and has been widely studied in gases for decades and in more recent times also in solids [7, 42]. HHG in solids originates from two main contributions: a laser-driven intraband current and an interband polarization, which includes electron-hole recollisions [8, 42]. While generalizations are difficult and still under debate, it is mostly accepted that the former effect (intraband) is dominant for below-band-gap harmonics, whereas the latter (interband) mainly contributes to above-band-gap harmonics [42]. Either way, the laser-driven sampling of the band structure in solid HHG implies a high sensitivity of HHG to subtle microscopic changes in electronic and lattice structures [41, 69, 130–135]. Thus high-harmonic spectroscopy has been used for all-optical detections of nanostructures [87], band structure [131, 132], dynamical Bloch oscillations [110], and the superconducting phase [133]. Moreover, the exquisite time resolution of high-harmonic spectroscopy has been utilized to control electron motion in dielectrics with attosecond accuracy [8, 136]. These characteristics highlight the remarkable capability of high-harmonic spectroscopy that we apply here to decipher photo-induced IMT processes with high sensitivity and temporal resolution. The availability and close-room-temperature IMT have made VO2 (T_c ~340 K) one of the best-studied strongly correlated materials. However, the low T_c makes thermal IMTs and effects from laser excitation difficult to separate from the non-thermal transition[56, 137], which challenges all subsequent efforts to disentangle electron-electron and electron-lattice mechanisms. Therefore, we chose niobium dioxide (NbO2), a $4d^1$ isovalent compound of VO2 to implement time-resolved HHG probing of phase transitions. NbO2 exhibits an IMT between a body-centered tetragonal (bct) semiconducting phase and a regular rutile metallic one, but at a much higher temperature of $T_c \sim 1080$ K [138, 139]. In this letter, the photo-induced non-thermal IMT in the thin film NbO2 is investigated by time-resolved high-harmonic spectroscopy and identified via a characteristic step-like reduction of HHG efficiency when the excitation surpasses a threshold (~ 11-12 mJ/cm^2). The model analysis and theoretical simulations both confirm the remarkable influence of IMT on HHG efficiency reduction. The fluence dependence and the transient change of this step-like reduction also indicate the local growth and the ultrafast timescale features of transient metallization in NbO2. These results highlight the capability of high-harmonic spectroscopy, and also provide new tools to investigate photo-induced IMTs.

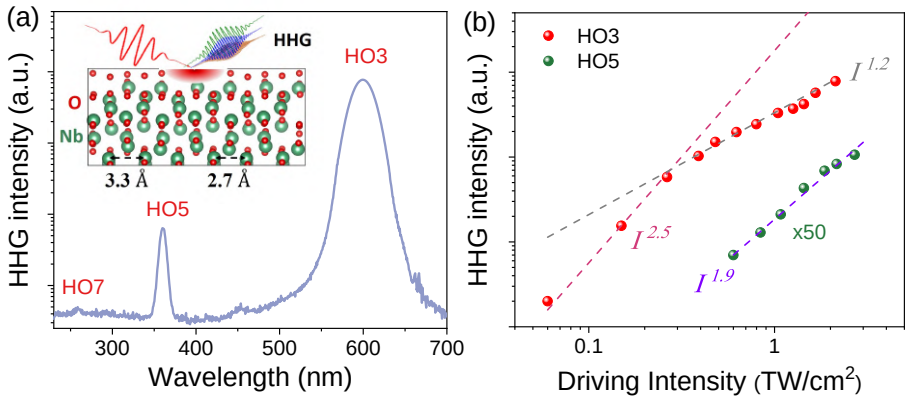


Figure 6.1: (a) Static HHG spectrum from NbO2 thin film, driven by 1.8-µm laser. Third, fifth, and seventh HOs can be clearly observed. The inset displays the experimental reflection configuration. (b) Signals of third and fifth harmonic orders as a function of the driving intensity. The dashed lines represent fitted power laws.

6.2 RESULTS

Polycrystalline NbO2 (115 nm thickness) was grown on a *c*-plane sapphire substrate by reactive bias target ion beam deposition [140, 141]. HHG is produced by a 50-fs and 1.8-µm driving pulse (details in supplementary notes) in reflection mode and collected by a fiber spectrometer (Fig. 6.1a). In the time-resolved measurements, pump pulses at 400 nm are used for photocarrier excitation. The pump fluences are varied between 1 to 25 mJ/cm^2 via polarizers and kept below the threshold of permanent degradation. Considering the linear absorption of NbO2 at 400 nm, the injected carrier density at these fluences is between 1 and 25 $\times 10^{20}$ cm^{-3}.

Figure 6.1a shows an HHG spectrum of NbO2, where the third, fifth and seventh harmonic orders (HOs) of 1.8 μm can be clearly observed. Due to the polycrystalline nature of NbO2, no even harmonic orders are observed. The measured HHG wavelengths are well above the direct (1.3 eV) and indirect bandgap of the thin film NbO2 (0.7 eV). Separating the interband and intraband contributions in our simulations (see supplementary notes) suggests that interband contributions are dominant. However, we cannot make a definitive assignment of the mechanism due to the complex band structure complexity of NbO2, which is also not the main point of our work. The third and fifth harmonic orders (HO3 and HO5) as a function of the driving intensity are plotted in Fig. 6.1b. The vacuum driving intensity of the 1.8-μm pulse is tuned from 0.05 to 3 TW/cm^2, corresponding to an electric field inside the sample of 0.33 to 2.7 V/nm. For lower intensities, HO3 follows $I^{2.5}$, close to the predicted power law of the perturbative theory. A slope change for HO3 is found when increasing the intensity beyond 0.25 TW/cm^2, where signals are nearly proportional to the driving intensity. Regarding HO5, the measured signal does not follow a power law expected from perturbative behavior but scales with $I^{1.9}$. While HO3 and HO5 are technically not high orders of the nonlinear response, their non-perturbative scaling with laser intensity justifies the classification of the underlying process as HHG. For our work, a high driving intensity (precisely 0.6 TW/cm^2 for HO3 and 1 TW/cm^2

for HO5) guarantees that all harmonic orders result from a non-perturbative nonlinear response.

To investigate HHG in different phases of NbO2, various pump fluences are applied to excite photocarriers and trigger a potential IMT. Figure 6.2a shows transient spectra of HHG at three pump-probe delays for an excitation fluence of 6 mJ/cm^2 (extended data in Fig. 6.5). The photocarrier injection leads to a rapid reduction of all observed harmonic orders, similar to observations in conventional semiconductors [68, 152]. It should be noted that the nearly full suppression of HHG signals can persist for hundreds of picoseconds as shown in Fig. 6.6. Signal recovery occurs on much longer time scales (not discussed in the present study) and may be affected by the nanosecond photocarrier recombination in NbO2 [141, 153]. Transient changes as a function of pump-probe delay for the integrated harmonics orders HO3 and HO5 are plotted for various excitation fluences in Fig. 6.2b and 6.7. Their dynamic behaviors are similar, but HO5 is suppressed more than HO3 following photocarrier injection, as shown in Fig. 6.8. Transient HHG signals reach the maximum suppression within 150 fs. Complete suppression of the signal (corresponding to ΔI_{HHG}=-1) with increasing excitation fluence is possible, enabling to tune nonlinear signals via optical or electronic excitation of carrier density. Subsequently, the HHG signals rapidly recover with a fitted lifetime of 0.3-0.4 ps, especially for low-fluence excitations, possibly related to fast Auger-Meitner recombination. However, this rapid recovery starts to diminish when the excitation becomes stronger, in contrast to the many-body effect in conventional semiconductors. Moreover, full quenching of HHG at the highest fluence can persist for tens of picoseconds without any relaxation, which is only observed in strongly correlated materials [13] This gives a first indication of the potential contribution of other mechanisms, such as an IMT, besides classical photocarrier dynamics. Before substantiating that argument, we first examine the dynamic behavior of transient HHG in the semiconducting NbO2 (at low fluence).

For HHG in solids, photoexcited free carriers have been found to reduce generation efficiency, and both ground-state bleaching by photoexcitation as well as a reduction of the dephasing time have been invoked as possible reasons[68, 141, 152, 154, 155]. To link the HHG suppression to photocarrier density, transient changes of HO3 and HO5 are shown as a function of the excitation fluences in Fig. 6.2(c-d) for three pump-probe delays. For delays right after time zero (e.g. 110 fs), we observe a signal suppression in HO3 and HO5 with a rapidly increasing slope for low fluences which saturates and shows complete suppression at high fluences. Similar behaviors are observed in the lower driving intensity (perturbative regime) (Fig. 6.9), and at longer driving wavelengths (Fig. 6.10). We fit the HHG signal suppression right after time zero (110 fs in Fig. 6.2(c-d)) or at low fluence with a phenomenological saturation model based on the semiconducting response, as detailed in SI. Importantly, we note that the observed suppression saturation (fit for HO3 and HO5) should be a general feature of photo-excited HHG in semiconductors and dielectrics, and has already been observed for many other materials [68, 141, 152, 154]. For later time delays (> 200 fs) in Fig. 6.2(c-d), the suppression of HO3 and HO5 at high fluence shows a remarkably different behavior rather than the usual saturation features observed at early delays and previously in the literature. The lower-fluence data again fit well by the saturation model, indicating a typical semiconductor-like response to HHG and its photocarrier-induced suppression. However, for fluences above a threshold F_{th} of 11-12

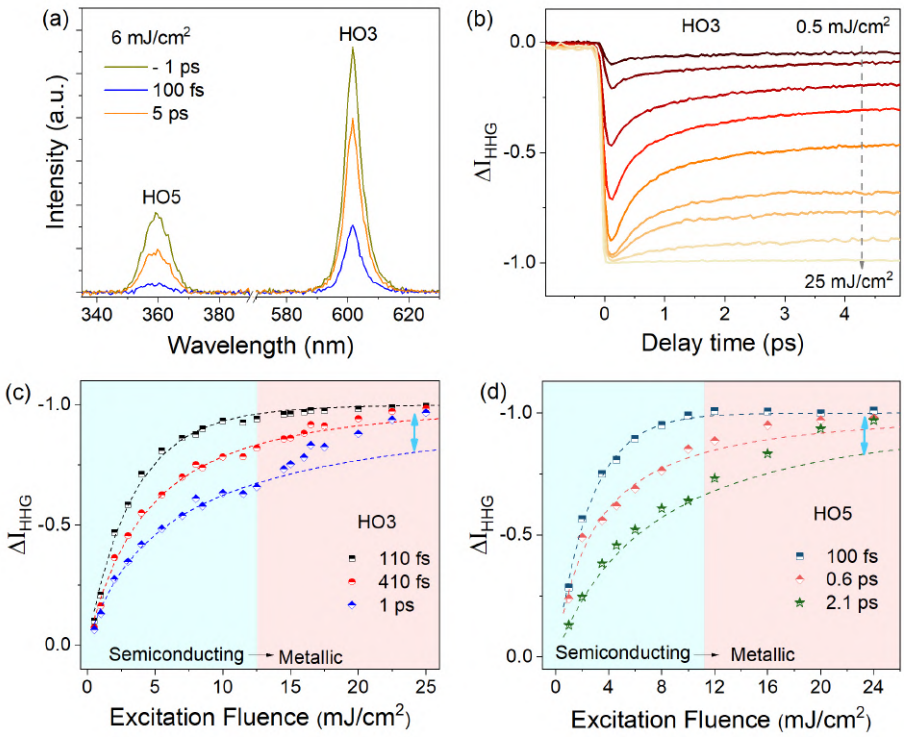


Figure 6.2: Time-resolved HHG in NbO2 thin film. (a) Transient HHG spectra for selected pump-probe delays at excitation fluence of 6 mJ/cm^2. (b) Transient change of HO3 under a series of excitation intensities, where 0 and -1 represent the intact value and full suppression of HHG. (c-d) Transient changes of HO3 and HO5 as a function of excitation fluence at several delay times. The dashed lines are fits based on the saturation model.

mJ/cm^2, the HHG suppression shows a stepwise increase (marked by cyan arrows in Fig. 6.2), which is also observed at the same fluence in independent measurements for HO5 (Fig. 6.2d) and HO3 at a longer driving wavelength (Fig. 6.10). This steplike suppression increase and significant deviation from the characteristics of the saturation model is a hallmark sign of an insulator-to-metal phase transition: Once the fluence reaches a threshold for sufficient photocarrier excitation, the supplied carriers modify the potential surface and weaken bonding to trigger metallization, and the emerging metallic phase causes a sudden steplike change in HHG signal. Previous studies on NbO2 indicated a photo-induced metallization near the same fluence F_{th} by THz and coherent phonon spectroscopic [141, 156]. HHG spectra have been reported in several strongly correlated materials theoretically [13, 69, 157–159] and experimentally, including time-resolved measurements of VO2 [13], but such steplike suppression has not been reported before and considered as robust evidence for phase transition.

To reinforce the above interpretation of photo-induced IMT revealed by HHG, simulations of the HHG process have been performed for both the semiconducting and metallic phases of NbO2, by means of a combined approach of *ab-initio* methods and solving

the semiconductor Bloch equations [150]. As shown in Fig. 6.3a, the band structures of these two phases (metallic rutile, and semiconducting bct) are calculated by Density functional theory (DFT) and projected onto Wannier orbitals to solve electron dynamics numerically. Figure 6.3b shows the calculated HHG spectra from the two distinct phases of NbO2, based on the experimental parameters used above. Stronger HHG signals can be observed in the bct phase than in the rutile one, consistent with experimental observation, where the metallic phase has a lower nonlinear efficiency. As shown in the inset of Fig. 6.3b, HO3 in the rutile phase is less than half of that in the bct phase. Such efficiency difference is enhanced in HO5, supporting the conclusion from Fig. 6.2, that higher-order nonlinearities are more sensitive to metallization. Interestingly one can also find a larger fundamental harmonic signal (i.e. N=1) in the rutile, compared with the bct, which could be attributed to the high reflection efficiency of the metallic phase and interpreted as evidence of the IMT. The transient reflection change of our sample in Fig. 6.12 reproduced this phenomenon and also verifies the validity of our simulations. Thus, HHG simulations in NbO2 under different phases demonstrate that metallic formation can indeed abruptly and significantly reduce HHG efficiency. To highlight the remarkable influence of metallization on HHG efficiency, we further performed another numerical simulation using a modified version of the Peierls model (see SI for more details). The effect of the bandgap on the HHG spectra is explored and the corresponding results are shown in Fig. 6.3(c-d). The HHG spectrum and efficiency are extremely sensitive to bandgap variations. In the upper panel of Fig. 6.3d, the gap shrinkage results in a gradual efficiency reduction of HO5. This effect may play a limited role in transient HHG changes, but can not explain the anomalous steplike deviation from the saturation model in Fig. 6.2(c-d). The complete collapse of the band gap, leading to a sudden and considerable drop in HHG efficiency in the upper panel of Fig. 6.3d, can provide us with a reasonable answer: once the excitation fluence exceeds F_{th}, the system enters a transient metallic phase and thus HHG signals are nearly completely deactivated, as shown in Fig. 6.3d. Therefore, metallization (i.e. bandgap collapse) beyond F_{th}, accounts for the obvious deviation from the saturation model in Fig. 6.2(c-d), corroborating our interpretation of the observation of photo-induced phase transition.

Figures 6.2 and 6.3 establish the presence and sensitivity of HHG to an IMT. Moreover, we have shown that the saturation model captures transient HHG from the semiconducting phase below F_{th}, and transient metallization leads to a step-like deviation at higher fluence. Thus, to isolate the transient emergence of the metallic phase from the general transient semiconducting response following photoexcitation, we subtract the fitted saturation model from transient data in Fig. 6.2 for all time delays. The isolated HHG responses are interpreted as the emergence of the metallic phase and the corresponding phase fraction can be calculated and plotted in Fig. 6.4a as a function of the excitation fluence for various time delays (details in SI). After time zero, the metallic phase fraction starts increasing with the excitation fluence ($> F_{th}$) but stays similar for a long delay time. The fluence-dependent phase fraction is indicative of a spatially inhomogeneous transition, and such an explanation is also supported by the observation that the significant deviation in Fig. 6.2(c-d) above F_{th} is rather gradual than abrupt. In fact, similar nanoscale nucleation has also been found in other phase-transition materials via modern nano-imaging techniques and assigned to crystal imperfections [56, 160].

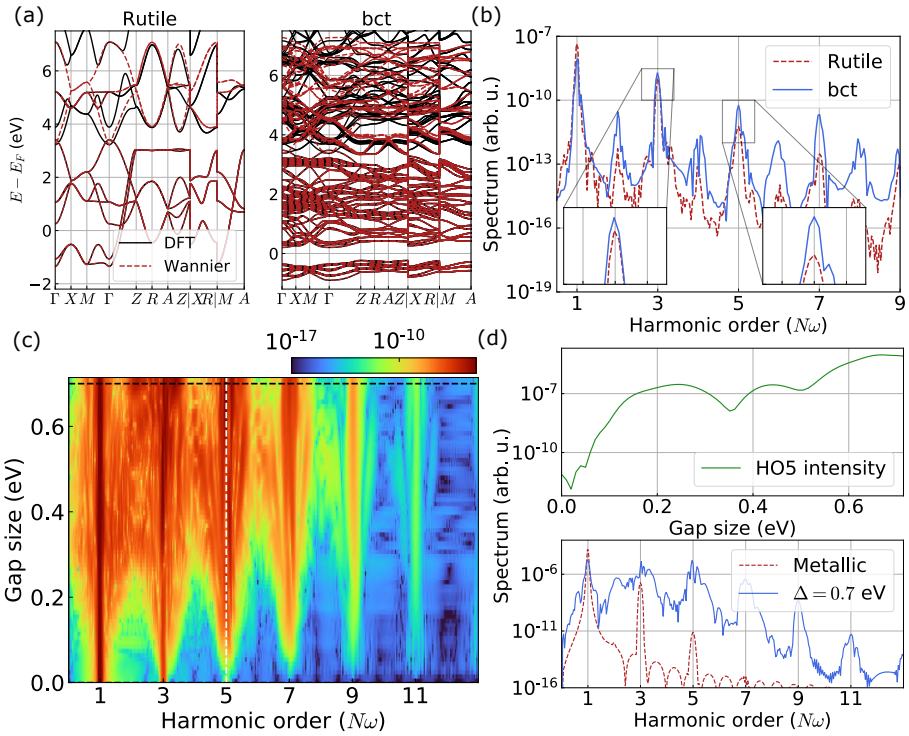


Figure 6.3: Theoretical simulations of HHG spectra in NbO2. (a) DFT band structure for both the metallic rutile and semiconducting *bct* phases. Black lines depict the full DFT calculation while red ones show the band structure after a wannierization procedure. (b) HHG spectra in the rutile and *bct* phase, using the full *ab-initio* model for the NbO2. The insets depict a zoom around HO3 and HO5 respectively. (c) HHG spectra of the Peierls model in terms of the gap size. (d) Two snapshots of (c). The upper panel, corresponding to the vertical white line in (c), depicts the intensity of the fifth harmonic as a function of the gap size. The lower panel, extracted from the horizontal black line in (c), shows the HHG spectra comparison between the metallic and insulating phases (with a gap of 0.7 eV which is roughly the gap in NbO2).

Besides spatial information on the IMT, the isolated IMT response in the time domain also allows tracking its emergence time scale. The inset of Fig. 6.4b displays the transient responses of the metallic phase for selected fluences, which shows that the IMT responses are absent for low fluence and only exist when the excitation fluence exceeds the threshold F_{th} – key signatures of phase transitions. Following photoexcitation at high fluence, the transient response from IMT emerges rapidly and the HHG suppression lasts long. Its emergence rate corresponds to the timescale of the IMT, and the extracted full width at half maximums (FWHM) of these rates are plotted in Fig. 6.4b and the fitting process can be found in SI. The time scale of IMT seems constant (from 110 to 90 fs) within error bars (20 fs), below the instrumental resolution (~ 70 fs) in our experiment. The direct fitting of transient HO3 changes in Fig. 6.14 also leads to the same conclusion: the rising edge becomes sharper when transient metallization occurs and eventually shows the shortest FWHM of 105 fs.

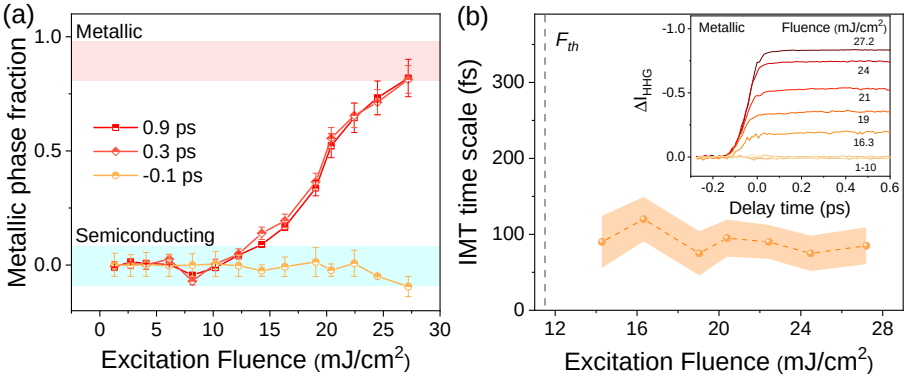


Figure 6.4: Phase diagram and time scale of IMT (a) Metallic phase fraction as a function of the excitation fluence, calculated from the difference between transient HHG signals and the saturation model in Fig. 6.2. (b) Timescale of phase transition, extracted from transient HHG response of newly emerging metallic phase. The inset shows the transient response of the metallic phase at different fluences. The FWHMs of the emergence rate of the metallic phase are fitted and taken as the timescale of phase transition.

Such a short timescale of IMT benefits discovering the driving forces of the IMT. According to the thermal capacity of NbO2 [161], the *upper* limit of the lattice temperature induced by laser heating is estimated to be < 500 K at F_{th}, much lower than the phase transition temperature (T_c ~1080 K). (The estimation details seen in SI) This not only confirms the nonthermal nature of transient metallization in NbO2, but also means that the lattice transformation has no obvious contribution to the steplike variation of the emitted harmonics, and transient metallization with the *bct* lattice, as intermediate states, may be an ultrafast and nonthermal phase transition [61, 128, 129]. It should be highlighted that transient metallization without complete lattice transformation does not justify an interpretation of a pure breakdown of electron-electron correlation (Mott interaction) following excitation. Ultrafast and local lattice distortion has also been found near F_{th} via coherent phonon spectroscopy [141], and the timescale we measured in the present study is close to a half period of the phonon mode, mainly for dissociating the Nb-Nb dimer-the characteristic lattice change in the temperature-induced IMT. This motivates revisiting the current experiments with even shorter pulses in order to distinguish structurally driven (Nb-Nb dimer dissociation) from electronically driven (Mott) transitions by their different time scales.

6.3 CONCLUSIONS

Our experiment represents the first unambiguous evidence of photo-induced IMT in strongly correlated materials via transient high-harmonic spectroscopy, which is apparent as a large deviation of transient HHG from the typical semiconductor response following photoexcitation. This method can be regarded as a robust strategy and general evidence for measuring photo-induced IMTs in strongly correlated materials using HHG. Our experimental findings are fully supported by HHG calculations from both the *ab-initio* theory in NbO2 and a Peierls model. Moreover, our analysis supports a local nucleation

process and ultrafast metallization process emerging with nanotexture for fluences just above the threshold. The time scale of the phase transition of 100 fs which we extract from our data indicates a non-thermal transition, that motivates experiments with even higher time resolution and ideally spatial resolution to address the emergent nanotexture that was indirectly inferred from our data. Finally, we note that the near-complete signal suppression observed at high fluences in NbO2 makes it an ideal candidate for all-optical switches and control, a key aspiration for ultrafast IMTs and strongly correlated materials.

SUPPLEMENTARY FIGURES

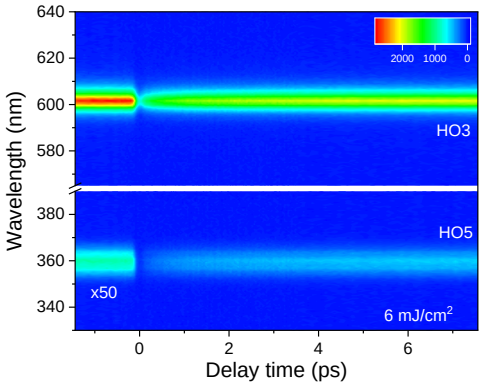


Figure 6.5: 2D map of transient HHG spectroscopy, including HO3 and HO5, excited by a fluence of 6 mJ/cm^2. A short-pass filter was used to reduce the signal intensity of HO3.

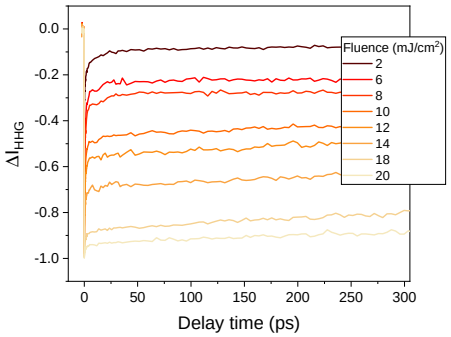


Figure 6.6: Transient change of HO3 within a long delay time, suggesting that HHG suppression could persist hundreds of ps

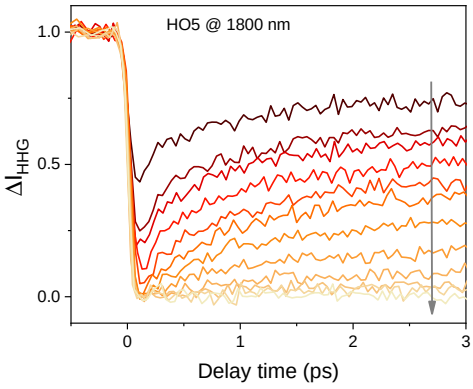


Figure 6.7: Dynamical curves of HO5 suppression under several excitation fluences.

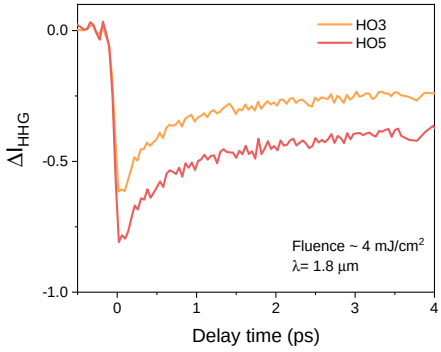


Figure 6.8: The dynamical comparison between HO3 and HO5, and higher order signals display a larger response at the same conditions.

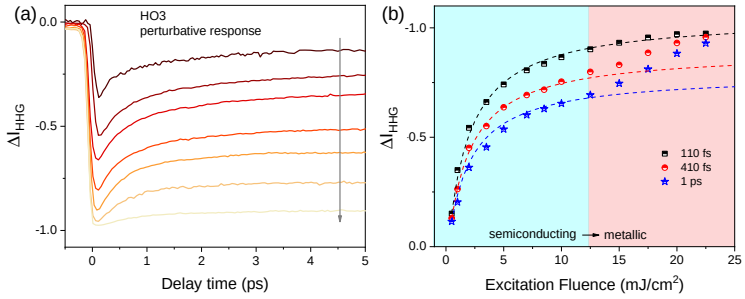


Figure 6.9: Transient HO3 at the perturbative regime. (a) Dynamical curves of HO3 at different excitation fluences, showing a similar change. (b) Transient change of HO3 as a function of the excitation fluence. The dashed lines are from the saturation model, and a similar model deviation can be observed at a similar fluence.

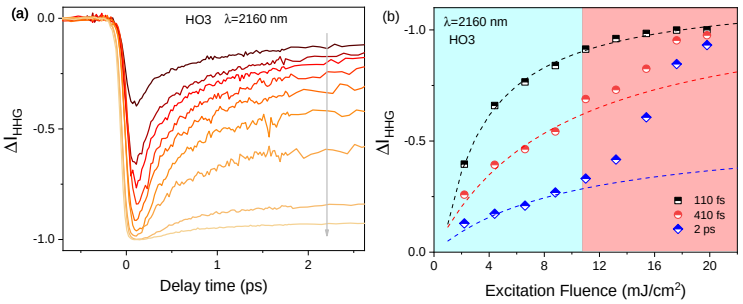


Figure 6.10: Transient HHG measurements probed at 2160 nm. (a) Dynamical curves of HO3 and (b) The HHG suppression at three different delay times under different fluences.

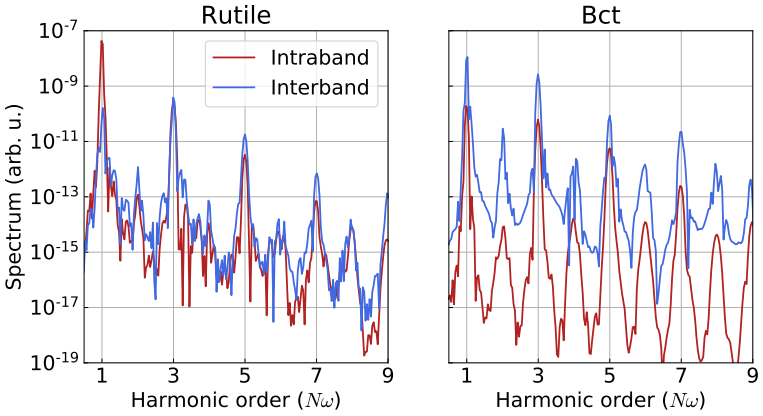


Figure 6.11: HHG spectra for both the rutile and *bct* phases where intraband and interband contributions are distinguished clearly.

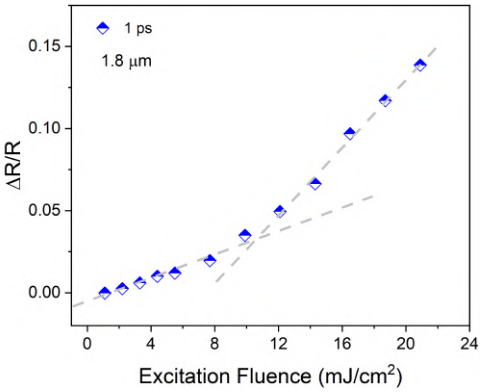


Figure 6.12: Transient reflection change of fundamental wavelength (1.8 μm) at 1 ps as a function of the excitation fluence. A slope change can be observed apparently near 11 mJ/cm^2 (the threshold for the phase transition).

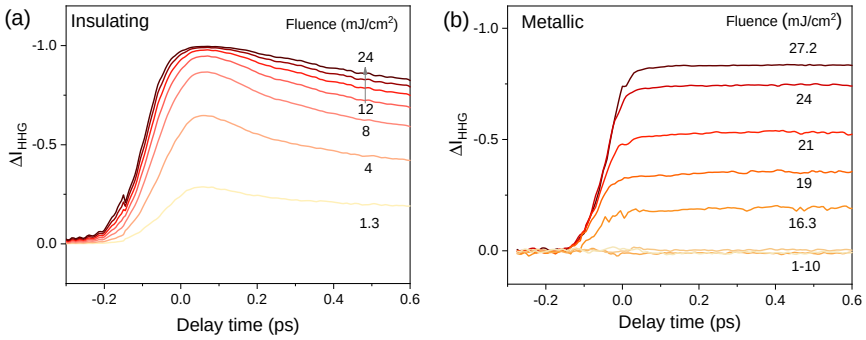


Figure 6.13: Transient HHG responses from (a) the semiconducting phase and (b) the metallic phase at a series of excitation fluences, calculated from the saturation model.

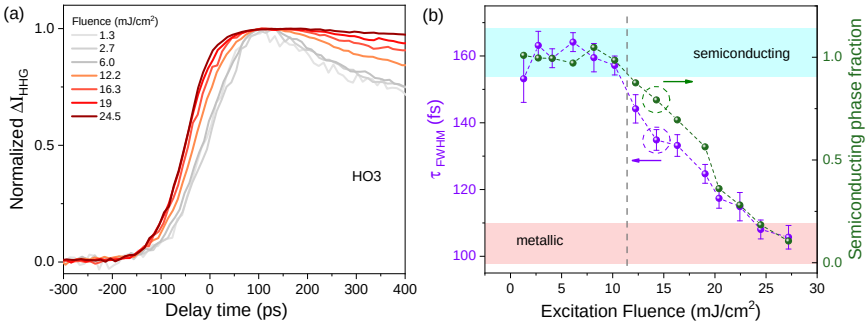


Figure 6.14: (a) The normalized dynamical curves of transient signals at HO3, where grey lines are from the low fluence and red lines represent the results above the threshold. (b) The fitted FWHM of the rising edge in (a) as a function of excitation fluences. The semiconducting phase fraction is also plotted for comparison.

SUPPLEMENTARY NOTES

MATERIAL CHARACTERIZATIONS

The polycrystalline NbO_2 investigated here was grown on a *c*-plane sapphire substrate through reactive bias target ion beam deposition (RBTIBD), and the details of growth conditions can be found elsewhere [140, 141]. The thickness of our sample is determined to be ~ 115 nm by X-ray reflectivity. The Raman spectrum shows two main peaks at 155 and 185 cm^{-1}, consistent with previously reported Raman modes of bct-NbO_2 films [142, 143]. In addition, the X-ray diffraction 2θ scan displays only two peaks at $2\theta = 37°$ and 79°, corresponding to the (440) and (880) diffractions of bct-NbO_2. No Raman or X-ray diffraction peaks of other oxide components (NbO or Nb_2O_5) are observed. Thus, it can be concluded that the studied polycrystalline film is predominantly the semiconducting bct phase of NbO_2 with the $(110)_{bct}/(100)_{rutile}$ orientation along the out-of-plane direction.

EXPERIMENTAL SETUP

To measure the static and transient HHG spectra in NbO_2 film, a commercial Ti:Sapphire laser amplification system (Astrella from Coherent) works as the femtosecond laser source, where the 35-fs pulses are generated with a central wavelength of 800 nm. The total pulse energy of 6 mJ is divided into two beams: the majority of laser power for the optical parametric amplification system (OPA) to generate longer wavelengths ranging from 1.6 to 2.4 μm, and the residual part for the frequency doubling to work as the pump beam [162]. The idler pulses of the OPA at 1.8 μm are chosen as a probe and focused onto the sample surface by a f=20cm focusing lens. The pulse duration of the 1.8 μm idler was measured to be 54 fs through FROG and the 400-nm pulse was estimated to be 57 fs via another independent measurement without phase transition. The reflected HHG signals from the sample surface are directly collected by a fiber spectrometer (Avantes). First test measurements were done with and without a lens in front of the fiber, which did not show any difference in measured dynamics. Then, we mounted the fiber entrance on an x-y positioner without the lens, which allowed scanning the fiber over the harmonics over several hundreds of micrometer without changing the signal. This gave us confidence that this was a viable way of collecting the light. Another beam with a frequency doubling to 400 nm works to inject photocarriers into the sample. It should be mentioned that the powers of these two beams can be tuned through waveplates and polarizers, but their polarizations are fixed as *p* polarization for all measurements. To avoid parasitic multiple reflections at the various interfaces for both pump and probe pulses, we applied two larger incident angles for these two beams (60 and 40 degrees for pump and probe). The corresponding spot sizes of 250 and 45 μm for the pump and probe, respectively, ensure homogenous excitation within the probed volume. To measure the transient HHG response, one motorized stage (Physik instruments) is employed to change the optical path of the pump beam, and one optical shutter (Vincent Associates) is also installed in the pump beam to create pump on and off states to extract transient HHG changes.

THE COMPARISON BETWEEN PERTURBATIVE AND NON-PERTURBATIVE THG DYNAMICS

As shown in Fig. 6.2b and Figure 6.9a, the dynamics of HO3 under the perturbative and non-perturbative regimes indeed look quite similar, even though the perturbative response is somewhat less pronounced. In principle, the perturbative HO3 response should also be sensitive to the IMT, because the transition from the insulating to metallic states can alter the material properties a lot and the local nonlinear polarization should be changed during IMT. Due to the difference in the physical origins, the non-perturbative response is theoretically expected to be more sensitive to IMT than the perturbative one.

THE SATURATION MODEL FOR PHOTO-EXCITED HHG

Transient reductions of HHG signals in solids have been reported and investigated in many materials, but the main mechanisms behind the interesting HHG suppression are an open question. According to the microscopic generation process of HHG, the carrier population and dephasing time of coherent electron-hole pairs are supposed to determine signal strengths directly. It has been verified that incoherent carriers have a deleterious influence on these two factors. Such carriers are created by either photoexcitation or electrical doping [68, 144, 154]. These incoherent carriers can reduce the tunneling probability of coherent electrons, driven by the probe beam, due to the phase space-filling effect and the variation of the joint density of states between valence and conduction bands. More importantly, these pre-existing carriers also lead to enhanced electron-electron scattering and largely reduce the dephasing time. Some relevant experiments and simulations reported the scattering enhancement as the main reason for transient HHG change [12, 68, 154]. and photon-echo spectroscopy in GaAs[145] also supports this claim: the dephasing time T_2 of coherent electrons can be phenomenologically described as $T_2 \propto (N+n_0)^{-0.3}$, where n_0 represents the intrinsic carrier density and N defines photocarrier density excited by the pump pulses. Generally, the intrinsic carrier density can be calculated roughly by electrical transport measurements and based on the measured conductivity in our sample at room temperature, n_0 is estimated to be 10^{18} cm^{-3} [140, 146]. although this value is always underestimated and not strictly comparable with photo-excited carriers. Regarding the contribution of pump excitation, the sample absorption and subsequent photocarrier dynamics could help calculate transient carrier density. Our sample shows a nearly constant absorption rate at the investigated fluence range, and the corresponding initial photocarrier density has been mentioned in the main text of this letter. Photocarrier dynamics in NbO_2 have been studied before via transient absorption[141, 153] and the decay equation can be directly used here. Although the microscopic and well-defined mechanism between HHG suppression and the dephasing time is still lacking, the characteristic of transient HHG in semiconductors could be phenomenologically described well by a simple exponential function of the dephasing time T_2: $I_{HHG} \propto e^{-\tau_{HHG}/T_2}$, where τ_{HHG} is one parameter about the emission time of specific harmonic order [68, 154]. Thus transient HHG signals in semiconductors can be linked to the applied excitation fluence. The above model can reproduce well experimental data in Fig. 6.2 (dash lines) and is named as the saturation model, due to the curve shape. It should be mentioned that the saturation model proposed here is also supported by transient HHG from two-dimensional materials [68, 147, 154] and perovskite

thin film recently found but unpublished. The good agreement between experimental data and the saturation model also confirms that HHG changes under low fluence or initial delay times indeed originate from the transient response of the semiconducting phase of NbO_2, so the deviation from the model can be assigned to photo-induced metallization. Moreover, temperature-dependent HHG signals also support the model assumption used above: static HHG signals start dropping with the temperature increase. Higher temperature will lead to higher intrinsic charge density and strengthen electron-electron scattering [140, 146], which both contribute to the reduction of the dephasing time and then suppress HHG emission largely.

In addition, while a previous report on time-resolved high-harmonic spectroscopy in VO2 has not explicitly shown this steplike change of HHG suppression, our own reanalysis of the author's data from Ref.[13] in fact, shows that the saturation model also fits well transient HHG changes in VO2 at low fluence and a similar steplike suppression change is likely to present. This implies that fluence dependence studies of time-resolved HHG are a highly sensitive way to probe IMTs.

NUMERICAL CALCULATIONS OF HIGH HARMONIC GENERATION IN NbO_2

The field-free band structure and dipole couplings were obtained with the electronic structure code Quantum Espresso [148]. We used a Perdew–Burke-Ernzerhof (PBE) exchange-correlation functional on a Monkhorst–Pack (MP) grid of $9 \times 9 \times 15$ $\boldsymbol{k}$-points for the rutile phase while a MP grid of $4 \times 4 \times 7$ $\boldsymbol{k}$-points was used for the bct phase. Afterward, the field-free tight-binding Hamiltonian used for the propagation was constructed by projecting the Bloch bands onto a set of maximally localized Wannier functions using the Wannier90 code [149]. For both phases, the Bloch states were projected onto the d_{z^2}, $d_{x^2-y^2}$, d_{xy}, d_{xz} and d_{yz} orbitals of niobium. For the bct phase, this meant a total number of 160 orbitals, while for the rutile phase, it meant only 10 orbitals.

The response of the material to the laser field was then obtained by numerically solving the semiconductor Bloch equations in the Wannier gauge, as described in ref. [150]. We simulated the interaction of both phases with a probe field with matching parameters of those used in the experiments: a linearly-polarized $1.8\,\mu$m field with an intensity of 0.2 TW/cm^2. While the theoretical intensity of the laser field does not completely match the experimental one, we have ensured that we are in the non-perturbative regime, so we can accurately and safely compare the experimental results with the theoretical ones. The excitation should occur at the point where the bandgap is, i.e. at the Γ-point. Since both phases have quite different unit cells, the directions of the laser field should also be different. We choose that specific direction, precisely the x-direction in the bct phase and inclined 45 degrees with respect to the x and y directions for the rutile phase, because it is where all the Nb-O bonds lie and therefore, where all the dynamics will happen. In momentum space, the situation gets a bit more complicated. As shown in Fig. 6.3a of the band structure of the material, there is a huge overlap between different bands. This means that the charge carriers will be able to move in almost all symmetry directions (in k-space). To accurately compare both spectra, we first projected the currents in the same direction. For the bct simulation, we used a MP grid of $20 \times 8 \times 2$ $\boldsymbol{k}$-points while for the rutile's case, we used a MP grid of $100 \times 100 \times 8$ $\boldsymbol{k}$-points. We checked that the results were properly converged for both cases. The calculated HHG spectra from both phases

have been displayed in Fig. 6.3 and 6.11. Our simulations also separate the intraband and interband contributions in both phases shown in Fig. 6.11 and support that interband polarization might play a significant role in our observed HHG spectra. In a system such as NbO_2, where one has hundreds of bands, it is rather complicated to completely ensure that the origin of the current is either intraband or interband. Indeed, the more likely scenario is that the origin is a complex combination of the two mechanisms. It is also likely that even higher harmonics would be dominated stronger by the interband mechanisms, however the defect emission and damage threshold of our polycrystalline sample make those higher harmonics, or even a plateau-like emission as could be expected for the interband mechanism, difficult to observe in the current experiments. Future studies that may aim to shed more light on the HHG mechanism should address this by using single-crystalline samples and shorter infrared driving pulses.

Alongside the full *ab-initio* calculation, we also developed a simplified model, to gain more physical insight, based on the Peierls model for one-dimensional dislocations. It consists of a one-dimensional chain with two atoms per unit cell with two types of hoppings, intracell (between atoms inside the same unit cell) and intercell (between different unit cells). The Hamiltonian for such a chain is simply:

$$H = \sum_x t_{\text{intra}} b_x^\dagger a_x + t_{\text{inter}} a_{x+1}^\dagger b_x + \text{h.c.}, \tag{6.1}$$

where $c_x / c_x^\dagger$ is the creation/annihilation operator on site x with c being either a or b. This model has two different phases depending on the magnitude of the hopping parameters. If $t_{\text{intra}} > t_{\text{inter}}$ the system will be insulating with a gap of magnitude $\Delta \sim |t_{\text{intra}} - t_{\text{inter}}|$. However, when both hopping parameters are equal ($t_{\text{intra}} = t_{\text{inter}}$), the system will be metallic as the gap vanishes. Such an atomic chain is also known as the Su–Schrieffer–Heeger (SSH) model. We are aware that this system can host topological phases [151]. However, those states only appears when we have a finite chain, and since we are working with a system with periodic boundary condition, there are no differences between the trivial and the "topological" regimes.

To mimic what happens in NbO_2, we will parameterise the hopping parameters as

$$t_{\text{intra/inter}} = t_0 \exp\left(-\frac{d_T/2 - d_{\text{intra/inter}}}{d_T}\right) \tag{6.2}$$

where $d_T = d_{\text{intra}} + d_{\text{inter}} = 3.5$ Å, which is similar to the Nb-O bond distance in the bct phase, and $t_0 = 1$ eV. We selected those parameters so to match the physics of NbO2. Using this parametrization, this atomic chain will be only metallic when $d_{\text{intra}} = d_{\text{inter}}$. Therefore, by tuning the bonding distances, we will move between insulating and metallic states. The laser parameters were the same as in the *ab-initio* calculation and also the dynamics were solved using the same scheme. We used a grid of 500 $\boldsymbol{k}$-points for the simulations.

THE TIMESCALE EXTRACTION OF TRANSIENT METALLIZATION

Experimental and theoretical studies both confirm that the excitation fluence beyond F_{th} can trigger transient metallization in NbO2, and the efficiency difference of semiconducting and metallic phases leads to HHG deviation from the saturation model. Interestingly,

such deviation increases gradually rather than suddenly. According to previous research on phase transition, this fluence-dependent feature can be explained by the second-order transition or the spatial inhomogeneity of phase transition. Coherent phonon spectroscopy in NbO2 shows no obvious phonon softening and the former hypothesis (second-order transition) can be safely ruled out [141]. Spatial inhomogeneity of IMT has been found in correlated materials, including VO2, via ultrafast microscopy and nano-imaging techniques, and generally assigned to crystal imperfections. The local crystal changes, such as element doping or lattice defects, can result in the entropy increase, and accordingly, reduce the enthalpy requirement for phase transition. Hence, this spatial inhomogeneity could be enabled by the polycrystalline nature of our sample, and local information of IMT, such as the metallic phase fraction P, can be derived from transient HHG changes. It can be assumed that both the newly formed metallic and residual semiconducting phases simultaneously contribute to HHG emission, and considering the much weaker efficiency of the metallic phase, transient HHG signals can be approximately written as:

$$I_{HHG} = P * \alpha_{metal} + (1-P) * \alpha_s(N,t) \tag{6.3}$$

where I_{HHG} is the detected HHG signal, and α_{metal} and $\alpha_s(N,t)$ are HHG efficiency of the metallic and semiconducting phases respectively. It should be noted that α_{metal} can be found from the above simulation and immune to carrier dynamics after metallization, and $\alpha_s(N,t)$ can be calculated by the proposed saturation model related to the excitation fluence and delay time. Via applying Equation (3) to fit experimental data after IMT, e.g. 0.3 and 1 ps in Fig. 6.2, phase fraction P at different delay times can be extracted and plotted in Fig. 6.4a. The phase fraction strongly relies on the excitation fluence and starts increasing beyond F_{th}. A uniform phase transition can be achieved in our sample when the excitation fluence approaches the damage threshold. This phase diagram reveals that transient metallization in NbO2 is a nanoscale nucleation process related to the excitation fluence.

Except for the phase diagram, the timescale of IMT can be also extracted from transient HHG changes in Fig. 6.2 by using Equation (3). The proposed saturation model manages to reproduce the HHG response of the semiconducting phase to the excitation fluence and delay time, as shown in Fig. 6.13a. Combined with the metallic phase fraction P, the isolated IMT response (i.e. the metallic response $P * \alpha_{metal}$) can be calculated and plotted in Fig. 6.13b at a serial of excitation fluences. At low fluence transient HHG changes from the metallic phase are almost negligible. Beyond the threshold F_{th}, HHG signals exhibit a sudden change (reduction), meaning the emergence of the metallic phase. The amplitude of HHG changes in Fig. 6.13b originates from the metallic phase fraction, consistent with Fig. 6.4a. As the derivative operation increases noise on experimental data, we chose another (equivalent) method based on the error function to fit the HHG change shown in the inset of Fig. 6.4b. The equation can be written as:

$$\Delta I_{HHG} = [1 + erf(\frac{t-b}{\tau_p})] \times [A_1 e^{-t/\tau_1} + A_2 e^{-t/\tau_2} + c] \tag{6.4}$$

where b and τ_p are the offset and width of the error function to describe the rising edge and the second brocket represents the subsequent decay processes. According to the mathematical definition of the error function, the full width at half maximum (FWHM)

of the rising edge should be equal to $\sqrt{4\ln 2}\,\tau_p$. The emergence rate of HHG suppression corresponds to the IMT timescale, and its fitted FWHM values are plotted as a function of the excitation fluence in Fig. 6.4b. Considering the uncertainty of measurements and the fitting errors, the FWHM of the IMT timescale stays nearly constant (90-110 fs) for the applied excitation fluences. To verify this analysis, we also normalized experimental data for all excitation fluences and directly fit those rising edges, which are summarized and shown in Fig. 6.14. The FWHM of the rising edge seems to be constant below F_{th}, and then starts decreasing with the fluence increase until the damage threshold. Such interesting dependence of the rising edge is nearly in accordance with the fraction change of the metallic phase. Thus, the constant FWHM (~ 160 fs) of the rising edge at low fluence represents the intrinsic HHG response of the semiconducting phase, and the smallest FWHM (~ 105 fs) means the timescale of IMT or metallization. The intermediate regime is a mixture of two phases, and the rising time is affected by two different responses. Shorter pulses and better models or simulations will help distinguish the nature of IMT.

THE ESTIMATION OF LATTICE TEMPERATURE

Based on the assumption that all absorbed laser energy can be dissipated through lattice heating without any other significant consumption, the lattice temperature rise induced by laser excitation can be estimated by the equation below:

$$\alpha F_{pump} = \frac{t\beta}{M}\int C_p dT \tag{6.5}$$

where the left side represents the total energy absorbed by NbO2, and the right side corresponds to the required energy for a certain temperature rise. Thus, α is the absorption of the pump pulses which is measured to be 0.6 for the sample in this study, and F_{Pump} is the pump fluence. And t is the sample thickness here. M and β are the molar mass and density of NbO2, which are 124.9 g/mol, and 5.9 g/cm^3 respectively. C_p is the heat capacity of NbO2, as a function of the lattice temperature. Using the equation and parameters above, the relationship between the excitation fluence and the estimated maximum lattice temperature can be calculated. The fluence threshold found in HHG measurements (12-13 mJ/cm^2) can only heat the sample to nearly 500K - this number represents an upper limit in the present conditions as elaborated above - which is still not sufficient to trigger IMT thermally (>1000 K). Moreover, considering the phonon emission time and phono-phonon interaction, energy transfer to heat lattice cannot occur within the timescale of IMT extracted from HHG. It can be safely concluded that the transition occurring at the fluence threshold is a non-thermal one and generally transient influence from photo-excited carriers on atomic bonding or lattice distortion should be the main driver for the non-thermal phase transition, which deserves further investigation.

7

HIGH-HARMONIC FIELD CHARACTERIZATION USING AN INTERFEROMETRIC NON-LINEAR CONVERSION TECHNIQUE

High-harmonic generation from solids has proved to be an excellent probe of electronic dynamics in matter. In standard pump-probe measurements, in which a first pulse excites a material, and a second one generates harmonics to track the subsequent changes in electron populations, the time resolution is usually limited by the envelope of both the pump and probe pulses. Achieving subcycle characterization of high-harmonics generated from solids has the potential to dramatically improve the measurable time scale of electronic dynamics.

In this chapter, we propose a technique consisting in producing sidebands via sum-frequency and difference-frequency between odd-order harmonics generated from a solid and their fundamental driver. First results are presenting colinear second and third harmonic generation auto-correlation measurements which were used for means of optimizing alignment of the experimental setup. The creation of a sideband between the third and fifth harmonic emitted from a BBO crystal is demonstrated, serving as a preliminary step towards complete pulse reconstruction.

7.1 INTRODUCTION

Strong-field induced photoexcitation of electrons in solid-state matter, followed by carrier acceleration inside the crystal, and subsequent electron-hole recollision, gives rise to the generation of a coherent pulse of light composed of a set of discrete harmonics of the fundamental driving field [11, 42, 43]. This process, called solid-high-harmonic generation (SHHG), can provide detailed information about the generation medium [8], and has established itself as a prominent tool for probing transient bandgap dynamics [47, 50, 68, 107]. SHHG spectroscopy typically consists in exciting a material with a pump beam, and probe it with a time-delayed NIR laser which generates harmonics. By tuning the time delay between pump and probe, transient HHG spectra can be measured and analyzed to investigate transient decays of excited states. Although this method has offered some very successful output, its achievable time resolution is intrinsically limited to the duration of the probe and pump pulses, and information concerning the relative emission time between each harmonic is lost. Therefore, a new method allowing for SHHG field characterization would be very valuable for gaining more insights on dynamics occurring faster than the optical cycle. A practical example is the investigation of ultrafast phase transitions in correlated materials, with reported timescale as short as a few femtosecond [13, 103, 163].

Accurate field characterization is critical to the development of ultrafast optics both for making a precise diagnosis of laser systems, but also for probing the complex temporal emission from materials. With the widespread introduction of mode-locked lasers, new techniques had to be established in order to overcome the fundamental limits imposed by electronic response time of photodetectors [164]. For intense femtosecond pulses such as the one obtained with Ti:Sapphire oscillators, the two most common techniques for field characterization are Frequency Resolved Optical Gating (FROG)[70] and Spectral Phase Interferometry for Direct Electric Field (SPIDER)[165], which both rely on second-order non-linear processes. For measuring attosecond pulses generated via gas-HHG, the above-mentioned techniques that rely on nonlinear crystals are not applicable because of the lack of availability of such crystals for the relevant high energy range (XUV, soft X-rays). The two main techniques developed for measuring HHG pulses are Reconstruction of Attosecond Beating by Interference of Two-photon Transitions (RABBITT)[30] and attosecond streaking [31], which both depend on measuring the energies of photoelectrons emitted from a gas medium, usually a noble gas.

Applying these techniques to harmonics generated in solids is not trivial. Generating a nonlinear signal (as in FROG) from the already inefficiently generated high harmonics from a solid is challenged by the low photon flux and requires the generate harmonics to fall into the part of the electromagnetic spectrum for which nonlinear crystals exist (ultraviolet, visible, infrared). Techniques relying on ionization (such as streaking or RABBITT) require the generated photon energies to be higher than the ionization potential of noble gases (lowest one being Xenon at 12.1 eV), which make the technique unpractical for harmonics in the UV, visible and NIR. We note that attosecond streaking of HHG from silica has indeed been demonstrated, where the generated energies were high enough to ionize a gas target subsequently [16]. The low photon flux is also a drawback, since the conversion efficiency of SHHG is orders of magnitude lower than gas-HHG [42]. Therefore, new approaches need to be considered to address these limitations.

Among the most noticeable work aiming at characterizing the subcycle SHHG emission, we can first cite the publication of Hohenleutner et al. where a technique combining cross-correlation frequency-resolved optical gating (XFROG) and electro-optic sampling is introduced [17]. In the paper by Bejot et al., an ultra-broadband mid-IR harmonic spectra emitted from ZnO was characterized using plasma-induced frequency resolved optical switching. We can also mention the recent work by Uchida et al. in which a Mach-Zehnder interferometric approach was used to probe the subcycle harmonic field emission in order to track real time dynamics of Floquet states in WSe_2 [166].

In this chapter, we present a new approach to SHHG field characterization, partially inspired by both RABBITT and FROG, which we have labeled Subcycle Characterization of Optical Radiations via Perturbative Interferometry of Odd-harmonics (SCORPIO). Preliminary measurements of collinear harmonic generation, used for optimizing the experimental setup, will first be presented, before showcasing first outputs of the SCORPIO technique, which will be refined at a later stage.

7.2 COLLINEAR HARMONIC GENERATION AUTO-CORRELATION

7.2.1 METHODS

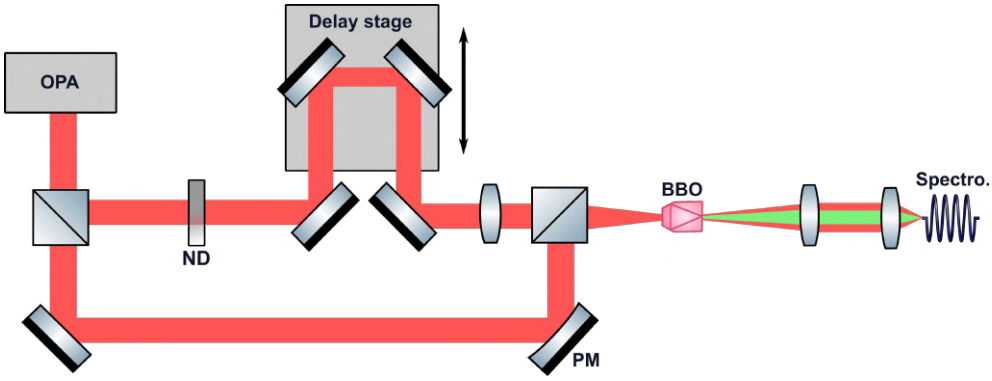


Figure 7.1: Layout of the collinear harmonic generation experimental setup used for alignment. The OPA output is splited in two by a beamsplitter. The first arm is focused on a BBO crystal by a 20 cm focal length parabolic mirror (PM). The second arm is time-delayed with respect to the first arm by moving a delay stage, recombined to the first arm with a second beam splitter, and focused on the BBO using a 20 cm BK7 lens. Harmonics emitted from the crystal are collimated using a 10 cm focal length CaF_2 lens and refocused with a 25 mm focal length BK7 lens in a visible range fiber spectrometer.

Collinear harmonic generation is a preliminary step used for optimizing alignment of the experimental setup for testing the SCORPIO technique. The setup is presented in Fig. 7.1. We use a Ti:sapphire laser (up to 7 mJ, 35 fs, 1 kHz) pumping an optical parametric amplifier with 5 mJ of its total output (TOPAS, Light Conversion) in order to tune the central wavelength of the beam in the near-infra-red (1950 nm central wavelength and a duration of $\approx$ 50 fs FWHM). The OPA output is split in two and both arms are recombined with a beam splitter and focused on a BBO crystal (200 µm thick ; cut for 800 nm type 1 SHG phase matching). Relative time delay between the two beam paths is controlled with

a delay stage and an neutral density filter wheel is used to control their relative power. The time-delayed beam path is focused on the BBO with a 20 cm BK7 lens, while a parabolic mirror with the same focal length is used for the other beam path. The spot size on the BBO is close to 100 µm ($1/e^2$) and the power of both beams is 10 mW. This corresponds to a fluence of 130 mJ/cm^2 and a peak intensity of 2.4×10^{12} W/cm^2. Harmonics emitted from the crystal are collimated using a 10 cm focal length CaF_2 lens and refocused with a 25 mm focal length BK7 lens in a visible range fiber spectrometer.

We will now derive the mathematical formulation of collinear harmonic generation. The complex electric field as function of time is first defined by:

$$E(t) = \mathscr{E}(t)e^{i\omega_0 t} \tag{7.1}$$

where ω_0 is the central carrier frequency and $\mathscr{E}(t)$ is the pulse gaussian envelope. At any time t, the intensity of harmonic order n due to the interaction of two identical pulses, with one being retarded by time τ, is proportional to:

$$I(t) \propto \left|(E(t) + E(t-\tau))^n\right|^2 \tag{7.2}$$

with a power scaling corresponding to the harmonic order. If we are considering SHG process, we then have:

$$I(t) \propto \left|E^2(t) + 2E(t)E(t-\tau) + E^2(t-\tau)\right|^2 \tag{7.3}$$

In a standard non-colinear FROG measurement, the central term, which is solely due to interaction of the two pulses, can be spatially isolated from the other two contributions and measured independently due to the addition of the two driving field momentum vector [70] (see figure 7.2). If the time delay between the two pulses is scanned, the measured signal should be proportional to:

$$I(\tau,\omega) \propto \left|\int_{-\infty}^{+\infty} E(t)E(t-\tau)e^{i\omega t}dt\right|^2 \tag{7.4}$$

We can identify the typical intensity autocorrelation used to recover the fundamental pulse duration in a FROG measurement.

In a collinear FROG measurement, all terms of equation 7.3 are captured by the detector, so that the previous expression becomes:

$$I(\tau,\omega) \propto \left|\int_{-\infty}^{+\infty} (E(t) + E(t-\tau))^2 e^{i\omega t}dt\right|^2 \tag{7.5}$$

It can be shown that this expression can be developed as [167, 168]:

$$I(\tau,\omega) = \left|(1 + e^{-i\omega\tau})E_{SH}(\Delta\omega) + 2e^{-i\omega_0\tau}E_{FROG}(\Delta\omega,\tau)\right|^2 \tag{7.6}$$

with

$$\Delta\omega = \omega - 2\omega_0 \tag{7.7}$$

The term E_{SH} corresponding to

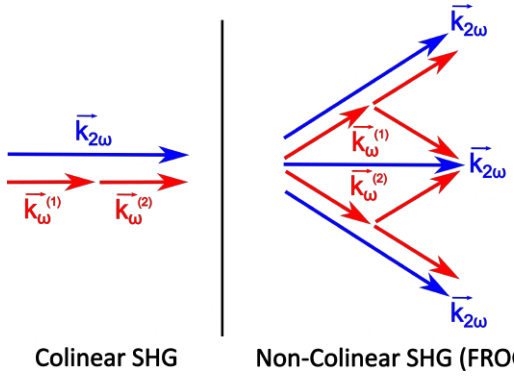


Figure 7.2: Illustration of momentum conservation in SHG process for both colinear SHG (on the left) and non-colinear SHG (on the right). Addition of the two fudamental wavevectors $\vec{k}_{\omega}^{(1)}$ and $\vec{k}_{\omega}^{(2)}$ allows for a single SH propagation axis in the colinear case, and three different ones for the non-colinear case. In a FROG measurement, only the central contribution due to mixing of both fundamentals is measured.

$$E_{SH}(\Delta\omega) = \int_{-\infty}^{+\infty} E^2(t) e^{-i\Delta\omega t} dt \tag{7.8}$$

which is the single-pulse contribution to SH and E_{FROG}, which is the field cross-correlation of the two pulses (see equation 7.4).

$$E_{FROG}(\tau,\Delta\omega) = \int_{-\infty}^{+\infty} E(t)E(t-\tau) e^{-i\Delta\omega t} dt \tag{7.9}$$

Expanding equation 7.6 yields:

$$\begin{aligned} I(\tau,\omega) =& 2|E_{SH}(\Delta\omega)|^2 + 4|E_{FROG}(\tau,\Delta\omega)|^2 \\ &+ 8cos[(\omega_0 + \frac{\Delta\omega}{2})\tau] Re[|E_{FROG}(\tau,\Delta\omega) E^*_{SH}(\Delta\omega) e^{i\frac{\Delta\omega\tau}{2}}] \\ &+ 2cos[(2\omega_0 + \Delta\omega)\tau] |E_{SH}(\Delta\omega)|^2 \end{aligned} \tag{7.10}$$

The first two terms are constant with τ and act as a DC baseband to the measured trace. The third term, is proportional to the product of both the single-pulse and two-pulses SHG contributions, modulated at the fundamental frequency. The last term also acts a constant offset with respect to time delay, but modulated at $2\omega_0$, and can be understood as a spectral interferometry term between the two single-pulse SH contributions.

A similar derivation can be carried out for collinear third harmonic generation [169][170]. We start with the same expression as in equation 7.5, replacing the power exponent by 3:

$$E(\tau,\omega) \propto \int_{-\infty}^{+\infty} (E(t) + E(t-\tau))^3 e^{-i\omega t} dt \tag{7.11}$$

Using the identity $(A+B)^3 = A^3 + B^3 + 3A^2B + 3AB^2$, we can write:

$$
\begin{aligned}
&= \underbrace{\int_{-\infty}^{+\infty} E^3(t)e^{-i\omega t}dt}_{E_1} + \underbrace{\int_{-\infty}^{+\infty} 3E^2(t)E(t-\tau)e^{-i\omega t}dt}_{E_2} \\
&+ \underbrace{\int_{-\infty}^{+\infty} 3E(t)E^2(t-\tau)e^{-i\omega t}dt}_{E_3} + \underbrace{\int_{-\infty}^{+\infty} E^3(t-\tau)e^{-i\omega t}dt}_{E_4}
\end{aligned}
\tag{7.12}
$$

We develop these four field terms separately:

$$
\begin{aligned}
E_1 &= \int_{-\infty}^{+\infty} E^3(t)e^{-i\omega t}dt \\
&= \int_{-\infty}^{+\infty} \mathscr{E}^3(t)e^{i3\omega_0 t}e^{-i\omega t}dt \\
&= \int_{-\infty}^{+\infty} \mathscr{E}^3(t)e^{-i\Delta\omega_3 t}dt \\
&= E_{TH}(\Delta\omega_3)
\end{aligned}
\tag{7.13}
$$

with

$$
\Delta\omega_3 = \omega - 3\omega_0 \tag{7.14}
$$

where $E_{TH}(\Delta\omega_3)$ is the single-pulse contribution to third harmonic field, analog to the term E_{SH} in equation 7.8.

$$
\begin{aligned}
E_2 &= \int_{-\infty}^{+\infty} 3E^2(t)E(t-\tau)e^{-i\omega t}dt \\
&= \int_{-\infty}^{+\infty} 3\mathscr{E}^2(t)e^{i2\omega_0 t}\mathscr{E}(t-\tau)e^{i\omega_0(t-\tau)}e^{-i\omega t}dt \\
&= 3e^{-i\omega_0\tau}\int_{-\infty}^{+\infty} \mathscr{E}^2(t)\mathscr{E}(t-\tau)e^{-i\Delta\omega_3 t}dt \\
&= 3e^{-i\omega_0\tau}E_{cc}(\tau,\Delta\omega_3)
\end{aligned}
\tag{7.15}
$$

in which $E_{cc}(\tau,\Delta\omega_3)$ is the cross-correlation of the two pulses, with one of them squared.

$$
\begin{aligned}
E_3 &= \int_{-\infty}^{+\infty} 3E(t)E^2(t-\tau)e^{-i\omega t}dt \\
&= \int_{-\infty}^{+\infty} 3\mathscr{E}(t)e^{i\omega_0 t}\mathscr{E}^2(t-\tau)e^{i2\omega_0(t-\tau)}e^{-i\omega t}dt \\
&= 3e^{-i2\omega_0\tau}\int_{-\infty}^{+\infty} \mathscr{E}(t)\mathscr{E}^2(t-\tau)e^{-i\Delta\omega_3 t}dt \\
&= 3e^{-i2\omega_0\tau}E_{cc}(\tau,\Delta\omega_3)
\end{aligned}
\tag{7.16}
$$

$$\begin{aligned} E_4 &= \int_{-\infty}^{+\infty} E^3(t-\tau)e^{-i\omega t}dt \\ &= \int_{-\infty}^{+\infty} \mathscr{E}^3(t-\tau)e^{i3\omega_0(t-\tau)}e^{-i\omega t}dt \\ &= e^{-i3\omega_0\tau}\int_{-\infty}^{+\infty} \mathscr{E}^3(t)e^{-i\Delta\omega_3 t}dt \\ &= e^{-i3\omega_0\tau}E_{TH}(\Delta\omega_3) \end{aligned} \tag{7.17}$$

By summing all this field terms, we obtain the following expression for the TH intensity:

$$I(\tau,\omega) = \left| \underbrace{E_{TH}(\Delta\omega_3)(1+e^{-i3\omega_0\tau})}_{A} + \underbrace{3E_{CC}(\tau,\Delta\omega_3)(e^{-i\omega_0\tau}+e^{-i2\omega_0\tau})}_{B} \right|^2 \tag{7.18}$$

Using the identity

$$|A+B|^2 = |A|^2 + |B|^2 + 2\Re\{AB^*\} \tag{7.19}$$

and omitting the $\Delta\omega$ and τ dependency, we have :

$$|A|^2 = 2|E_{TH}|^2(1+\cos(3\omega_0\tau)) \tag{7.20}$$

$$|B|^2 = 18|E_{CC}|^2(1+\cos(\omega_0\tau)) \tag{7.21}$$

$$\begin{aligned} 2\Re\{AB^*\} &= 6\Re\{E_{TH}E_{CC}^*(e^{i\omega_0\tau}+e^{2i\omega_0\tau}+e^{-2i\omega_0\tau}+e^{-i\omega_0\tau})\} \\ &= 12\Re\{E_{TH}E_{CC}^*\}(\cos(\omega_0\tau)+\cos(2\omega_0\tau)) \end{aligned} \tag{7.22}$$

The total intensity can then be written as:

$$\begin{aligned} I(\tau,\omega) = {} & 2|E_{TH}|^2(1+\cos(3\omega_0\tau)) + 18|E_{CC}|^2(1+\cos(\omega_0\tau)) \\ & + 12\Re\{E_{TH}E_{CC}^*\}(\cos(\omega_0\tau)+\cos(2\omega_0\tau)) \end{aligned} \tag{7.23}$$

A plot of this expression for a pulse duration of 100 fs (FWHM) is presented in Fig. 7.5a. The Fourier transform shown in Fig.7.5 shows that three frequency terms are prominent: ω_0 and $3\omega_0$, which could be identified in equation 7.23, and $4\omega_0$, which originates from the last term of the equation.

7.2.2 RESULTS

Figure 7.3a shows the collinear harmonic generation spectra emitted from the BBO crystal as function of time delay, and Fig. 7.3b, for a specific delay around maximum overlap of the two pulses. A wavelength of 1950 nm was chosen in order to generate TH and FH in the visible range, at respectively 650 and 390 nm, and a step size of one micron was used, corresponding to a time resolution of 6.66 fs and a Nyquist frequency of 0.075 fs^{-1}. Harmonics two, three and five can be spotted. Phase matching angle was tuned in order

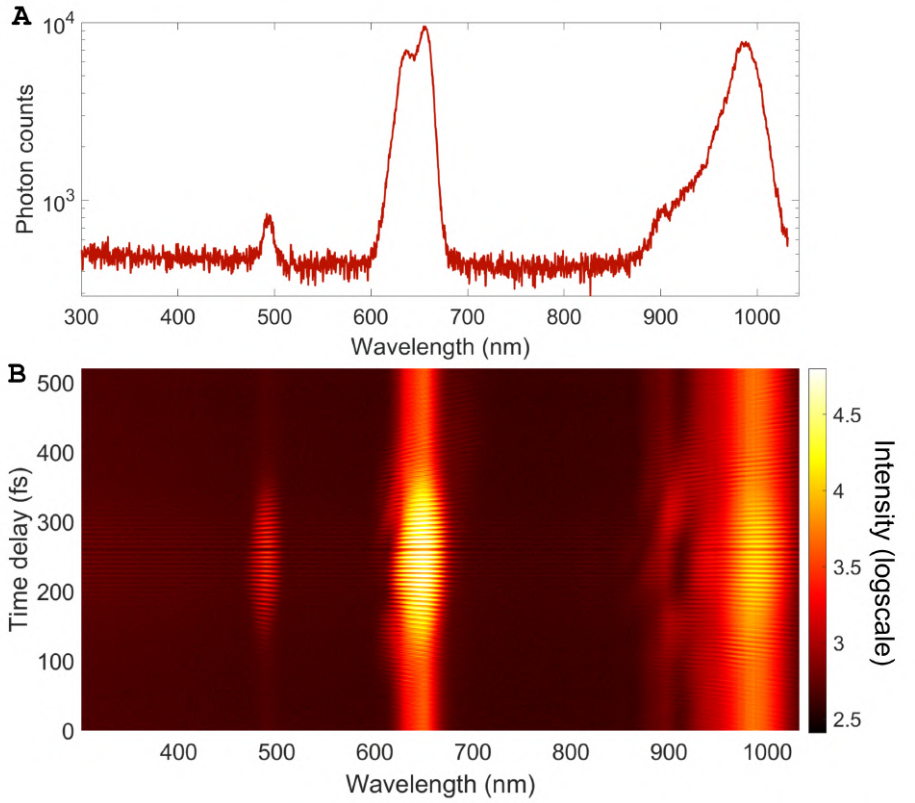


Figure 7.3: Collinear harmonic generation from a BBO crystal, using an OPA output centered at $\lambda_0 = 1950$ nm. a) Spectra measured for maximum overlap of the two pulses. b) Spectral intensity as function of time delay between the two pulses.

to optimize THG and FHG, which explains the similar intensities between second and third harmonic. Interference fringes can be observed on Fig. 7.3a for all harmonics.

Figure 7.4b shows a close up of the spectrally-resolved SH trace, and Fig. 7.4a, the same measurement integrated over the SH spectral peak. This second figure can be compared to the simulated plot for $\omega = \omega_0$, following equation 7.10, in Fig. 7.4c. To produce this plot, the FWHM of the gaussian envelope (100 fs) in Fig. 7.4a was extracted and used as input of the simulation. Interference fringes are partially looking alike between the two figures, with a common oscillating frequency, although the simulation display some more complex patterns not visible in the measurement. The baseline present in the simulation does not appear in the measurement, with an amplitude close to zero outside overlap of the two pulses. By looking at the fourier transform of these two traces, presented in Fig. 7.4d, we can observe the ω_0 oscillation expected from theory is also present in the measurement, but that higher frequencies are missing. The maximum resolvable frequency is indeed limited by the step size used for the delay scan, which would need to be smaller to recover a trace closer to simulation.

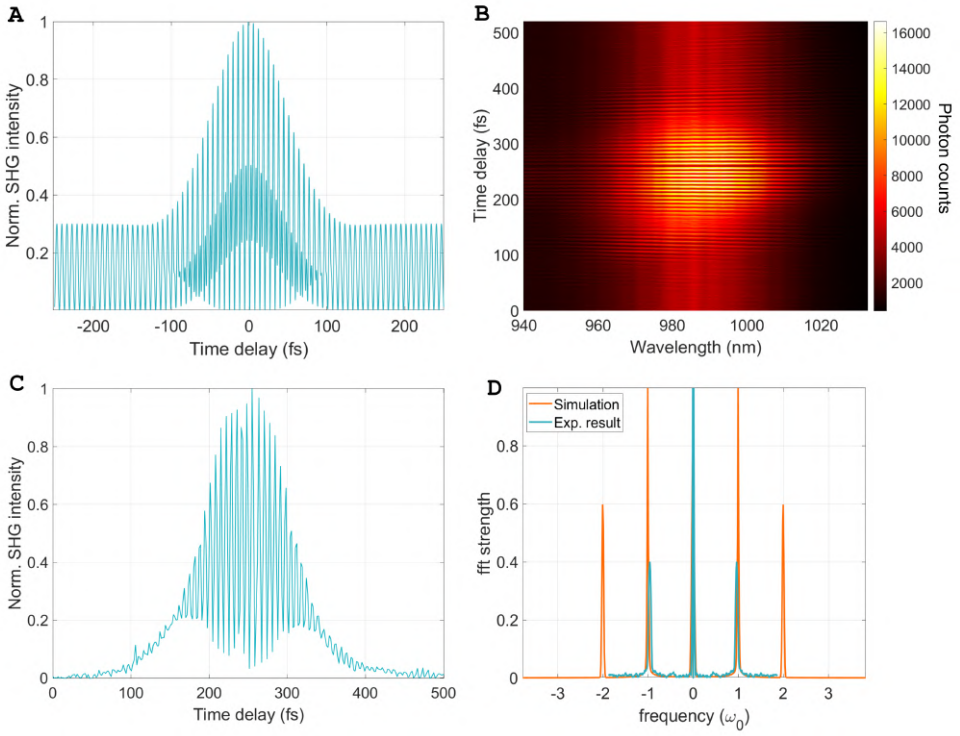


Figure 7.4: Collinear SHG from a BBO crystal. a) Simulation of the time-delay SHG trace for a gaussian fundamental beam of central wavelength $\lambda_0 = 1950$ nm and pulse duration $\tau = 110$ fs. b) Close up on the SH time delay trace from the measurement presented in Fig.7.3b. c) Spectrally-integrated plot of the scan in b). d) FFT of the simulation plot in a) and measurement plot in c).

Similar results can be extracted from the TH time trace close-up in Fig. 7.5b. Figure 7.5a displays the integrated time trace around the TH peak which can be compared to simulation in c, for $\omega = \omega_0$, and a pulse duration of 117 fs (FWHM), extracted from Fig. 7.5a. The two convolutions oscillate at the fundamental frequency as shown in the FFT plots presented in Fig. 7.5d. Once again, higher frequency terms ($3\omega_0$ and $4\omega_0$) are not resolvable due to the finite step size used in the measurement. For both H2 and H3, a very high fringes contrast can be noticed, which confirms that close to optimal overlap of the two pulses in a collinear geometry could be achieved, which is a crucial parameter for optimizing SCORPIO.

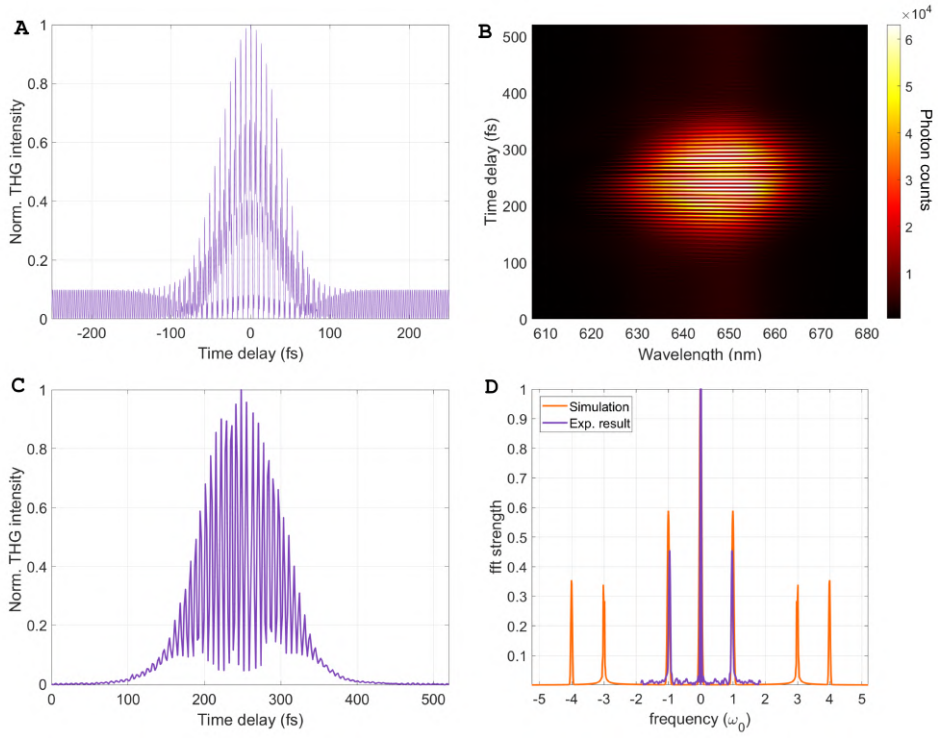


Figure 7.5: Collinear THG from a BBO crystal. a) Simulation of the THG time-delay trace for a gaussian fundamental beam of central wavelength $\lambda_0 = 1950$ nm and pulse duration $\tau = 100$ fs. b) Close up on the TH time delay trace from the measurement presented in Fig.7.3b. c) Spectrally-integrated plot of the scan in b). d) FFT of the simulation plot in a) and measurement plot in c).

7.3 SCORPIO

7.3.1 METHODS

The SCORPIO technique aims at measuring the spectral phase of a discrete number of harmonics emitted from a sample. Only odd-harmonics can be emitted from crystal structures with an inversion symmetry, which is the case for the vast majority of crystals. By focusing these harmonics in a second non-linear crystal, and combine it with a time-delayed field at the fundamental frequency ω_0, even harmonics can be generated through sum-frequency generation (SFG) and difference-frequency generation (DFG). In similar way to the RABBITT technique, these additional harmonics, also called side bands (SB), are reachable by two independent quantum pathways, leading to an interference signal uncoding the spectral phase of odd-harmonics.

Figure 7.6 displays the experimental setup of the SCORPIO technique, in which harmonics generated from a first crystal are combined with a beam at the same fundamental frequency in a second non-linear crystal, for both SFG and DFG process to take place. The setup is similar to the one presented for the autocorrelation measurements, and optics used for focusing on the second crystal and into the fiber are the same. Additional optics

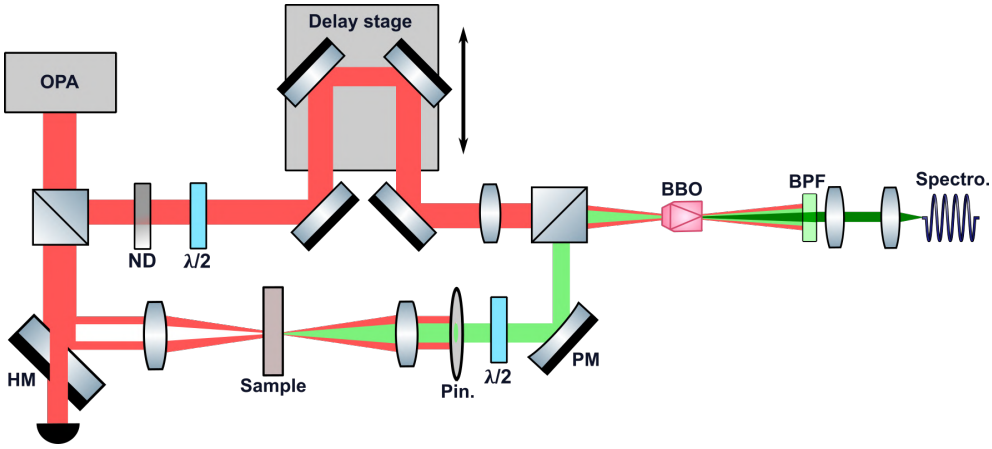


Figure 7.6: Layout of the SCOPIO experimental setup. The OPA output is split in two by a beamsplitter. One of the arms is reflected from a holey mirror (HM) and focused on a first crystal using a 25 cm focal length CaF_2 lens to generate harmonics. After recolimation, the NIR ring is filtered out by partially closing an iris (Pin.) and going through a shortpass filter. The beam is then is focused on a BBO crystal with a 20 cm focal length parabolic mirror (PM). The other arm is delayed by a linear stage, focused on the sample with a 20 cm focal length BK7 lens, and recombine to the other arm with a beamsplitter. Harmonics emitted from the BBO are recolimated by a 10 cm focal length CaF_2 lens, and focused on the fiber spectrometer by a 25 mm focal length BK7 lens. Halfwaveplates are used in each arm to control polarization independently, and ND filtering wheels are used to tune intensities.

are located in the non-delayed beam path in which harmonic generation from a sample takes place, by focusing the NIR beam with a 25 cm focal length CaF_2 lens.

Conversion efficiency from fundamental to harmonic is relatively low, and even more so as the harmonic order increases. As a result, SFG and DFG efficiencies in the second crystal are expected to be very small. Thus, special attention must be given to removing fundamental NIR light from the sample beam path, which is orders of magnitude more intense than harmonics, in order to avoid interactions between the two fundamentals in the second crystal, which would mask the sideband oscillations. For this reason, the sample arm is first reflected from a holey mirror (flat mirror with an opening in the middle) to give the beam a donut-like shape. In focus, the beam is expected to conserve a profile close to gaussian, which can be verified by looking at the beam profile of the generated harmonic, which should also display a gaussian-like profile. After the beam is re-collimated, an iris is used to block the NIR outer ring, and let the harmonics pass through its center. This method can be used to remove most of the NIR and the remaining signal is blocked using a short pass filter. Half-waveplates are also present in each arms to control the polarization, so that both fundamental and harmonics fields are oriented in the same direction.

Let's consider a first SB, harmonic 4, which is accessible by SFG of $3\omega_0$ with ω_0, or DFG between $5\omega_0$ and ω_0. For SFG we have:

$$\begin{aligned} E_{H4}(\tau,\omega) &\propto \int_{-\infty}^{+\infty} (E_{\omega_0}(t) + E_{3\omega_0}(t-\tau))^2 e^{-i\omega t}\,dt \\ &= \int_{-\infty}^{+\infty} E_{\omega_0}^2(t) e^{-i\omega t}\,dt \\ &+ \int_{-\infty}^{+\infty} 2E_{\omega_0}(t)E_{3\omega_0}(t-\tau) e^{-i\omega t}\,dt \\ &+ \int_{-\infty}^{+\infty} E_{3\omega_0}^2(t-\tau) e^{-i\omega t}\,dt \end{aligned} \tag{7.24}$$

The first and last terms of this equation do not contribute to H4 generation since only one of the two frequencies is involved in the convolution product. Expanding the remaining term yields the following:

$$\begin{aligned} E_{H4}(\tau,\omega) &\propto \int_{-\infty}^{+\infty} 2\mathscr{E}_{\omega_0}(t) e^{i\omega_0 t} \mathscr{E}_{3\omega_0}(t-\tau) e^{i3\omega_0(t-\tau)} e^{-i\omega t}\,dt \\ &= 2e^{-i3\omega_0\tau} \int_{-\infty}^{+\infty} \mathscr{E}_{\omega_0}(t)\mathscr{E}_{3\omega_0}(t-\tau) e^{-i\Delta\omega t}\,dt \\ &= 2e^{-i3\omega_0\tau} E_{cc}(\Delta\omega_4) \end{aligned} \tag{7.25}$$

with

$$\Delta\omega_4 = \omega - 4\omega_0 \tag{7.26}$$

The intensity is then:

$$\begin{aligned} I_{H4}(\tau,\omega) &= |E_{H4}(\tau,\omega)|^2 \\ &= E_{H4}(\tau,\omega)E_{H4}^*(\tau,\omega) \\ &2e^{-i3\omega_0\tau} E_{cc}(\Delta\omega_4) 2e^{+i3\omega_0\tau} E_{cc}^*(\Delta\omega_4) \\ &= |E_{cc}(\tau,\omega)|^2 \\ &= \int_{-\infty}^{+\infty} \left| \mathscr{E}_{\omega_0}(t)\mathscr{E}_{3\omega_0}(t-\tau) e^{-i\Delta\omega_4 t} \right|^2 dt \\ &= \int_{-\infty}^{+\infty} \left| A_1 e^{-t^2/2\sigma^2} A_2 e^{-(t-\tau)^2/2\sigma_{H3}^2} e^{-i\Delta\omega_4 t} \right|^2 dt \\ &\propto \exp\left[-\frac{1}{2} \frac{\Delta\tau^2}{\sigma^2 + \sigma_{\mathrm{H3}}^2} \right] \end{aligned} \tag{7.27}$$

We can define an effective standard deviation σ_{eff}:

$$\sigma_{eff} = \sqrt{\sigma^2 + \sigma_{H3}^2} \tag{7.28}$$

We make the following assumption on the pulse duration for the generated harmonics to proceed with the derivation, effectively assuming a perturbative nonlinear temporal response. The duration τ_n of an harmonic pulse of order n therefore verifies:

$$\tau_n = \frac{\tau}{\sqrt{n}} \tag{7.29}$$

with τ being the duration of the fundamental pulse. Therefore, equation 7.28 can be written:

$$\begin{aligned}\sigma_{eff} &= \sqrt{\sigma^2 + (\sigma/\sqrt{3})^2} \\ &= \frac{2}{\sqrt{3}}\sigma\end{aligned} \tag{7.30}$$

Derivation of $E_{H4}(\tau,\omega)$ and $I_{H4}(\tau,\omega)$ for the DFG process is essentially the same, and it can be easily shown that for DFG we have:

$$E_{H4}(\tau,\omega) \propto 2e^{-i5\omega_0\tau}E_{cc}(\Delta\omega) \tag{7.31}$$

with

$$\Delta\omega_6 = \omega - 6\omega_0 \tag{7.32}$$

and that

$$I_{H4}(\tau,\omega) = |E_{cc}(\tau,\omega)|^2 \tag{7.33}$$

with a corresponding standard deviation:

$$\begin{aligned}\sigma_{eff} &= \sqrt{\sigma^2 + (\sigma/\sqrt{5})^2} \\ &= \sqrt{\frac{6}{5}}\sigma\end{aligned} \tag{7.34}$$

We now consider the expression for H4, if both SFG and DFG take place at the same time. We can write:

$$E_{H4}(\tau,\omega) \propto \int_{-\infty}^{+\infty} S(E_{\omega_0}(t) + E_{3\omega_0}(t-\tau))^2 e^{-i\omega t} + D(E_{\omega_0}(t) + E_{5\omega_0}(t-\tau))^2 e^{-i\omega t} dt \tag{7.35}$$

with S and D being the relative SFG and DFG efficiencies. According to results obtained in equation 7.25 and 7.31 for independent SFG and DFG, we have:

$$E_{H4}(\tau,\omega) \propto Se^{-i3\omega_0\tau}E_{cc}^{(S)}(\tau,\Delta\omega_4) + De^{-i5\omega_0\tau}E_{cc}^{(D)}(\tau,\Delta\omega_6) \tag{7.36}$$

while $E_{cc}^{(S)}$ and $E_{cc}^{(D)}$ correspond to the cross correlations of the NIR fundamental with respectively $3\omega_0$ and $5\omega_0$. Using the identity $|A+B|^2 = |A|^2 + |B|^2 + 2\Re\{AB^*\}$, the H4 field intensity can be written as:

$$\begin{aligned}I_{H4}(\tau,\omega) &\propto |E_{cc}^{(S)}(\tau,\Delta\omega_4)|^2 + |E_{cc}^{(D)}(\tau,\Delta\omega_6)|^2 + 2\Re\{e^{-i3\omega_0\tau}E_{cc}^{(S)}(\tau,\Delta\omega_4)e^{+i5\omega_0\tau}E_{cc}^{(D)*}(\tau,\Delta\omega_6)\} \\ &= |E_{cc}^{(S)}(\tau,\Delta\omega_4)|^2 + |E_{cc}^{(D)}(\tau,\Delta\omega_6)|^2 + 2\Re\{e^{i2\omega_0\tau}E_{cc}^{(S)}(\tau,\Delta\omega_4)E_{cc}^{(D)*}(\tau,\Delta\omega_6)\} \\ &= |E_{cc}^{(S)}(\tau,\Delta\omega_4)|^2 + |E_{cc}^{(D)}(\tau,\Delta\omega_6)|^2 + 2\cos(2\omega_0\tau)\Re\{E_{cc}^{(S)}(\tau,\Delta\omega_4)E_{cc}^{(D)*}(\tau,\Delta\omega_6)\}\end{aligned} \tag{7.37}$$

Simulations of the sideband time delay trace, considering both an harmonic and fundamental pulses with a duration of 100 fs (FWHM), are plotted in Fig. 7.8, for even efficiencies in a), and a ratio of 0.1 in figure b). The trace is characterized by a gaussian corresponding to the cross-correlation of the two pulses envelope, modulated at $2\omega_0$. The fringes contrast only depends on the relative efficiencies between SFG and DFG.

If $3\omega_0$ and $5\omega_0$ fields contain an additional phase term $\phi_{3\omega_0}$ and $\phi_{5\omega_0}$, we can see from equation 7.37 that the oscillating term becomes $\cos(2\omega_0\tau + \Delta\phi)$, with $\Delta\phi = \phi_{5\omega_0} - \phi_{3\omega_0}$. Similar results can also be obtained for higher order SB harmonics, for example by measuring harmonic 6, which is accessible by both SFG of $5\omega_0$ with ω_0, and DFG of $7\omega_0$ with ω_0. By simultaneously measuring multiple SB oscillations, it is thus possible to infer the phase difference between each harmonic order. Figure 7.7a shows the simulated SCORPIO trace for SB4 and SB6, with a close up on the two SB in 7.7b. For sake of simplicity, intensity of each harmonic and SFG/DFG efficiencies are set to an equal value. Pulse duration is fixed to 50 fs (FWHM). The phase terms are set to arbitrary values of $\phi_{3\omega_0} = \pi/2$, $\phi_{5\omega_0} = \pi/4$, and $\phi_{7\omega_0} = \pi$, which gives rise to a phase offset observable between H4 and H6 beatings. If intensities and relative phase between each harmonic is known, the full reconstruction of the HHG field as function of time is achievable.

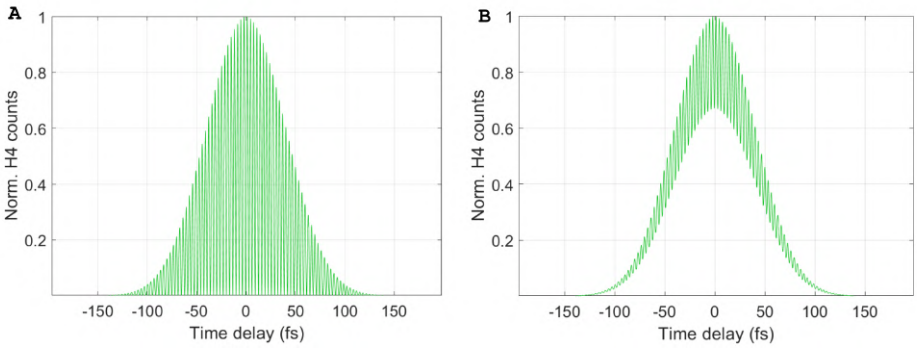


Figure 7.7: Simulation of the H4 sideband intensity as function of time delay between the NIR fundamental, and the harmonic pulse emitted from a sample. The two pulses have the same duration of 100 fs (FWHM). In a) the relative efficiencies of SFG and DFG are the same whereas in b) SFG is ten times more efficient.

7.3.2 RESULTS

The SCORPIO technique requires both SFG and DFG processes to take place at the same time. As shown in Fig. 7.8, if the relative strength between the two is different, the fringe contrast is attenuated. Both SFG and DFG being second-order non-linear processes, their efficiencies strongly depend on the input beam intensities. Therefore, to obtain a high fringe contrast, H5 and H3 should ideally have similar amplitudes. As a first proof of principle of SCORPIO, we choose another BBO (200 μm thick, cut for THG of 800 nm) as our test sample, so that the phase matching angle could be tuned to optimize H5 generation, and thus enhance the fringe visibility.

Figure 7.9c shows the measured spectra in DFG configuration, blocking H3 and H2 from the "sample" BBO with a bandpass filter. H5 is the most intense peak and saturates

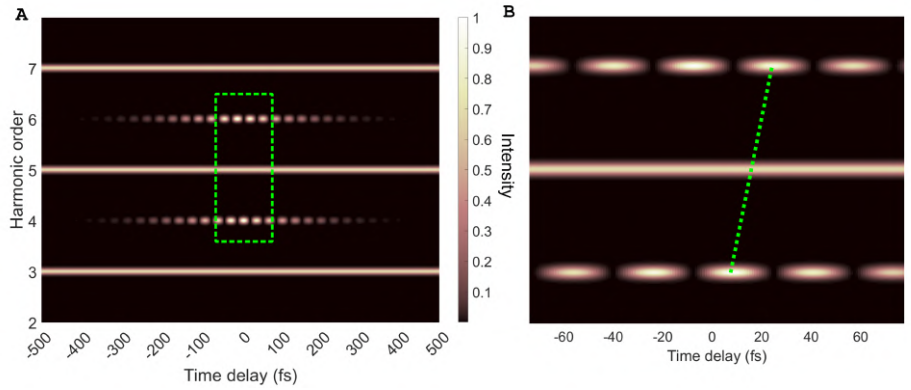


Figure 7.8: a) Simulation of two even harmonic sideband generation $4\omega_0$ and $6\omega_0$ as function of time delay between the NIR fundamental, and the harmonic pulse emitted from a sample. The two pulses have the same duration of 50 fs (FWHM). b) Close up on the dotted area in a) in which the phase offset between the two SB is highlighted.

the spectrometer, while lower yielding H2 and H3 peaks, generated by frequency doubling and tripling of the NIR pulse in the second BBO. The peak for H4 is centered at a wavelength of 492 nm, which is slightly blue-shifted from the expected $4\omega_0$ wavelength of 487.5 nm. In Fig. 7.9d, H4 intensity is integrated over the spectral peak, and plotted as function of time delay (step size of 0.12 µm corresponding to a time resolution of 0.8 fs and a Nyquist frequency of 1.25 fs^{-1}). As expected from equation 7.25, the signal, which should correspond to the convolution of the NIR and H3 envelopes, exhibits a gaussian shape, with no visible interferences. This is a strong indicator that NIR was fully removed from the sample beam, which would otherwise induce ω_0 oscillations due to spectral-interferometry of the two fundamentals.

Fig. 7.9a shows the spectra measured in SFG configuration, filtering out both H2 and H5 by changing the bandpass filter after the "sample" BBO, but keeping all other parameters identical. H3 saturates the spectrometer, and a peak at H5 due to generation from the second crystal can be noticed. The peak for H4 is centered at a wavelength of 496 nm, which is again slightly blue-shifted from the expected $4\omega_0$ wavelength of 487.5 nm. Similarly to DFG results, H4 counts as function of time delay plotted in Fig. 7.9b shows a gaussian profile, with no visible interferences.

Both SFG and DFG traces were fitted to a gaussian function. Considering equations 7.30 and 7.34, the ratio between the duration of the two pulses was estimated to 1.054. A FWHM of 92.78 fs was extracted from the DFG trace and 101.54 fs for the SFG one, yielding a ratio of 1.098, which is in reasonable agreement with the estimate.

After verifying both processes can generate H4 with equivalent intensities, filtering elements are removed from the sample beam path in order to measure both SFG and DFG at the same time. A bandpass filter centered on H4 is placed just before the spectrometer to block other harmonic orders. The spectra measured for the time delay corresponding to the expected maximum overlap of the two pulses is plotted in Fig. 7.9e. The most pronounced peak corresponds to H4, and H3 counts remaining after the bandpass filter

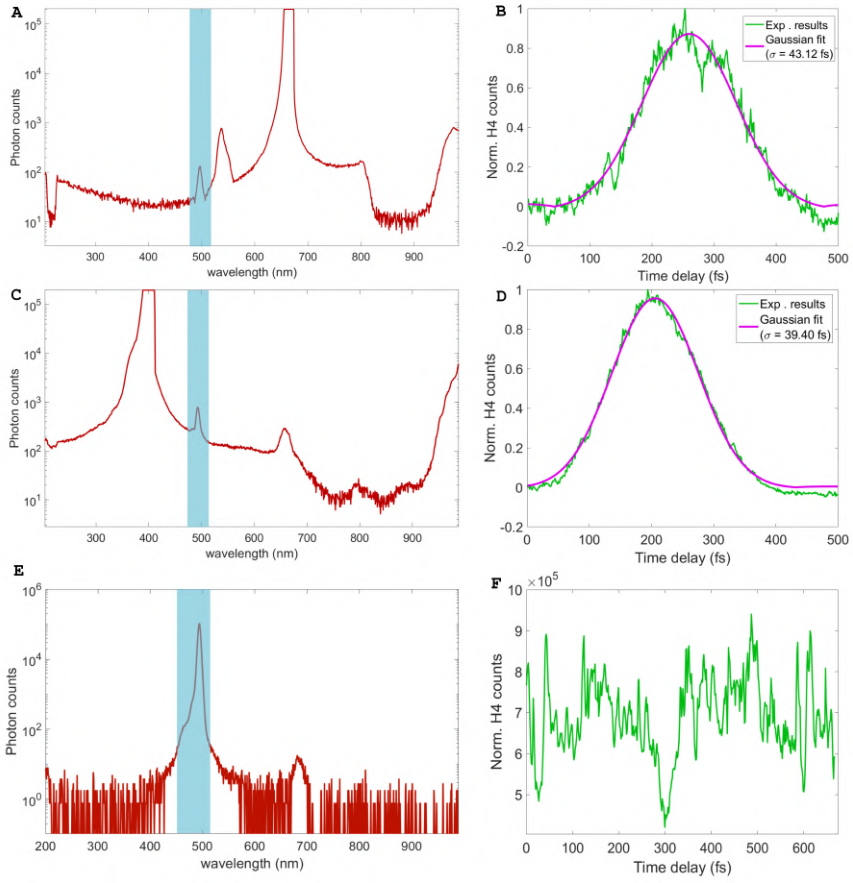


Figure 7.9: SFG and DFG time delay traces. Harmonics are generated from a first BBO crystal and focused with a time-delayed beam at the fundamental frequency in a second BBO. The experimental conditions are the same between each plots and only the bandpass filters used for isolating harmonics are changed. The blue bands indicates the bandwidth over which integration was done in the time delay plots. a) Spectra in SFG configuration, where a bandpass filter centered on the third harmonic is placed after the first BBO. b) Normalized H4 counts as function of time delay in SFG configuration. c) Spectra in DFG configuration, where a bandpass filter centered on the fifth harmonic is placed after the first BBO. d) Normalized H4 counts as function of time delay in DFG configuration. e) Spectra in SFG+DFG configuration, where filters are removed from the beam path in-between the two BBO crystals, and a bandpass filter centered and fourth harmonic is placed before the fiber spectrometer. f) Normalized H4 counts as function of time delay in SFG+DFG configuration.

are also present. H4 counts as function of time delay are plotted in Fig. 7.9f. No gaussian envelope can be identified, nor clear signs of oscillations. We attribute this result to the remaining H4 light emitted from the first BBO crystal, whose fluctuations mask the interferometric contribution generated in the second BBO crystal. A way to get around this issue would be to use a centro-symetric material which does not emit even harmonics as our test sample. However, the conversion efficiency obtained from a BBO crystal is

difficult to be matched with other dielectrics materials, which is not ideal as a first proof of principle experiment. Therefore, upcoming experiments are planned using a higher repetition rate laser in order to obtain stronger harmonic yields.

7.4 CONCLUSION

We have presented some first proof of principle results of the SCORPIO technique, which aims at a full characterization of the electrical field generated via SHHG. We could show that efficient SFG and DFG using harmonics generated in a BBO crystal could be obtained in the same experimental conditions, thus proving SB oscillations are within reach if a higher signal-to-noise ratio is achieved. Further work will aim at repeating this experiment using a higher repetition laser system in order to improve the fringes visibility at this particular SB, but also investigate higher orders in order to recover meaningful phase differences which could be used for determining harmonic emission on a subcycle timescale.

Potential applications are numerous. Investigation of quantum materials is one of them, since resolving subcycle changes in harmonic emission could be used to probe ultrafast changes of the dielectric function, which can provide insights on the material electronic and structural dynamics with unprecedented time resolution.

8

NON-LINEAR PUMP-PROBE DIGITAL HOLOGRAPHY FOR TRACKING THE ULTRAFAST PHASE TRANSITION IN NIOBIUM DIOXIDE

This final chapter aims at measuring the transient phase and amplitude of third harmonic emitted from NbO_2 using DHM, while exciting the material with a second source to trigger an insulator-to-metal transition. We report some transient phase change of more than one radian, which are shown to be uncorrelated from the phase of the fundamental. A model accounting for the effect of bandgap shrinkage on the dipole phase of the third harmonic is introduced to explain these results.

8.1 INTRODUCTION

How fast transient phases emerging from photoexcitation of quantum materials may be, they are not instantaneous, and a progressive nucleation process should be observable, with a distribution of coexisting heterogeneous phases in the material. Although these transitions are being studied for decades, a proper in-situ characterization of dynamic domain formation is still very hard to achieve, as both a spatial resolution down to the nanoscale and a femtosecond time resolution are needed at once, making experimental implementation extremely challenging.

Recent work has shown some success in this endeavor. In the paper by Johnson et al. [64], coherent X-ray imaging was used to reveal the ultrafast metallization of VO_2. The work insisted on the importance of the initial spatial heterogenity of the material, with preexisting domains being more favorable to undergo the phase transition. Danz et al. have reported ultrafast transmission electron microscopy measurements on the transition metal dichalcogenide $1T-TaS_2$ [171]. Kim et al. used energy-resolved transmission electron microscopy to unveil ultrafast formation of domains in VO_2 [172].

With this last chapter, we aim at combining experiments carried in chapter 4 and 6, i.e. to achieve a pump-probe DHM measurement on NbO_2 to create a movie of the transient phase and amplitude of the third harmonic, in order to track dynamic band structure changes during an insulator-to-metal transition. The goal of this experiment is not to resolve the formation of domains, which are supposedly much smaller than the achievable resolution of the optical system, but rather to measure how the overall phase distribution is affected, as illustrated by Fig.8.1.

8.2 METHODS

Figure 8.2 presents the experimental setup. Similarly to the static measurement presented in chapter 4, the OPA idler output (central wavelength of 1980 nm ; duration of around 50 fs) is split in two. One beam path is focused to the sample using a lens of 5 cm focal length, and an image of the third harmonic reflection is produced on the camera using a two-lens microscope. The other beam path is used to generate a reference TH wave inside a BBO crystal for recombination with the first beam on the camera, where the hologram is formed. Time delay between the two pulses is controlled manually via a linear delay stage, and optimized to obtain an interference pattern in the desired area of the TH image. For pumping, a leftover 800 nm output of the OPA is time-delayed using a linear delay stage (*CLS-9292* from *Smaract*) with an accuracy close to 1 nm, and focused on the sample by the same lens used for imaging. The objective utilized for the static measurement is replaced by a 1 inch lens with a focal length of 2.5 cm to facilitate focusing of both the pump and probe beams simultaneously. In this geometry, the probe beam spot on the sample is larger than the pump, which allows to use the un-pumped areas as an in-situ reference from which we can appreciate the phase difference with pumped areas. The $1/e^2$ diameter of the pump beam on the sample is around 50 µm, whereas the probe diameter is in the hundreds of microns range (the sample is placed slightly before the focus of the probe beam to obtain a larger illumination). A shutter, installed in the pump beam bath, allows to rapidly alternate between pump-on and pump-off hologram acquisition.

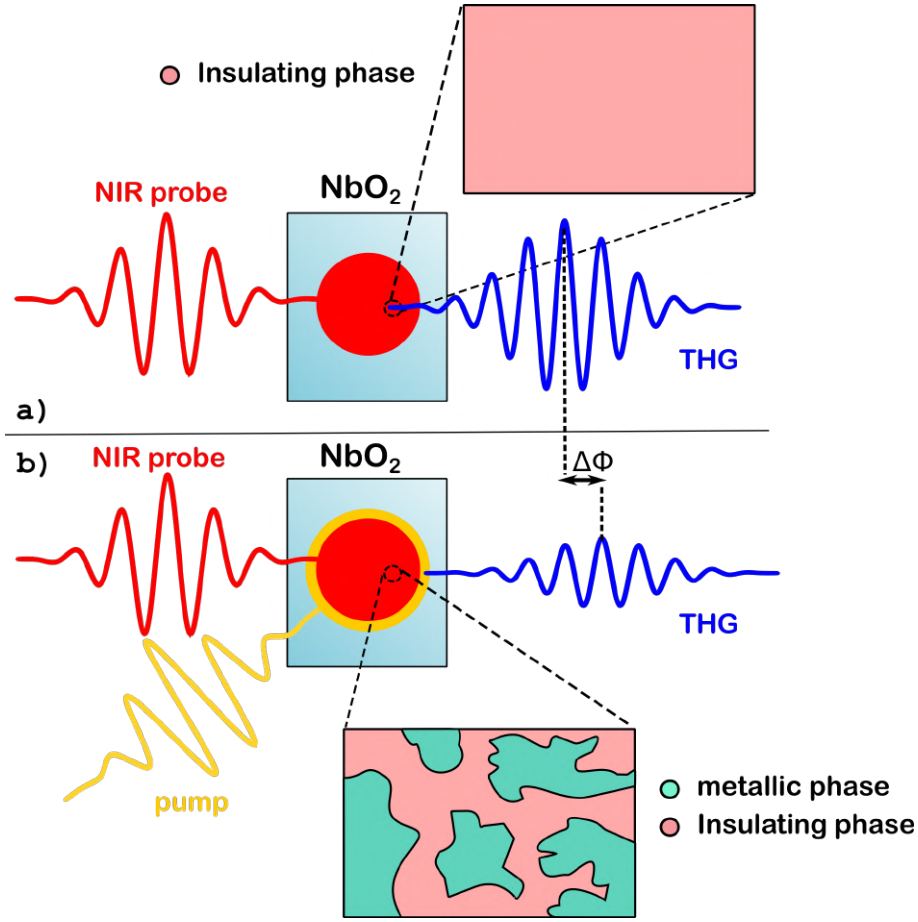


Figure 8.1: Schematic of the pump-probe THG holography measurement. In a), the NIR fundamental is focused on the sample to generate harmonic, while in b) a pump pulse is added. In the latter case, the pump-induced phase transition gives rise to the formation of metallic and insulating phase domain with subwavelength dimensions. The generated third harmonic emitted in both case varies in both amplitude and phase.

The hologram reconstruction procedure differs from the static case. For each time delay, two holograms are acquired: one with the pump shutter opened, and one closed. As displayed in Fig. 8.3a, and Fig. 8.3b, the pumped area appears as a darker round spot, highlighted by the insets. A Fourier transform is applied to both holograms, the convolution term is isolated, and an inverse Fourier transform is performed to recover both an amplitude and phase reconstruction (Fig. 8.3c-f).

In the static measurement presented in chapter 4, an hologram of a flat area close to the pattern of interest was used to remove phase contributions resulting from the illumination field, so that phase changes induced by the nanostructure could be isolated. In the present experiment, the pump-off phase reconstruction is subtracted from the pump-on one in order to isolate effects of the pump on the TH wavefront. An example of

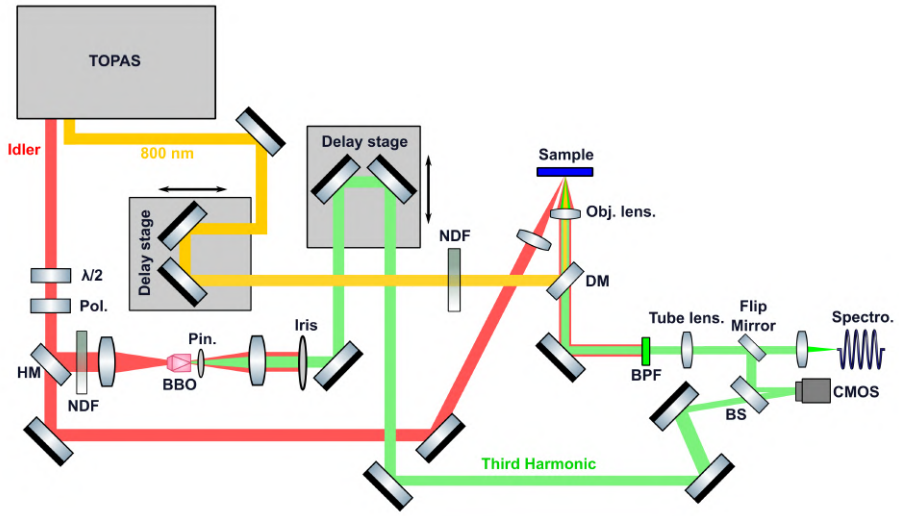


Figure 8.2: The OPA output goes through both a half-waveplate ($\lambda/2$) and a thin film polarizer (Pol.) in order to adjust power and polarization. A holey mirror (HM) is used to split the beam in two. The reflected beam, shaped as a donut in the far field, passes through an neutral density filter (NDF) in order to tune its relative intensity with respect to the other arm. It is focused in a BBO where harmonic generation takes place. A 200 μm diameter pinhole (Pin.) is placed just after the BBO in order to clean up the beam profile in the far-field. The donut-shaped NIR fundamental is filtered out using a partially closed iris while letting the third harmonic pass. The beam passes through a delay stage to adjust the time overlap of the two arms. Finally, the beam is sent to the CMOS detector through transmission of a beamsplitter (BS). The second beam path, transmitted from the holey mirror, is focused on the sample using a 5 cm focal length lens, at an incidence angle of around 35 degrees. The reflected TH is collected by an objective lens coupled to a tube lens, and imaged on the CMOS detector. The 800 nm leftover pump output from the OPA is time-delayed using a linear stage, and focused on the sample using the imaging lens. Power is tuned using a ND wheel filter. A bandpass filter (BPF) is placed in-between the two lenses of the microscope to filter out the remaining fundamental and pump light.

phase reconstruction after pump-off subtraction is displayed in Fig.8.3h. We can observe a uniform phase distribution for unpumped areas, surrounded by a speckle pattern formed by the random values set to areas out of the temporal overlap of the imaging and reference beams, and a well-localized gaussian-like spot for the pump. In order to create a movie of the phase distribution as function of time delay, a small un-pumped area of ten by ten pixels is set to a fixed phase value of zero to better appreciate the continuity from one frame to the next.

By subtracting Fig. 8.3c and Fig. 8.3d, the relative amplitude distribution is obtained as shown in Fig. 8.3g. We can clearly identify a spot corresponding to a localized decrease of harmonic generation. The surrounding area have a value of zero, therefore indicating that they are unaffected by the pump. Similarly to the phase distribution, areas outside the limits of the temporal overlap display random values carrying no information.

There is two possible way to plot the transient change in TH amplitude. The first one is to compare the signal difference between pumped area with shutter on, and shutter off, as was just described. A second way, is to define the reference spatially, by comparing signals from the pumped area with an unpumped area, acquired simultaneously by the camera.

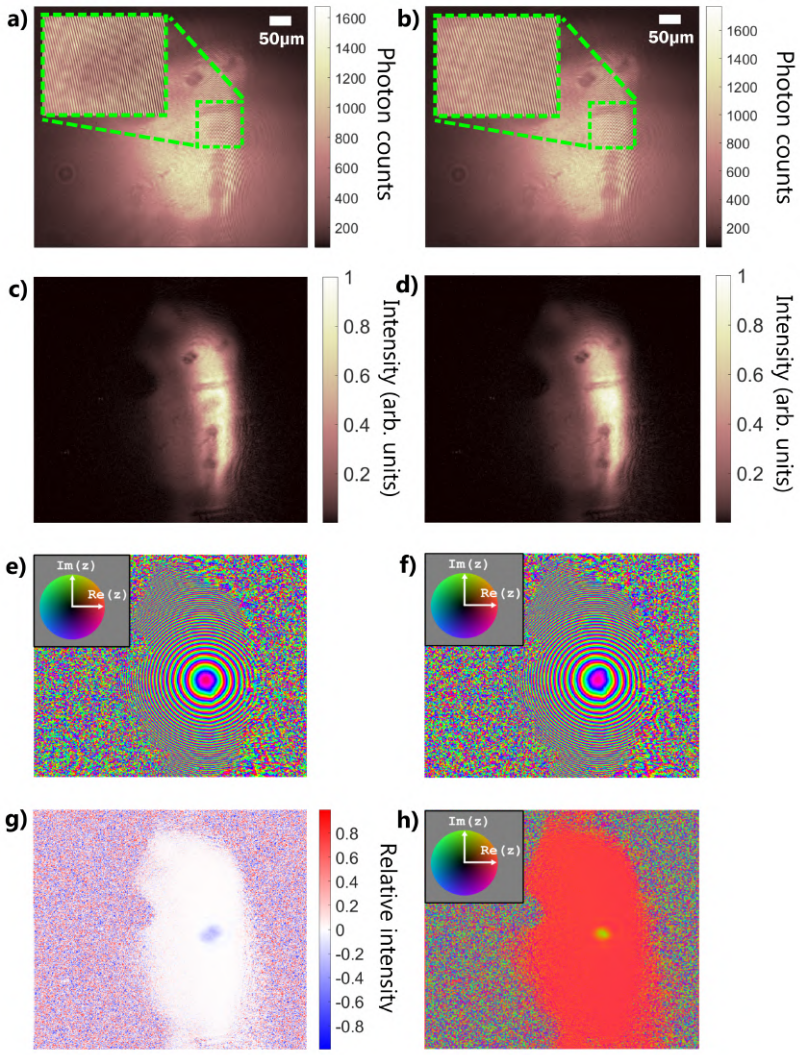


Figure 8.3: Reconstruction procedure of pump-probe DHM measurements. The pump fluence on the sample is 12 mJ/cm^2, the probe is around 5 mJ/cm^2, and the time delay is set to the value providing maximum change in both phase and amplitude. a) Hologram recorded with pump on. b) Hologram recorded with pump off. The insets highlights the pumped area, visible as a darker round area in a). c) Amplitude reconstruction with pump on. d) Amplitude reconstruction with pump off. e) Phase reconstruction with pump on. f) Phase reconstruction with pump off. g) Relative amplitude change between c) and d). h) Phase subtraction between e) and f).

This second approach has a great advantage in terms of noise reduction. Indeed, because the reference signal is measured at the same time as the pump one, noise contributions resulting from intensity fluctuations of the laser from one hologram acquisition to the

next are canceled out. Since the illumination of the beam is not homogeneous, we first need to define a baseline ratio R_0, averaged over multiple images acquired before time zero [11, 173]:

$$R_0 = \langle \frac{S_p(t)}{S_u(t)} \rangle_{t<0} \tag{8.1}$$

where $S_p(t)$ is the mean intensity of the pumped area, averaged over a small box of a few pixels and $S_u(t)$ is the mean intensity of the unpumped area, also averaged on multiple pixels. We then define a corrected pump signal so that:

$$S_p^{corr}(t) = \frac{S_p(t)}{R_0} \tag{8.2}$$

The transient change is then calculated using:

$$\frac{\Delta S(t)}{S_u(t)} = \frac{S_p(t)^{corr} - S_u(t)}{S_u(t)} \tag{8.3}$$

Two NbO_2 samples were used: a first one is a polycrystalline thin film of 115 nm grown by reactive bias target ion beam deposition, and the second one is a crystalline thin film of 20 nm which was grown on a sapphire substrate via pulsed-laser deposition. The miller index of the surface is (100), corresponding to an a-axis normal to the surface, with b and c-axis lying in the surface plane.

8.3 RESULTS

A first measurement, performed on the polycrystalline film, consists in recording holograms sequentially at every time delay, for a few pump powers. The fluence of the OPA output driving HHG was kept at a constant value of around mJ/cm^2. Figure 8.4 shows the relative phase and relative amplitude reconstructions for selected time delays, at a pump fluence of 12 mJ/cm^2. For both phase and amplitude, no spot is visible before time zero, indicating that no permanent degradation has occurred.

In Fig. 8.6, the relative phase and amplitude, integrated over a few pixels located at the pump spot are plotted as function of time delay. The harmonic yield drops very quickly at time zero, and then recovers at a slower pace, in a very similar manner to the transient traces presented in chapter 6. A very large phase shift of more than a radian is measured at time zero, and coincides exactly with the maximum decrease in TH. The recovery of the phase to its original value shows almost identical dynamics than the amplitude, and reveals clear relationship between the two. Both spatial (Fig. 8.6b) and temporal (Fig. 8.6a) referencing are used for plotting the relative amplitude change. The spatial referencing leads to a much smoother and noise-free curve, demonstrating the advantage of actually imaging the sample in this pump-probe experiment.

In a second measurement, the time delay is fixed at specific values, and holograms are recorded for multiple pump powers in a row. Because the phase of harmonics is partially inherited from its fundamental driver, it is crucial for interpreting our results to measure how the fundamental is affected by the pump. Therefore, hologram acquisition of both TH and NIR fundamental is performed, keeping the experimental setup identical, and only

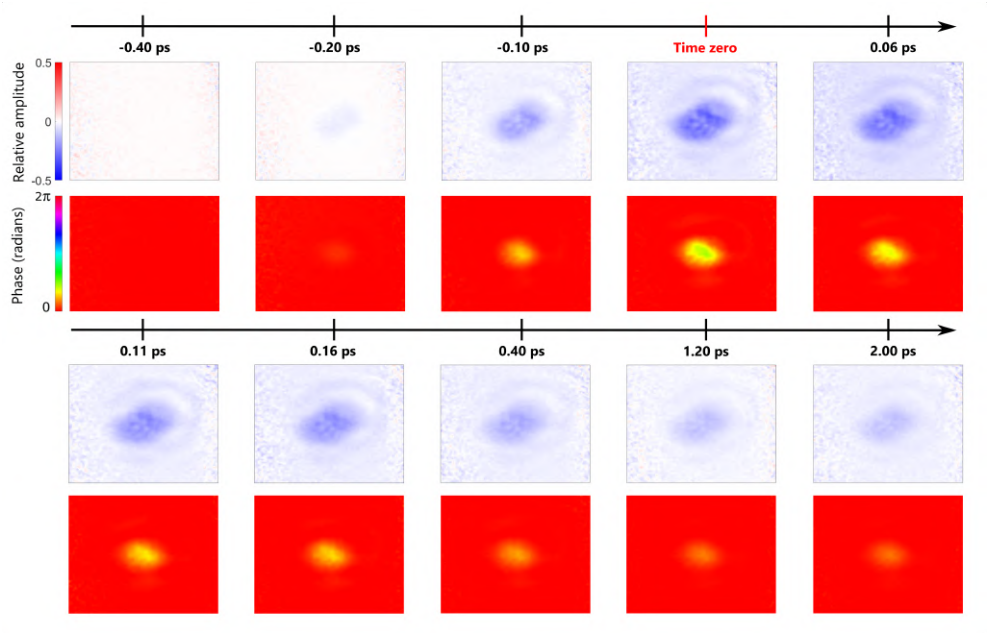


Figure 8.4: Third harmonic phase and relative amplitude reconstructions for multiple time delays, at a pump fluence of 12 mJ/cm^2

changing the filter positioned before the camera. Figure 8.5 displays amplitude and phase reconstruction of the fundamental for selected time delays (pump fluence of 34 mJ/cm^2), showing a slight increase in reflection after time zero, and no visible changes for the phase. Figures 8.7 show plots of the maximum phase and amplitude change (around time zero) for both third harmonic and fundamental. The amplitude of the driving wavelength signal increases with pump power, reaching a maximum enhancement of around 20% relative to the unpumped signal. This behavior can be explained by the pump-induced creation of free carriers, which increase the Drude response of the material in the NIR range, i.e. the pulse interacts strongly with excited carriers, therefore screening its propagation, and boosting reflectivity. This enhancement is higher along the a-axis compared to c-axis, which could partially explain why the TH signal gets more depleted along a-axis. Indeed, a higher reflection of the fundamental also implies a lower harmonic yield emitted from the sample. For both c and a axis, the TH depletion saturates when reaching higher fluence values, similarly to the results reported in chapter 6, which involved depletion of the signal due to decoherence through electron-electron scattering.

The phase of the fundamental only changes by a few tens of miliradians for both axis, and therefore cannot explain the phase shift of the third harmonic, which is orders of magnitude higher. For both axis, the phase difference reaches the same saturation threshold at high pump fluences. This indicates that the TH phase does not simply follow an inversely proportional relationship with amplitude decrease, since the relative amplitude along the two axis does not reach the same level of depletion.

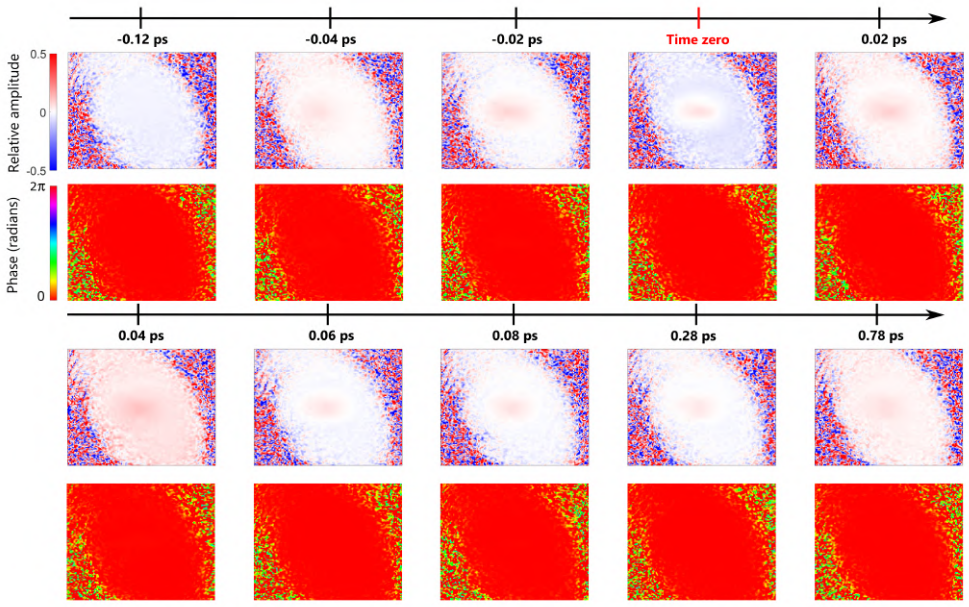


Figure 8.5: Fundamental phase and relative amplitude reconstructions for multiple time delays, at a pump fluence of 34 mJ/cm^2

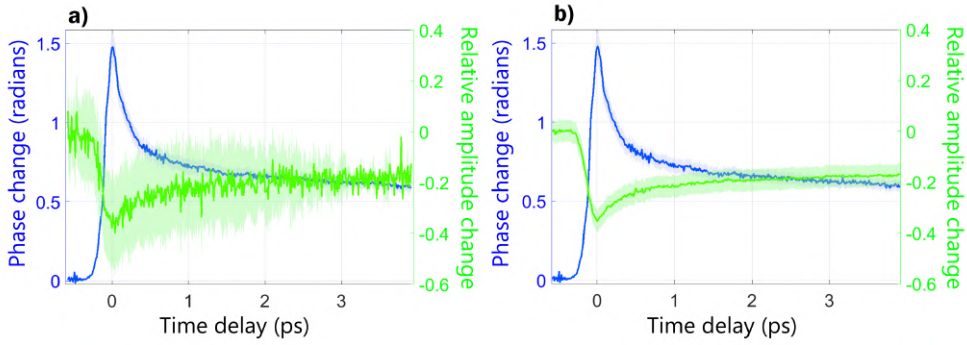


Figure 8.6: Transient third harmonic phase and amplitude as function of time delay for a pump power of 28 mJ/cm^2. The phase is represented in dark blue in both plots, with error bars shown in light blue. In a) the temporal referencing is used for calculating the relative amplitude change (dark green with error bars in light green), whereas the spatial referencing is used in b).

A possible way to interpret these results is to consider how dynamical band structure changes induced by excited carriers can influence the phase of generated harmonics, and to conclude if this mechanism is enough to explain the observable phase shift, or if another cause needs to be invoked, i.e. a phase transition from an insulating to metallic state. As detailed in the theoretical framework section, interband harmonic generation

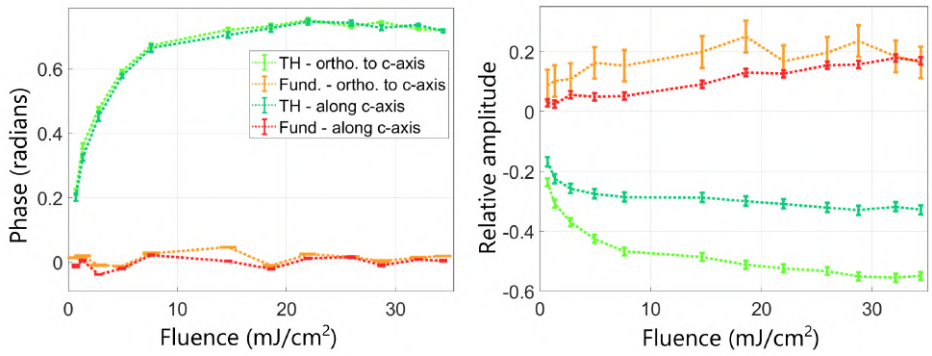


Figure 8.7: a) Relative phase change between pumped and unpumped area for both fundamental and TH, along both c-axis and a-axis, at time zero. b) Relative amplitude change (equation 8.3) between pumped and unpumped area for both fundamental and TH, along both c-axis and a-axis. Fluence of the idler field driving HHG was kept at a constant value of around 5 mJ/cm^2

originates from the recombination of an excited electron to the valence band after it has been accelerated by the driving field in the conduction band. The semi-classical action associated to the electron can be expressed as [107]:

$$S(t_r) = \int_{t_i}^{tr} \Delta\epsilon(k(\tau))d\tau \tag{8.4}$$

In which t_i is the time of excitation from the valence to the conduction band, t_r is the time of recombination between the hole and the electron, and $\Delta\epsilon(k(\tau))$ is the difference in energy at the instant of recombination. The dipole phase characterizing the emitted harmonic can be derived from the semi-classical action using:

$$\phi = N\left(\omega_0 t_r + \frac{\pi}{2}\right) - S(t_r) \tag{8.5}$$

in which ω_0 is the fundamental frequency. If we consider relatively small bandgap variations, we can assume that the phase difference can be approximated by:

$$\Delta\phi \approx -\Delta E_g \Delta t \tag{8.6}$$

Where Δt is the time difference between ionization and recombination, $t_r - t_i$, and ΔE_g is the change in bandgap energy. In the paper from de Keijzer et al.[106], an excursion time of 0.30 fs is theoretically derived for the third harmonic by solving semi-conductor Bloch equations. Assuming this reported time is of the same order as for our specific case (band structure, wavelength, intensity), and inject this value into equation 8.6, as well as the saturation phase difference of 0.75 radians extracted from Fig. 8.7b, a bandgap shift of 0.61 eV is obtained. This value is very close to the indirect bandgap of NbO_2 (0.7 eV) and possibly indicates that the material has indeed reach a metallic state. The fact that the value of 0.7 eV is not reached could be explained by the fact that not all the pumped area has actually undergone a phase transition, and therefore decrease the value of the averaged phase difference measured from the hologram.

8.4 CONCLUSION

We have demonstrated some first experimental results of pump-probe digital holography using harmonic generated from solids. This method could allow to probe the transient phase and amplitude of the third harmonic emitted in reflection from a NbO_2 sample during photo-excitation by a time-delayed pump. A large phase shift of the third harmonic wavefront could be measured upon photo-excitation of NbO_2, uncorrelated from the phase of the fundamental, and which could be linked to the carrier-induced dynamic modification of the band structure. These results pave the way towards using the phase recovered from harmonic holography as an ultrafast probe of phase transition in quantum materials.

BIBLIOGRAPHY

REFERENCES

[1] J Bardeen and WH Brattain. The transistor, a semi-conductor triode. *Physical review*, 74(2):230, 1948.

[2] TH Maiman. Stimulated optical radiation in ruby. *Nature*, 187(4736):493–494, 1960.

[3] Donna Strickland and Gerard Mourou. Compression of amplified chirped optical pulses. *Optics communications*, 55(6):447–449, 1985.

[4] N Bohr. I. on the constitution of atoms and molecules. *The London, Edinburgh, and Dublin Philosophical Magazine and Journal of Science*, 26(151):1–25, 1913.

[5] M Ferray, A L'Huillier, XF Li, LA Lompre, G Mainfray, and C Manus. Multiple-harmonic conversion of 1064 nm radiation in rare gases. *Journal of Physics B: Atomic, Molecular and Optical Physics*, 21(3):L31, 1988.

[6] A McPherson, G Gibson, H Jara, U Johann, TS Luk, IA McIntyre, Keith Boyer, and CK Rhodes. Studies of multiphoton production of vacuum-ultraviolet radiation in the rare gases. *Journal of the Optical Society of America B*, 4(4):595–601, 1987.

[7] S Ghimire, AD DiChiara, E Sistrunk, P Agostini, LF DiMauro, and DA Reis. Observation of high-order harmonic generation in a bulk crystal. *Nature physics*, 7(2):138–141, 2011.

[8] G Vampa, TJ Hammond, N Thiré, BE Schmidt, F Légaré, CR McDonald, T Brabec, DD Klug, and PB Corkum. All-optical reconstruction of crystal band structure. *Physical Review Letters*, 115(19):193603, 2015.

[9] M Kira and SW Koch. *Semiconductor quantum optics*. Cambridge University Press, 2011.

[10] D Golde, T Meier, and SW Koch. High harmonics generated in semiconductor nanostructures by the coupled dynamics of optical inter-and intraband excitations. *Physical Review B — Condensed Matter and Materials Physics*, 77(7):075330, 2008.

[11] G Vampa, CR McDonald, G Orlando, DD Klug, PB Corkum, and T Brabec. Theoretical analysis of high-harmonic generation in solids. *Physical review letters*, 113(7):073901, 2014.

[12] GG Brown, A Jiménez-Galán, REF Silva, and M Ivanov. Real-space perspective on dephasing in solid-state high harmonic generation. *Physical Review Research*, 6(4):043005, 2024.

[13] MR Bionta, E Haddad, A Leblanc, V Gruson, P Lassonde, H Ibrahim, J Chaillou, N Émond, MR Otto, A Jiménez-Galán, et al. Tracking ultrafast solid-state dynamics using high harmonic spectroscopy. *Physical Review Research*, 3(2):023250, 2021.

[14] PJ van Essen, Z Nie, B de Keijzer, and PM Kraus. Toward complete all-optical intensity modulation of high-harmonic generation from solids. *ACS photonics*, 11(5):1832–1843, 2024.

[15] MLS van der Geest, JJ de Boer, K Murzyn, P Jurgens, B Ehrler, and PM Kraus. Transient high-harmonic spectroscopy in an inorganic–organic lead halide perovskite. *The Journal of Physical Chemistry Letters*, 14(48):10810–10818, 2023.

[16] M Garg, M Zhan, TT Luu, H Lakhotia, T Klostermann, A Guggenmos, and E Goulielmakis. Multi-petahertz electronic metrology. *Nature*, 538(7625):359–363, 2016.

[17] M Hohenleutner, F Langer, O Schubert, M Knorr, U Huttner, SW Koch, M Kira, and R Huber. Real-time observation of interfering crystal electrons in high-harmonic generation. *Nature*, 523:572–575, 2015.

[18] J Park, A Subramani, S Kim, and MF Ciappina. Recent trends in high-order harmonic generation in solids. *Advances in Physics: X*, 7(1):2003244, 2022.

[19] JW Goodman. *Introduction to Fourier optics*. Roberts and Company publishers, 2005.

[20] D Gabor, GW Stroke, D Brumm, A Funkhouser, and A Labeyrie. Reconstruction of phase objects by holography. *Nature*, 208(5016):1159–1162, 1965.

[21] LP Yaroslavskii and NS Merzlyakov. *Methods of digital holography*. Springer, 1980.

[22] D Gauthier, M Guizar-Sicairos, X Ge, W Boutu, B Carré, JR Fienup, and H Merdji. Single-shot femtosecond x-ray holography using extended references. *Physical Review Letters*, 105(9), 2010.

[23] N Bukin. *Time-resolved imaging of magnetisation dynamics using x-ray holography with extended reference and autocorrelation by linear differential operator (HERALDO)*. University of Exeter (United Kingdom), 2018.

[24] S Mustafi and T Latychevskaia. Fourier transform holography: A lensless imaging technique, its principles and applications. *Photonics*, 10(2):153, 2023.

[25] J Geilhufe, B Pfau, CM Günther, M Schneider, and S Eisebitt. Achieving diffraction-limited resolution in soft-x-ray fourier-transform holography. *Ultramicroscopy*, 214:113005, 2020.

[26] S Paschen, T Lühmann, S Wirth, P Gegenwart, O Trovarelli, C Geibel, F Steglich, P Coleman, and Q Si. Lensless imaging of magnetic nanostructures by x-ray spectroholography. *Nature*, 432(7019):881–885, 2004.

[27] CM Günther, B Pfau, R Mitzner, B Siemer, S Roling, H Zacharias, O Kutz, I Rudolph, D Schondelmaier, R Treusch, and S Eisebitt. Sequential femtosecond x-ray imaging. *Nature Photonics*, 5:99–102, 2 2011.

[28] PA Franken, AE Hill, CW Peters, and G Weinreich. Generation of optical harmonics. *Physical review letters*, 7(4):118, 1961.

[29] RW Boyd. *Nonlinear Optics*. Academic Press, 4 edition, 2020.

[30] PM Paul, ES Toma, P Breger, G Mullot, F Augé, P Balcou, Muller HG, and P Agostini. Observation of a train of attosecond pulses from high harmonic generation. *Science*, 292(5522):1689–1692, 2001.

[31] M Hentschel, R Kienberger, C Spielmann, GA Reider, N Milosevic, T Brabec, P Corkum, U Heinzmann, M Drescher, and F Krausz. Attosecond metrology. *Nature*, 414(6863):792–794, 2001.

[32] F Krausz and M Ivanov. Attosecond physics. *Reviews of modern physics*, 81(1):163–234, 2009.

[33] LV Keldysh. Ionization in the field of a strong electromagnetic wave. In *Selected Papers of Leonid V Keldysh*, pages 56–63. World Scientific, 2024.

[34] PB Corkum. Plasma perspective on strong field multiphoton ionization. *Physical review letters*, 71(13):1994, 1993.

[35] EN Osika, A Chacón, L Ortmann, N Suárez, JA Pérez-Hernández, B Szafran, MF Ciappina, F Sols, AS Landsman, and M Lewenstein. Wannier-bloch approach to localization in high-harmonics generation in solids. *Physical Review X*, 7(2):021017, 2017.

[36] TT Luu, M Garg, SY Kruchinin, A Moulet, MT Hassan, and E Goulielmakis. Extreme ultraviolet high-harmonic spectroscopy of solids. *Nature*, 521(7553):498–502, 5 2015.

[37] S Feng and HG Winful. Physical origin of the gouy phase shift. *Optics letters*, 26(8):485–487, 2001.

[38] R Righini. Ultrafast optical kerr effect in liquids and solids. *Science*, 262(5138):1386–1390, 1993.

[39] SDC Roscam Abbing, N Kuzkova, R van der Linden, F Campi, B de Keijzer, C Morice, Z Zhang, MLS van der Geest, and PM Kraus. Enhancing the efficiency of high-order harmonics with two-color non-collinear wave mixing in silica. *Nature Communications*, 15(1):8335, 2024.

[40] SDC Roscam Abbing, F Campi, A Zeltsi, P Smorenburg, and PM Kraus. Divergence and efficiency optimization in polarization-controlled two-color high-harmonic generation. *Scientific Reports*, 11(1):24253, 2021.

[41] AJ Uzan-Narovlansky, A Jiménez-Galán, G Orenstein, REF Silva, T Arusi-Parpar, S Shames, D Bruner, B Yan, O Smirnova, M Ivanov, et al. Observation of light-driven band structure via multiband high-harmonic spectroscopy. *Nature photonics*, 16(6):428–432, 2022.

[42] S Ghimire and DA Reis. High-harmonic generation from solids. *Nature Physics*, 15(1):10–16, 2019.

[43] E Goulielmakis and T Brabec. High-harmonic generation in condensed matter. *Nature Photonics*, 16(6):411–421, 2022.

[44] A Jiménez-Galán, C Bossaer, G Ernotte, AM Parks, REF Silva, DM Villeneuve, A Staudte, T Brabec, A Luican-Mayer, and G Vampa. Orbital perspective on high-harmonic generation from solids. *Nature Communications*, 14(1):8421, 2023.

[45] N Klemke, N Tancogne-Dejean, GM Rossi, Y Yang, F Scheiba, RE Mainz, G Di Sciacca, A Rubio, FX Kärtner, and OD Mücke. Polarization-state-resolved high-harmonic spectroscopy of solids. *Nature communications*, 10(1):1319, 2019.

[46] J Lu, EF Cunningham, YS You, DA Reis, and S Ghimire. Interferometry of dipole phase in high harmonics from solids. *Nature Photonics*, 13(2):96–100, 2019.

[47] Nataliia Kuzkova, Pieter J van Essen, Roy van der Linden, Brian de Keijzer, Rui EF Silva, Álvaro Jiménez Galán, and Peter M Kraus. Attosecond high-harmonic interferometry probes orbital-and band-dependent dipole phase in magnesium oxide. *Science Advances*, 12(18):eaeb4109, 2026.

[48] REF Silva, Á Jiménez-Galán, B Amorim, O Smirnova, and M Ivanov. Topological strong-field physics on sub-laser-cycle timescale. *Nature Photonics*, 13(12):849–854, 2019.

[49] I Tyulnev, L Zhang, L Vamos, J Poborska, U Bhattacharya, RW Chhajlany, T Grass, S Mañas-Valero, E Coronado, M Lewenstein, and J Biegert. High harmonic spectroscopy reveals anisotropy of the mott to charge-density-wave phase transition in $TiSe_2$. *arXiv preprint arXiv:2409.04216*, 2024.

[50] PM Kraus and HJ Wörner. Time-resolved high-harmonic spectroscopy of valence electron dynamics. *Chemical Physics*, 414:32–44, 2013.

[51] E Morosan, D Natelson, AH Nevidomskyy, and Q Si. Strongly correlated materials. *Advanced Materials*, 24(36):4896–4923, 2012.

[52] NF Mott. Metal-insulator transition. *Reviews of Modern Physics*, 40(4):677, 1968.

[53] R Peierls. The size of a dislocation. *Proceedings of the Physical Society*, 52(1):34, 1940.

[54] HM Yamamoto. Phase-transition devices based on organic mott insulators. *Bulletin of the Chemical Society of Japan*, 94:2505–2539, 2021.

[55] H Liu, J Lu, and XR Wang. Metamaterials based on the phase transition of VO_2. *Nanotechnology*, 29(2):024002, 2017.

[56] D Wegkamp and J Stähler. Ultrafast dynamics during the photoinduced phase transition in VO_2. *Progress in Surface Science*, 90(4):464–502, 2015.

[57] G Mirbagheri, DT Crouse, and C Tan. Recent advance in phase transition of vanadium oxide based solar reflectors and the fabrication progress. In *Physics and Simulation of Optoelectronic Devices XXX*, volume 11995, pages 181–191. SPIE, 2022.

[58] Z He and AJ Millis. Photoinduced phase transitions in narrow-gap mott insulators: The case of VO_2. *Physical Review B - Condensed Matter and Material Physics*, 93(11):115126, 2016.

[59] A Cavalleri, T Dekorsy, H Chong, JC Kieffer, and RW Schoenlein. Evidence for a structurally-driven insulator-to-metal transition in vo 2: A view from the ultrafast timescale. *Physical Review B - Condensed Matter and Materials Physics*, 70(16):1–4, 2004.

[60] AA Gavdush, VA Zhelnov, KB Dolganov, AA Bogutskii, SV Garnov, MG Burdanova, DS Ponomarev, Q Shi, KI Zaytsev, and GA Komandin. Insulator–metal transition in $mathrmVO_2$ film on sapphire studied by broadband dielectric spectroscopy. *Scientific Reports*, 15(1), 2025.

[61] MF Jager, C Ott, PM Kraus, CJ Kaplan, W Pouse, RE Marvel, RF Haglund, DM Neumark, and SR Leone. Tracking the insulator-to-metal phase transition in vo2 with few-femtosecond extreme uv transient absorption spectroscopy. *Proceedings of the National Academy of Sciences of the United States of America*, 114(36):9558–9563, 2017.

[62] HT Kim, BG Chae, DH Youn, SL Maeng, G Kim, KY Kang, and YS Lim. Mechanism and observation of mott transition in vo2-based two- and three-terminal devices. *New Journal of Physics*, 6(1), 2004.

[63] AS Johnson, J Valls Conesa, L Vidas, D Perez-Salinas, CM Günther, B Pfau, KA Hallman, RF Haglund Jr, S Eisebitt, and S Wall. Quantitative hyperspectral coherent diffractive imaging spectroscopy of a solid-state phase transition in vanadium dioxide. *Science Advances*, 7(33):eabf1386, 2021.

[64] AS Johnson, D Perez-Salinas, KM Siddiqui, S Kim, S Choi, K Volckaert, PE Majchrzak, S Ulstrup, N Agarm, K Hallman, RF Haglund, CM Günther, B Pfau, S Eisebitt, D Backes, F Maccherozzi, A Fitzpatrick, SS Dhesi, P Gargiani, M Valvidares, N Artrith, F de Groot, H Choi, D Jang, A Katoch, S Kwon, SH Park, H Kim, and SE Wall. Ultrafast x-ray imaging of the light-induced phase transition in vo2. *Nature Physics*, 19(2):215–220, 2023.

[65] GI Petrov, VV Yakovlev, and JA Squier. Nonlinear optical microscopy analysis of ultrafast phase transformation in vanadium dioxide. *Optics Letters*, 27(8):655–657, 2002.

[66] Y Murakami, M Eckstein, and P Werner. High-harmonic generation in mott insulators. *Physical Review Letters*, 121(5):057405, 2018.

[67] O Grånäs, I Vaskivskyi, X Wang, P Thunström, S Ghimire, R Knut, J Söderström, L Kjellsson, D Turenne, RY Engel, M Beye, J Lu, DJ Higley, AH Reid, W Schlotter, G Coslovich, M Hoffmann, G Kolesov, C Schüßler-Langeheine, A Styervoyedov, N Tancogne-Dejean, MA Sentef, DA Reis, A Rubio, SSP Parkin, O Karis, JE Rubensson, O Eriksson, and HA Dürr. Ultrafast modification of the electronic structure of a correlated insulator. *Physical Review Research*, 4(3):L032030, 2022.

[68] C Heide, Y Kobayashi, AC Johnson, F Liu, TF Heinz, DA Reis, and S Ghimire. Probing electron-hole coherence in strongly driven 2d materials using high-harmonic generation. *Optica*, 9(5):512–516, 2022.

[69] REF Silva, IV Blinov, AN Rubtsov, O Smirnova, and M Ivanov. High-harmonic spectroscopy of ultrafast many-body dynamics in strongly correlated systems. *Nature Photonics*, 12:266–270, 2018.

[70] R Trebino, KW DeLong, DN Fittinghoff, JN Sweetser, MA Krumbügel, BA Richman, and DJ Kane. Measuring ultrashort laser pulses in the time-frequency domain using frequency-resolved optical gating. *Review of Scientific Instruments*, 68(9):3277–3295, 1997.

[71] M Stepanova and S Dew. *Nanofabrication: techniques and principles*. Springer Science & Business Media, 2011.

[72] PE Debevec and M Jitendra. *Recovering High Dynamic Range Radiance Maps from Photographs*. Association for Computing Machinery, New York, NY, USA, 1 edition, 2023.

[73] G Tortarolo, M Castello, A Diaspro, S Koho, and G Vicidomini. Evaluating image resolution in stimulated emission depletion microscopy. *Optica*, 5(1):32–35, 2018.

[74] M Van Heel and M Schatz. Fourier shell correlation threshold criteria. *Journal of structural biology*, 151(3):250–262, 2005.

[75] K Matsushima and T Shimobaba. Band-limited angular spectrum method for numerical simulation of free-space propagation in far and near fields. *Optics express*, 17(22):19662–19673, 2009.

[76] T Tahara, X Quan, R Otani, Y Takaki, and O Matoba. Digital holography and its multidimensional imaging applications: a review. *Microscopy*, 67(2):55–67, 2018.

[77] G Zheng, C Shen, S Jiang, P Song, and C Yang. Concept, implementations and applications of fourier ptychography. *Nature Reviews Physics*, 3(3):207–223, 2021.

[78] Y Shechtman, Y Eldar, O Cohen, H Chapman, J Miao, and M Segev. Phase retrieval with application to optical imaging. *IEEE Signal Processing Magazine*, 87(3):87–109, 2015.

[79] M Kim. Principles and techniques of digital holographic microscopy. *SPIE Reviews*, 1(1):018005, 2010.

[80] PJ Campagnola and C Dong. Second harmonic generation microscopy: principles and applications to disease diagnosis. *Laser Photonics Reviews*, 5(1):13–26, 2024.

[81] D Debarre, W Supatto, A Pena, A Fabre, T Tordjmann, P Combettes, M Schanne-Klein, and E Beaurepaire. Imaging lipid bodies in cells and tissues using third-harmonic generation microscopy. *Nature Methods*, 3(1):47–53, 2005.

[82] Y Gao, Y Fan, Y Wang, W Yang, Q Song, and S Xiao. Nonlinear holographic all-dielectric metasurfaces. *Nano Letters*, 18(12):8054–8061, 2018.

[83] K Murzyn, MLS van der Geest, L Guery, Z Nie, P van Essen, S Witte, and PM Kraus. Breaking abbe's diffraction limit with harmonic deactivation microscopy. *Science Advances*, 10(46):eadp3056, 2024.

[84] Y Pu, M Centurion, and D Psaltis. Harmonic holography: a new holographic principle. *Applied Optics*, 47(4):A103–A11 0, 2008.

[85] C Hsieh, R Grange, Y Pu, and D Psaltis. Three-dimensional harmonic holographic microcopy using nanoparticles as probes for cell imaging. *Optics Express*, 17(4):2880–2891, 2009.

[86] Y Farah, G Murray, J Field, M Varughese, L Wang, O Pinaud, and R Bartels. Synthetic spatial aperture holographic thirdharmonic generation microscopy. *Optica*, 11(5):693–705, 2024.

[87] S Roscam Abbing, R Kolkowski, Z Zhang, F Campi, L Lötgering, F Koenderink, and PM Kraus. Extreme-ultraviolet shaping and imaging by high-harmonic generation from nanostructured silica. *Physical Review Letters*, 128(22):223902, 2022.

[88] A Korobenko, S Rashid, AY Naumov, DM Villeneuve, DA Reis, P Berini, PB Corkum, and G Vampa. In situ high-harmonic microscopy of nanostructured solid. *Optica*, 10(5):642–649, May 2023.

[89] L Huang, S Zhang, and T Zentgraf. Metasurface holography: from fundamentals to applications. *Nanophotonics*, 7(6):1169–1190, 2018.

[90] B Reineke, B Sain, R Zhao, L Carletti, B Liu, L Huang, C De Angelis, and T Zentgraf. Silicon metasurfaces for third harmonic geometric phase manipulation and multiplexed holography. *Nano letters*, 19(9):6585–6591, 2019.

[91] S Jalil, K Awan, I Ali, S Rashid, J Baxter, A Korobenko, G Ernotte, A Naumov, D Villeneuve, A Staudte, P Berini, L Ramunno, and G Vampa. Controlling the polarization and phase of high-order harmonics with a plasmonic metasurface. *Optica*, 9(9):987–991, 2022.

[92] S Yamada and K Yabana. Determining the optimum thickness for high harmonic generation from nanoscale thin films: An ab initio computational study. *Physical Review B*, 103(15):155426, 2021.

[93] T Journigan, Y Liu, C Cabello, SN Berriel, NG Rudawski, P Banerjee, and M Chini. High harmonic generation in epitaxially grown zinc oxide films. *Journal of the Optical Society of America B*, 41(6):B1–B6, 2024.

[94] E Sanchez-Ortiga, A Doblas, G Saavedra, M Martínez-Corral, and J Garcia-Sucerquia. Off-axis digital holographic microscopy:practical design parameters foroperating at diffraction limit. *Applied Optics*, 53(10):2058–2066, 2014.

[95] C Messinis. *Dark-Field Digital Holographic Microscopy For Advanced Semiconductor Metrology*. PhD thesis, Vrije Universiteit Amsterdam, 2022.

[96] C Messinis, M Adhikary, T Cromwijk, T van Schaijk, S Witte, J de Boer, and A den Boef. Pupil apodization in digital holographic microscopy for reduction of coherent imaging effects. *Optics Continuum*, 1(5):1202–1217, 2022.

[97] F Maier, D Fuentes, JS Weinberg, JD Hazle, and JR Stafford. Robust phase unwrapping for mr temperature imaging using a magnitude-sorted list, multi-clustering algorithm. *Magnetic Resonance in Medecine*, 73(4):1662–1668, 2014.

[98] S Koho, G Tortarolo, M Castello, T Deguchi, A Diaspro, and G Vicidomini. Fourier ring correlation simplifies image restoration in fluorescence microscopy. *Nature communications*, 10(1):3103, 2019.

[99] FL Pedrotti, LM Pedrotti, and LS Pedrotti. *Introduction to Optics*. Cambridge University Press, 3 edition, 2018.

[100] F Bijloo, AJ den Boef, PM Kraus, and AF Koenderink. Structure-in-void quasi-bound state in the continuum metasurface for deeply subwavelength nanostructure metrology. *ACS nano*, 19(36):32082–32092, 2025.

[101] A Taflove, SC Hagness, and M Piket-May. Computational electromagnetics: the finite-difference time-domain method. *The Electrical Engineering Handbook*, 3(629-670):15, 2005.

[102] F Bijloo, K Murzyn, F van Emmerik, AJ den Boef, PM Kraus, and AF Koenderink. Near-unity all-optical modulation of third-harmonic generation with a fano-resonant dielectric metasurface. *Nano Letters*, 24(41):12942–12947, 2024.

[103] Z Nie, L Guery, EB Molinero, P Juergens, TJ Van Den Hooven, Y Wang, A Jimenez Galan, PCM Planken, REF Silva, and PM Kraus. Following the nonthermal phase transition in niobium dioxide by time-resolved harmonic spectroscopy. *Physical review letters*, 131(24):243201, 2023.

[104] Z Nie, K Murzyn, L Guery, TJ van den Hooven, and PM Kraus. Ultrafast permittivity engineering enables broadband enhancement and spatial emission control of harmonic generation in zno. *ACS photonics*, 11(12):5084–5090, 2024.

[105] PJ Van Essen, B De Keijzer, T Van Horen, EB Molinero, AJ Galán, REF Silva, and PM Kraus. Spatial polarization gating of high-harmonic generation in solids. *Physical Review Research*, 7(1):L012063, 2025.

[106] B De Keijzer, PJ van Essen, and PM Kraus. Effect of photoexcitation on high-harmonic generation in semiconductors. *Journal of the Optical Society of America B*, 41(8):1754–1763, 2024.

[107] Lisa-Marie Koll, Simon Vendelbo Bylling Jensen, Pieter J Van Essen, Brian De Keijzer, Emilia Olsson, Jon Cottom, Tobias Witting, Anton Husakou, Marc JJ Vrakking, Lars Bojer Madsen, et al. Extreme ultraviolet high-harmonic interferometry of excitation-induced bandgap dynamics in solids. *Optica*, 12(10):1606–1614, 2025.

[108] RB Varillas, P Agostini, F Ardana-Lamas, CL Arnold, D Ayuso, M Reduzzi, J Benda, J Biegert, C Bourassin-Bouchet, T Brabec, et al. Roadmap on attosecond science. *arXiv preprint arXiv:2604.15085*, 2026.

[109] B Zaks, R Liu, and MS Sherwin. Experimental observation of electron–hole recollisions. *Nature*, 483(7391):580–583, 2012.

[110] O Schubert, M Hohenleutner, F Langer, B Urbanek, C Lange, U Huttner, D Golde, T Meier, M Kira, SW Koch, et al. Sub-cycle control of terahertz high-harmonic generation by dynamical bloch oscillations. *Nature Photonics*, 8(2):119–123, 2014.

[111] PM Kraus and HJ Wörner. Perspectives of attosecond spectroscopy for the understanding of fundamental electron correlations. *Angewandte Chemie International Edition*, 57(19):5228–5247, 2018.

[112] D Baykusheva, PM Kraus, SB Zhang, N Rohringer, and HJ Wörner. The sensitivities of high-harmonic generation and strong-field ionization to coupled electronic and nuclear dynamics. *Faraday discussions*, 171:113–132, 2014.

[113] DD Winters, DR Smith, and R Bartels. Measurement of orientation and susceptibility ratios using apolarization-resolved second-harmonic generation holographic microscope. *Biomedical Optics Express*, 3(9):2004–2011, 2012.

[114] E Shaffer, P Marquet, and C Depeursinge. Real time, nanometric 3d-tracking of nanoparticles made possible by second harmonic generation digital holographic microscopy. *Optics Express*, 18(16):17392–17403, 2010.

[115] Murat Sivis, Marco Taucer, Giulio Vampa, Kyle Johnston, André Staudte, Andrei Yu Naumov, DM Villeneuve, Claus Ropers, and PB Corkum. Tailored semiconductors for high-harmonic optoelectronics. *Science*, 357(6348):303–306, 2017.

[116] LM Stadler, C Gutt, T Autenrieth, O Leupold, S Rehbein, Y Chushkin, and G Grübel. Hard x ray holographic diffraction imaging. *Physical Review Letters*, 100(24):245503, 2008.

[117] W Eschen, S Wang, C Liu, R Klas, M Steinert, S Yulin, H Meißner, M Bussmann, T Pertsch, J Limpert, and J Rothhardt. Towards attosecond imaging at the nanoscale using broadband holography-assisted coherent imaging in the extreme ultraviolet. *Communications Physics*, 4(1):154, 2021.

[118] DJ Treacher, DT Lloyd, F Wiegandt, K O'Keeffe, and SM Hooker. Optimised xuv holography using spatially shaped high harmonic beams. *Optics Express*, 27(20):29016, 2019.

[119] GO Williams, AI Gonzalez, S Künzel, L Li, M Lozano, E Oliva, B Iwan, S Daboussi, W Boutu, H Merdji, M Fajardo, and P Zeitoun. Fourier transform holography with high harmonic spectra for attosecond imaging applications. *Optics Letters*, 40(13):3205, 2015.

[120] Tianhan Wang et al. Femtosecond single-shot imaging of nanoscale ferromagnetic order in co/pd multilayers using resonant x-ray holography. *Physical Review Letters*, 108(26):267403, 2012.

[121] M Di Pietro Martínez, A Wartelle, CH Martínez, Farid Fettar, Florent Blondelle, Jean François Motte, Claire Donnelly, Luke Turnbull, Feodor Ogrin, Gerrit Van Der Laan, Horia Popescu, Nicolas Jaouen, Flora Yakhou-Harris, and Guillaume Beutier. Three-dimensional tomographic imaging of the magnetization vector field using fourier transform holography. *Physical Review B - Condensed Matter and Materials Physics*, 107(9):094425, 2023.

[122] A Kiani, K Venkatakrishnan, and B Tan. Direct patterning of silicon oxide on si-substrate induced by femtosecond laser. *Opt. Express*, 18(3):1872–1878, 2010.

[123] M Rini, R Tobey, N Dean, J Itatani, Y Tomioka, Y Tokura, RW Schoenlein, and A Cavalleri. Control of the electronic phase of a manganite by mode-selective vibrational excitation. *Nature*, 449(7158):72–74, 2007.

[124] JH Gerrit, H Böckmann, B Wit, F Kurtz, G Storeck, and C Ropers. Coherent control of a surface structural phase transition. *Nature*, 583(7815):232–236, 2020.

[125] M Imada, A Fujimori, and Y Tokura. Metal-insulator transitions. *Reviews of modern physics*, 70(4):1039, 1998.

[126] Z Yang, C Ko, and S Ramanathan. Oxide electronics utilizing ultrafast metal-insulator transitions. *Annual Review of Materials Research*, 41(1):337–367, 2011.

[127] S Kumar, RS Williams, and Z Wang. Third-order nanocircuit elements for neuromorphic engineering. *Nature*, 585(7826):518–523, 2020.

[128] D Wegkamp, M Herzog, L Xian, M Gatti, P Cudazzo, CL McGahan, RE Marvel, RF Haglund Jr, A Rubio, M Wolf, et al. Instantaneous band gap collapse in photoexcited monoclinic VO_2 due to photocarrier doping. *Physical Review Letters*, 113(21):216401, 2014.

[129] VR Morrison, RP Chatelain, KL Tiwari, A Hendaoui, A Bruhács, M Chaker, and BJ Siwick. A photoinduced metal-like phase of monoclinic VO2 revealed by ultrafast electron diffraction. *Science*, 346(6208):445–448, 2014.

[130] TT Luu and Hans J Wörner. Measurement of the berry curvature of solids using high-harmonic spectroscopy. *Nature Communications*, 9(1):916, 2018.

[131] M Borsch, CP Schmid, L Weigl, S Schlauderer, N Hofmann, C Lange, JT Steiner, SW Koch, R Huber, and M Kira. Super-resolution lightwave tomography of electronic bands in quantum materials. *Science*, 370(6521):1204–1207, 2020.

[132] JB Costello, SD O'Hara, Q Wu, DC Valovcin, LN Pfeiffer, KW West, and MS Sherwin. Reconstruction of bloch wavefunctions of holes in a semiconductor. *Nature*, 599(7883):57–61, 2021.

[133] J Alcalà, U Bhattacharya, J Biegert, M Ciappina, U Elu, T Graß, PT Grochowski, M Lewenstein, A Palau, TPH Sidiropoulos, et al. High-harmonic spectroscopy of quantum phase transitions in a high-$_c$ superconductor. *Proceedings of the National Academy of Sciences*, 119(40):e2207766119, 2022.

[134] CP Schmid, L Weigl, P Grössing, V Junk, C Gorini, S Schlauderer, S Ito, M Meierhofer, N Hofmann, D Afanasiev, et al. Tunable non-integer high-harmonic generation in a topological insulator. *Nature*, 593(7859):385–390, 2021.

[135] EB Molinero and REF Silva. Coherent control of the photoinduced transition in a strongly correlated material. *Phys. Rev. Res.*, 4:043198, 2022.

[136] J Freudenstein, M Borsch, M Meierhofer, D Afanasiev, CP Schmid, F Sandner, M Liebich, A Girnghuber, M Knorr, M Kira, et al. Attosecond clocking of correlations between bloch electrons. *Nature*, 610(7931):290–295, 2022.

[137] L Vidas, D Schick, E Martínez, D Perez-Salinas, A Ramos-Álvarez, S Cichy, S Batlle-Porro, AS Johnson, KA Hallman, RF Haglund Jr, et al. Does VO2 host a transient monoclinic metallic phase? *Physical Review X*, 10(3):031047, 2020.

[138] G Belanger, J Destry, G Perluzzo, and PM Raccah. Electron transport in single crystals of niobium dioxide. *Canadian Journal of Physics*, 52(22):2272–2280, 1974.

[139] A O'Hara and AA Demkov. Nature of the metal-insulator transition in NbO2. *Physical Review B - Condensed Matter and Materials Physics*, 91(9):094305, 2015.

[140] Y Wang, RB Comes, S Kittiwatanakul, SA Wolf, and J Lu. Epitaxial niobium dioxide thin films by reactive-biased target ion beam deposition. *Journal of Vacuum Science & Technology A*, 33(2):021516, 2015.

[141] Y Wang, Z Nie, Y Shi, Y Wang, and F Wang. Coherent vibrational dynamics of nbo2 film. *Physical Review Materials*, 6(3):035005, 3 2022.

[142] K Shibuya and A Sawa. Epitaxial growth and polarized raman scattering of niobium dioxide films. *AIP Advances*, 12(5):055103, 2022.

[143] GJ Páez Fajardo, SA Howard, E Evlyukhin, MJ Wahila, WR Mondal, M Zuba, JE Boschker, H Paik, DG Schlom, JT Sadowski, et al. Structural phase transitions of NbO2: bulk versus surface. *Chemistry of Materials*, 33(4):1416–1425, 2021.

[144] H Nishidome, K Nagai, K Uchida, Y Ichinose, Y Yomogida, Y Miyata, K Tanaka, and K Yanagi. Control of high-harmonic generation by tuning the electronic structure and carrier injection. *Nano Letters*, 20(8):6215–6221, 2020.

[145] PC Becker, HL Fragnito, CH Brito Cruz, RL Fork, JE Cunningham, JE Henry, and CV Shank. Femtosecond photon echoes from band-to-band transitions in gaas. *Physical Review Letters*, 61(14):1647, 1988.

[146] Y Sakai, N Tsuda, and T Sakata. Electrical properties of semiconducting NbO_2. *Journal of the Physical Society of Japan*, 54(4):1514–1518, 1985.

[147] Y Cheng, H Hong, H Zhao, C Wu, Y Pan, C Liu, Y Zuo, Z Zhang, J Xie, J Wang, et al. Ultrafast optical modulation of harmonic generation in two-dimensional materials. *Nano Letters*, 20(11):8053–8058, 2020.

[148] P et al. Giannozzi. Quantum espresso: a modular and open-source software project for quantum simulations of materials. *Journal of physics: Condensed matter*, 21(39):395502, 2009.

[149] AA Mostofi, JR Yates, G Pizzi, Y Lee, I Souza, D Vanderbilt, and N Marzari. An updated version of wannier90: A tool for obtaining maximally-localised wannier functions. *Comput. Phys. Commun.*, 185(8):2309–2310, 2014.

[150] REF Silva, F Martín, and M Ivanov. High harmonic generation in crystals using maximally localized wannier functions. *Physical Review B - Condensed Matter and Materials Physics*, 100(19):195201, 2019.

[151] D Vanderbilt. *Berry Phases in Electronic Structure Theory*. Cambridge University Press, 2018.

[152] Z Wang, H Park, YH Lai, J Xu, CI Blaga, F Yang, P Agostini, and LF DiMauro. The roles of photo-carrier doping and driving wavelength in high harmonic generation from a semiconductor. *Nature Communications*, 8(1):1686, 2017.

[153] JK Clark, Y Ho, H Matsui, H Tabata, and J Delaunay. Thresholdless behavior and linearity of the optically induced metallization of NbO2. *Physical Review Research*, 1(3):033168, 2019.

[154] K Nagai, K Uchida, S Kusaba, T Endo, Y Miyata, and K Tanaka. Effect of incoherent electron-hole pairs on high harmonic generation in an atomically thin semiconductor. *Physical Review Research*, 5(4):043130, 2023.

[155] KS Takeda, K Uchida, K Nagai, S Kusaba, S Takahashi, and K Tanaka. Ultrafast electron-electron scattering in metallic phase of 2 h-nbse 2 probed by high harmonic generation. *Physical Review Letters*, 132(18):186901, 2024.

[156] R Rana, JM Klopf, J Grenzer, H Schneider, M Helm, and A Pashkin. Nonthermal nature of photoinduced insulator-to-metal transition in nbo2. *Physical Review B — Condensed Matter and Materials Physics*, 99(4), 1 2019.

[157] N Tancogne-Dejean, MA Sentef, and A Rubio. Ultrafast modification of hubbard U in a strongly correlated material: *ab initio* high-harmonic generation in NiO. *Physical Review Letters*, 121(9):097402, 2018.

[158] S Imai, A Ono, and S Ishihara. High harmonic generation in a correlated electron system. *Physical Review Letters*, 124(15):157404, 2020.

[159] K Uchida, G Mattoni, S Yonezawa, F Nakamura, Y Maeno, and K Tanaka. High-order harmonic generation and its unconventional scaling law in the mott-insulating Ca2RuO4. *Physical Review Letters*, 128(12):127401, 2022.

[160] SA Donges, O Khatib, BT O'Callahan, JM Atkin, JH Park, D Cobden, and MB Raschke. Ultrafast nanoimaging of the photoinduced phase transition dynamics in VO_2. *Nano Letters*, 16(5):3029–3035, 2016.

[161] KT Jacob, C Shekhar, M Vinay, and Y Waseda. Thermodynamic properties of niobium oxides. *Journal of Chemical & Engineering Data*, 55(11):4854–4863, 2010.

[162] G de Haan, TJ van den Hooven, and PCM Planken. Ultrafast laser-induced strain waves in thin ruthenium layers. *Optics Express*, 29(20):32051–32067, 2021.

[163] C Brahms, L Zhang, X Shen, U Bhattacharya, M Recasens, J Osmond, T Grass, RW Chhajlany, KA Hallman, RF Haglund, et al. Decoupled few-femtosecond phase transitions in vanadium dioxide. *Nature Communications*, 16(1):3714, 2025.

[164] IA Walmsley and C Dorrer. Characterization of ultrashort electromagnetic pulses. *Advances in Optics and Photonics*, 1(2):308–437, Apr 2009.

[165] C Iaconis and IA Walmsley. Spectral phase interferometry for direct electric-field reconstruction of ultrashort optical pulses. *Optics Letters*, 23(10):792–794, 1998.

[166] K Uchida and K Tanaka. High harmonic mach–zehnder interferometer for probing sub-laser-cycle electron dynamics in solids. *Optica*, 11(8):1130–1137, 2024.

[167] I Amat-Roldán, IG Cormack, P Loza-Alvarez, EJ Gualda, and D Artigas. Ultrashort pulse characterisation with shg collinear-frog. *Opt. Express*, 12(6):1169–1178, Mar 2004.

[168] J Chung and AM Weiner. Ambiguity of ultrashort pulse shapes retrieved from the intensity autocorrelation and the power spectrum. *IEEE Journal of selected topics in quantum electronics*, 7(4):656–666, 2001.

[169] R Chadwick, E Spahr, JA Squier, CG Durfee, BC Walker, and DN Fittinghoff. Fringe-free, background-free, collinear third-harmonic generation frequency-resolved optical gating measurements for multiphoton microscopy. *Optics Letters*, 31(22):3366–3368, 2006.

[170] J Hyyti, E Escoto, and G Steinmeyer. Third-harmonic interferometric frequency-resolved optical gating. *Journal of the Optical Society of America B*, 34(11):2367–2375, 2017.

[171] T Danz, T Domröse, and C Ropers. Ultrafast nanoimaging of the order parameter in a structural phase transition. *Science*, 371(6527):371–374, 2021.

[172] Y Kim, H Nho, S Ji, H Lee, H Ko, J Weissenrieder, and O Kwon. Femtosecond-resolved imaging of a single-particle phase transition in energy-filtered ultrafast electron microscopy. *Science Advances*, 9(4):eadd5375, 2023.

[173] S Varghese, JD Mehew, A Block, DS Reig, P Woźniak, R Farris, Z Zanolli, P Ordejón, MJ Verstraete, NF Van Hulst, et al. A pre-time-zero spatiotemporal microscopy technique for the ultrasensitive determination of the thermal diffusivity of thin films. *Review of Scientific Instruments*, 94(3), 2023.

LIST OF PUBLICATIONS

1 - Z. Nie, L. Guery, E. Molinero, P. Juergens, T. van Den Hooven, Y. Wang, A. Jimenez Galan, P. Planken, R. Silva and P.M. Kraus (2023). Following the nonthermal phase transition in niobium dioxide by time-resolved harmonic spectroscopy. *Physical review letters*. 131(24): 243201. DOI: https://doi.org/10.1103/PhysRevLett.131.243201
Authors Contribution
Zhonghui Nie – Writing, experimental work, data analysis.
Leo Guery – Experimental work, data analysis.
Thomas van den Hooven and Paul Planken - Experimental implementation.
Peter Juergens - Results interpretation.
Yong-Long Wang - Sample fabrication and characterization.
Eduardo Molinero, Alvaro Jimenez Galan and Rui Silva - SHHG simulations.
Peter Kraus - Supervision and data analysis
Presented in chapter 6.

2 - L. Guery, F. Bijloo and P.M. Kraus (2026). Digital Holography Using Harmonic Generation from Solids for Reconstruction of Subwavelength Nanostructures. *ACS Photonics*. 13(4):1055-1064. DOI: https://doi.org/10.1021/acsphotonics.5c02501
Authors Contribution
Leo Guery – Writing, experimental work, data analysis.
Falco Bijloo - Data analysis.
Peter Kraus - Supervision and data analysis.
Presented in chapter 4.

3 - F. Corazza, E. Kechaoglou, L. Guery, Z. Nie, P. Phadke, C. Lehmann, R. Bliem and P.M. Kraus (2025). Broadband extreme ultraviolet zero-order Scatterometry for nanostructure metrology. PREPRINT (Version 1) available at Research Square.
DOI: https://doi.org/10.21203/rs.3.rs-7215343/v1.
Not presented in this thesis.

4 - K. Murzyn, M. van der Geest, L. Guery, Z. Nie, P. van Essen, S. Witte, and P.M. Kraus (2024). Breaking Abbe's diffraction limit with harmonic deactivation microscopy. *Science advances*. 10(46): eadp3056. DOI: http://doi.org/10.1126/sciadv.adp3056
Not presented in this thesis.

SUMMARY

High-harmonic generation from solids (SHHG) has established itself as a remarkable tool for probing ultrafast dynamics in matter. Highly non-linear interactions between light and matter characterizing this process allow to study the dynamic change to the electronic and structural properties of solids at very short time scale. In this thesis, we have used SHHG spectroscopy to investigate the insulator-to-metal (IMT) phase transition in correlated materials. These unique materials are extremely attractive for the development of next generation opto-electronic devices, due to their ability to change resistance in reaction to small external perturbations. Therefore, improving our understanding of the exact mechanisms driving these phase transitions is crucial.

Measuring the phase of light, as provided by holographic measurements, is necessary in order to fully describe SHHG emission. Therefore, this work also aimed at combining SHHG with holographic imaging in order to develop new metrology techniques for the characterization of nanostructures etched in semiconductors. Transient dynamics in correlated materials were also assessed, using the phase information as an additional probing tool.

In chapter 4 we have demonstrated how digital holography could be used to recover both phase and amplitude of third harmonic light generated in silicon and how it allow to extract the morphological parameters of subwavelength structures. In chapter 5, a lensless approach was performed to recover the harmonic field, opening the way towards application at higher harmonic orders. The phase content of harmonic could be used to recover height differences with few-nanometer resolution. In chapter 6, we investigated the photo-induced phase transition in NbO_2 by measuring the transient SHHG. We showed how IMT is reflected on the yield of generated harmonics, and could allow to track dynamic electronic and structural changes in the material at the femtosecond time scale. In chapter 7, we took some first steps towards subcycle probing of SHHG, which may improve the time resolution of transient SHHG measurements. We have introduced a technique we named Subcycle Characterization of Optical Radiations via Perturbative Interferometry of Odd-harmonics (SCORPIO) and have presented some preliminary results. In the final chapter, we have combined the pump-probe scheme presented in chapter 6 with the digital holography reconstruction procedure presented in chapter 4 and achieved transient phase imaging of the third harmonic phase emitted during photo-excitation of NbO_2. We could link the recovered phase content to the band gap closure of the material when undergoing its phase transition.